PERFORMANCE OF A SHORT OPEN-END SQUEEZE FILM DAMPER WITH

FEED HOLES: EXPERIMENTAL ANALYSIS OF DYNAMIC FORCE

COEFFICIENTS

A Thesis

by

GARY DANIEL BRADLEY

Submitted to the Office of Graduate Studies of
Texas A&M University
in partial fulfillment of the requirements for the degree of

MASTER OF SCIENCE

Chair of Committee,	Luis San Andrés
Committee Members,	Dara Childs
	Tom Strganac
Head of Department,	Andreas Polycarpou

August 2013

Major Subject: Mechanical Engineering

ABSTRACT

With increasing rotor flexibility and shaft speeds, turbomachinery undergoes large dynamic loads and displacements. Squeeze film dampers (SFDs) are a type of fluid film bearing used in rotating machinery to attenuate rotor vibration, provide mechanical isolation, and/or to tune the placement of system critical speeds. Industry has a keen interest in designing SFDs that are small, lightweight, and mechanically simple. To achieve this, one must have a full understanding of how various design features affect the SFD forced performance.

This thesis presents a comprehensive analysis, experimental and theoretical, of a short (L=25.4 mm) open ends SFD design incorporating three lubricant feed holes (without a circumferential feed groove). The damper radial clearance (c=127 μm), L/D ratio (0.2), and lubricant (ISO VG2) have similar dimensions and properties as in actual SFDs for aircraft engine applications. The work presents the identification of experimental force coefficients ($\mathbf{K}$, $\mathbf{C}$, $\mathbf{M}$) from a 2-DOF system model for circular and elliptical orbit tests over the frequency range ω=10-250Hz. The whirl amplitudes range from r=0.05c-0.6c, while the static eccentricity ranges from e_S=0-0.5c.

Analysis of the measured film land pressures evidence that the deep end grooves (provisions for installation of end seals) contribute to the generation of dynamic pressures in an almost purely inertial fashion. Film land dynamic pressures show both viscous and inertial effects. Experimental pressure traces show the occurrence of significant air ingestion for orbits with amplitudes r>0.4c, and lubricant vapor cavitation when pressures drop to the lubricant saturation pressure (P_{sat}~0 bar).

Identified force coefficients show the damper configuration offers direct damping coefficients that are more sensitive to increases in static eccentricity (e_S) than to increases in amplitude of whirl (r). On the other hand, SFD inertia coefficients are more sensitive to increases in the amplitude of whirl than to increases in static eccentricity. For small amplitude motions, the added or virtual mass of the damper is as large as 27% of the bearing cartridge mass (M_{BC}=15.15 kg). The identified force coefficients are

shown to be insensitive to the orbit type (circular or elliptical) and the number of open feed holes (3, 2, or 1).

Comparisons of damping coefficients between a damper employing a circumferential feed groove[1] and the current damper employing feed holes (no groove), show that both dampers offer similar damping coefficients, irrespective of the orbit amplitude or static eccentricity. On the other hand, the grooved damper shows much larger inertia force coefficients, at least ~60% more.

Predictions from a physics based model agree well with the experimental damping coefficients, however for large orbit motion, over predict inertia coefficients due to the model neglecting convective inertia effects.

Credence is given to the validity of the linearized force coefficients by comparing the actual dissipated energy to the estimated dissipated energy derived from the identified force coefficients. The percent difference is below 25% for all test conditions, and in fact is shown to be less than 5% for certain combinations of orbit amplitude (r), static eccentricity (e_S), and whirl frequency (ω).

---

[1] Tested earlier by other students

DEDICATION

To Stephenie …the reason for my desire and motivation to achieve

ACKNOWLEDGEMENTS

NOMENCLATURE

a_X, a_Y	BC absolute acceleration [m/s^2]
B_α	Bias uncertainty in the measured parameter α
c, c_g	Film land radial clearance, groove radial clearance [μm]
C^*	Classical SFD damping coefficient [N.s/m]
$C_{\alpha\beta,\ (\alpha,\beta=X,Y)}$	Identified damping coefficients of the lubricated structure [N.s/m]
$C_{SFD\alpha\beta,\ (\alpha,\beta=X,Y)}$	Identified SFD damping coefficients [N.s/m]
$C_{S\alpha\beta,(\alpha,\beta=X,Y)}$	Identified remnant damping coefficients of the dry structure [N.s/m]
C	Film land flow conductance [LPM/bar]
D	Journal diameter [mm]
e	Dynamic eccentricity [μm]
e_S, e_{SX}, e_{SY}	Static eccentricity along 45°, X-axis, and Y-axis [μm]
E_v	Dissipated energy [J]
$F_{X(t)}$, $F_{Y(t)}$	Excitation force along X-axis and Y-axis
h	Lubricant film thickness [μm]
$H_{(\omega)}$	Impedance function [N/m]
$K_{\alpha\beta,\ (\alpha,\beta=X,Y)}$	Identified stiffness coefficients of the lubricated structure [MN/m]
$K_{SFD\alpha\beta,\ (\alpha,\beta=X,Y)}$	Identified SFD stiffness coefficients [MN/m]
$K_{S\alpha\beta,(\alpha,\beta=X,Y)}$	Identified structural stiffness coefficients of the dry structure [MN/m]
L, L_g	Axial film land length, groove axial length [mm]
M_{BC}	Effective mass of BC [kg]
M^*	Classical SFD mass coefficient [kg]
$M_{\alpha\beta,\ (\alpha,\beta=X,Y)}$	Identified added mass coefficients of the lubricated structure [kg]

$M_{SFD\alpha\beta,\ (\alpha,\beta=X,Y)}$	Identified SFD added mass coefficients [kg]
$M_{S\alpha\beta,(\alpha,\beta=X,Y)}$	Identified inertia coefficients of the dry structure [kg]
O_J, O_B	Journal equilibrium position and bearing center
P_α	Precision uncertainty in the measured parameter α
P, P_{static}	Dynamic and static pressure in film land [bar]
P_a, P_{cav}, P_{sat}	Ambient pressure, lubricant cavitation pressure, and lubricant saturation pressure [bar]
P_S	Lubricant supply pressures at journal inlet [bar]
$P_{P\text{-}P}, P^*$	Peak-to-peak dynamic pressure and normalized peak-to-peak dynamic pressure [bar]
Q_{in}, Q_b	Supply lubricant flow rate and bottom lubricant flow rate
r, r_X, r_Y	Amplitude of circular motion and elliptical motion along X, Y-axes [μm]
R	Journal radius [mm]
Re_s	Modified squeeze film Reynolds number, $\rho\omega c^2/\mu$
t	Time [s]
T_a, T_s	Ambient temperature and lubricant supply temperature [^{o}C]
T_P	Period of whirl motion [s]
U_α	Total uncertainty in the measured parameter α
$x_{(t)}, y_{(t)}$	BC displacements along X and Y directions [μm]
z	Damper axial coordinate [mm]
α_v	Oil viscosity coefficient [1/°C]
γ	Squeeze flow parameter [-]
ε	Dimensionless orbit radius r/c [-]
ζ	Damping ratio [-]
θ, Θ	Rotating angular and fixed SFD angular coordinates [°]
$\tilde{\kappa}_z$	Flow shear parameter [-]
μ	Lubricant dynamic viscosity [cP]

ρ	Lubricant density [kg/m^3]
ϕ_X, ϕ_Y	Arguments of the fundamental component of the Fourier series
ω, ω_n	Excitation (whirl) frequency, natural frequency [rad/s]

Matrices and Vectors

a	Matrices BC absolute accelerations [m/s^2]
C$_S$, C, C$_{SFD}$	Matrices of damping coefficients for dry structure, lubricated system and squeeze film [N.s/m]
e	IVFM error matrix
K$_S$, K, K$_{SFD}$	Matrices of stiffness coefficients for dry structure, lubricated system and squeeze film [N/m]
F$_S$, F, F$_{SFD}$	Vectors of dry structural reaction force, excitation force and squeeze film force [N]
G	Flexibility matrix [m/N]
H	Mechanical impedance matrix[N/m]
I	Identity matrix [-]
M$_S$, M, M$_{SFD}$	Matrices of inertia coefficients for dry structure, lubricated system and squeeze film [kg]
W	Instrument variable filter matrix
z, ż, z̈	Vectors of journal/BC relative displacement, relative velocity, relative acceleration [m/s^2]

TABLE OF CONTENTS

LIST OF FIGURES

xii

xiii

LIST OF TABLES

CHAPTER I

INTRODUCTION

Squeeze film dampers (SFDs) are a type of fluid film bearing used mainly in rotating machinery to attenuate rotor vibration and/or to tune the placement of system critical speeds. The most common application of SFDs is in gas-turbine aircraft engines, where a non-rotating "journal" is assembled to the outer race of a ball bearing. The journal is allowed to precess or "whirl" within a small clearance between it and the bearing housing. Lubricant supplied to the clearance, or annulus, between the journal and bearing housing, produces hydrodynamic pressures when squeezed from the journal precession. The hydrodynamic pressures exert reaction forces on the whirling journal that dissipate mechanical energy, limiting the rotor amplitude of motion and the forces transmitted to the bearing housing.

A SFD forced performance depends on numerous factors such as its geometric configuration, flow regime, and lubricant gaseous phenomena (lubricant cavitation and air ingestion) among others. Much research has been devoted to determining the effects of damper geometry on the forced response, however there are unlimited possible configurations. Simple designs are more desirable in industry because of their low cost and maintenance. SFDs incorporating a circumferential feeding groove have traditionally been investigated, as the groove provides a uniform flow around the damper circumference. On the other hand, some research efforts have aimed at assessing the performance of SFDs with a simpler feeding mechanism, such as orifice feed holes.

SFDs incorporating feed holes can potentially provide similar forced performance as a longer SFD with a circumferential feed groove. Dampers with a shorter axial length save space and weight, which are vital to the aerospace industry. The majority of research utilizing the feed hole design focuses on the flow dynamics of the feed holes and how they affect the formation of oil cavitation regions. However, few of these efforts experimentally determine the forced performance of hole fed SFDs. Additionally, to the author's knowledge, published experimental research comparing the forced

performance of a SFD with feed holes to a SFD with a circumferential feed groove does not exist.

Literature Review

Background

Cooper [1] investigated squeeze films almost 50 years ago as a means to reduce the amplitude of rotor vibrations due to imbalance. Della Pietra and Adiletta [2] notes that some US patents issued as early as in 1933 and 1948 depicted a type of SFD. Since these early investigations, a plethora of research and development has enhanced understanding, design, and usage of SFDs. Della Pietra and Adiletta [2, 3] give a comprehensive review of the main research findings from the 1960s to the early 2000s. The papers discuss the construction characteristics and operating features of the SFD as a separate component [2] and also reviews research work the on dynamic behavior of rotors equipped with SFDs [3].

Correct design and implementation of SFDs in rotating machinery is of great importance, since if the damping is too large, the SFD acts as a rigid constraint and transmits large forces to the supporting structure, whereas if damping is too low, the SFD is ineffective and likely to permit large amplitude motions [4]. Zeidan *et al.* [5] discuss numerous design aspects that effect the performance of SFDs, such as geometry (length, diameter, and radial clearance), viscosity of the lubricant used, supply pressure, feeding and discharge flow mechanisms, type of end seals, fluid inertia, dynamic cavitation, etc.

The aforementioned literature gives a good basis for understanding of SFD design practices and research areas. The following outlines prior research work on specific areas of interest that the proposed work intends to address.

Fluid inertia effects

The majority of SFD research has focused on the magnitude of the oil film forces developed and the factors affecting them. Classical lubrication theory ignores fluid

inertia and gives the Reynolds equation to describe the hydrodynamic pressure distribution in the oil film. This classical equation, however, is overly simplified for application to SFDs. Typical SFD applications with large clearances (c), low viscosity (μ) lubricants, and operating high whirl frequencies (ω) are highly affected by fluid inertia [5]. Reinhart and Lund [6] derive journal bearing force coefficients including fluid inertia effects for plain journal bearings. Their results indicate that the added mass (inertia) coefficient can be several times the mass of the journal itself and may significantly affect system critical speeds.

Tichy, through numerous works [7, 8, 9], expands the theory to analyze SFDs with fluid inertia effects. In particular, he presents a modified Reynolds equation and concludes that fluid inertia causes a large increase in pressure amplitude, a change in the shape of the dynamic pressure curve, and a phase shift of the pressure peak in the direction of the precessional motion [9]. Tichy [7] also demonstrates that fluid inertia forces are comparable to viscous forces for operation with large squeeze film Reynolds numbers $\mathrm{Re_s}= \rho\omega c^2/\mu >10$.

San Andrés [10] presents expressions to calculate force coefficients for SFDs performing small to large orbits in centered and off-centered journal conditions. The analysis shows that the fluid virtual mass decreases as the orbit radius increases due to convective acceleration terms.

Other works, such as in Refs. [11-18], show that circumferential grooves ranging from shallow to deep do produce dynamic film pressures and add significant amounts of fluid inertia to the lubricated system. More recent work by Delgado [19] introduces an effective groove depth, lesser than the actual depth, that accurately predicts the contribution of the circumferential groove to the SFD forced performance. However, this analysis does not give an empirical relation to determine the effective groove depth, but merely selects the effective depth that best fits the experimental data. A more scientific approach that does not depend on experimental data is needed.

Oil cavitation and air ingestion

Lubricant cavitation and air ingestion are types of lubricant gaseous phenomena that cause a fluid film to rupture. The film rupture causes adverse effects on the generation of hydrodynamic pressures, and is therefore a critical topic for SFD research efforts.

Sun and Brewe [20] show through high-speed photography formation and patterns of cavitation bubbles in a whirling SFD. The analysis shows that the cavitation bubble emerges and collapses for a non-centered circular whirl. However for a centered circular whirl, the lubricant film locally cavitates as the low-pressure wave revolves around the bearing circumference, which produces the appearance of a revolving cavitation bubble. The authors conclude that small bearing clearance, high whirl speed, and large eccentricity prompt the occurrence of lubricant cavitation, indicating that larger dynamic pressures are more likely to form cavitation regions.

In a follow-up study, Sun and Brewe [21] simultaneously take pressure measurements and high-speed photographs to obtain more insight on oil cavitation regimes. When the fluid film cavitates the film pressure is near absolute zero. Air entrained into the vaporous cavitation bubble increases the pressure slightly. Interestingly, cavitation sometimes did not occur when the measured pressure was at or below absolute zero. In fact, several cases show the fluid withstanding large negative pressures or tension. As the authors indicate, there were several sources of error in the pressure measurement magnitudes and the pressure measurements should be taken as illustrative only.

More recently, Xing and Braun [22] present pictures showing the differences between lubricant vapor cavitation and lubricant gaseous cavitation. Gaseous cavitation occurs even at low whirl speeds (1000 RPM) as a fern-like shape concentrated in a small area. With an increased whirl frequency, vapor cavitation becomes apparent as large vapor pockets concentrated at the damper axial mid-plane (area of largest negative pressure). Gaseous cavitation is still present (in the form of numerous small air bubbles) with the occurrence of vapor cavitation and in fact expands across the entire film land length. The large vapor bubbles or pockets due to vapor cavitation are shown to have

instantaneous formation and explosive collapse that can detrimentally affect damper performance.

Similarly, San Andrés and Diaz [23] present high-speed pictures from a SFD operating with either gaseous cavitation and/or air ingestion. Air ingestion is shown to produce striations through the film originating from the damper open end. Gaseous cavitation is shown as a fern-like shape similar to that in [22].

In general, visualizations of oil film gaseous phenomena show the randomness and unpredictability from period to period, device-to-device, etc. Various cavitation models have been developed to accurately predict and model lubricant cavitation in hydrodynamic bearings including SFDs. Jacobson, Floberg and Olsson [24-25] introduce a cavitation algorithm (JFO model) that fully satisfies the principle of mass conservation at the rupture and reformation boundaries. Elrod [26] advances a universal cavitation algorithm that incorporates the JFO model into one equation that describes the flow in the full film and the cavitation region. Vijayarahavan and Keith [27] expand on the universal algorithm by incorporating a compressible fluid flow technique into a numerical algorithm that adapts automatically to flow conditions (cavitated or uncavitated). These cavitation models can provide realistic predictions for steady state journal bearings and fully flooded SFD configurations, however they are elaborate and at times difficult to implement with acceptable certainty.

On the other hand, algorithms describing the phenomenon of air ingestion are limited. Diaz and San Andrés [28] introduce a squeeze flow parameter (γ) that predicts the occurrence and amount of air ingestion that will occur in a damper geometry, with known supply flow and specific operating conditions. The squeeze flow parameter is assessed against experimental data and shown to accurately determine the conditions under which air ingestion will occur.

Mendez *et al.* [29] expand on the squeeze flow parameter and advance a model that estimates the performance of finite length SFDs operating with free air entrainment. The model shows that as the damper *L/D* ratio increases, the amount of entrained air reduces. The model also shows that operation with even a 60% air - 40% oil mixture the damper

forced performance is just within 3% of the 100% oil performance. Above 60% air content, the damper forced performance drops dramatically. Adjustments on the supply flow rate, supply pressure, or change in *L/D* ratio can limit the amount of air entrainment. Implementation of this model is rather straightforward; however the challenge comes in the appropriate selection of the lubricant feed boundary conditions.

Several other models for air ingestion such as Younan *et al.* [30] appear in the literature, but none have yet to be widely accepted. The elaborate implementation of cavitation models and lack of proven air ingestion models make lubricant gaseous phenomena in SFDs an interesting topic in need of further research. In general, industry over designs to avoid operating conditions that cause these caviation/air ingestion regimes. However, better understanding of the consequences of operating with lubricant cavitation and air ingestion will help to produce more efficient designs.

Lubricant feeding mechanisms

In general, there are three basic lubricant feed configurations for SFDs:

- in-film land circumferential groove (groove usually supplied by feed holes)
- end-groove/plenum
- in-film land feed holes

A circumferential feeding groove (end and in-film) is thought of as source for uniform lubricant flow around a damper circumference that aids in preventing lubricant starvation and/or cavitation. Refs. [11-18] present abundant research on grooved SFDs, as this is a commonly adopted lubricant feed mechanism. On the other hand, some research efforts have investigated SFDs with feed holes, as a means to simplify the design of SFDs and provide (theoretically) four times more damping than in-film land grooved dampers [5]. The following reviews research conducted on SFDs with oil feed holes.

Levesley and Holmes [31] analyze a SFD with a circumferential feed groove supplied by one to three holes. The results show that an open-end damper operating with one hole supplying the feed groove does not attenuate vibration as well as operation with

three holes supplying the groove. On the other hand, the number of supply holes has minimal effect when the damper is operating in a closed-end condition. The authors suggest that the differences with the open-end damper are due to lubricant cavitation, however do not present evidence (pressure profiles) of this effect. The results also indicate that the axial location of the circumferential groove does not significantly affect the damping capability as long as sufficient lubricant supply pressure is used. In fact the authors suggest that the damping factor is not dependent upon the position of the groove but rather the total land length of the damper. Although this damper configuration has a circumferential feed groove, the work gives insight of what to expect with variation of feed holes in a non-grooved damper.

Chen and Hahn [32] present an analysis to determine the pressure distribution at and around oil feed holes in SFDs. The procedure allows for any number of oil holes, check valves and flow restrictors to be accounted for. The results of computational analyses show that the pressure distribution radiates from the feed hole, with the highest pressure at the hole center and decreases away from the hole in all directions. The pressure distribution also shows to be film thickness dependent. For example, the pressure gradient is more expansive (covers more area of the damper) at $\theta=0$ (maximum film thickness) than at $\theta=180$ (minimum film thickness) where the pressure gradient is more localized. The results and discussion are intuitively correct and show realistic characteristics of the pressure field.

Much like Sun & Brewe [20, 21], Xing and Braun [22], and San Andrés and Diaz [23], Walton II *et al.* [33] present high-speed camera pictures of a cavitating SFDs. The unique aspect of this analysis is that Walton investigates two different damper feed configurations, feed groove versus feed holes. The high-speed photos show that the cavitation region is quite different for oil hole feed than for groove feed. The hole feed film rupture zone is strongly influenced by the hole and is not repeatable from cycle to cycle, differing from the grooved damper. The analysis shows that feed holes may act as drain (or sink) holes when the film land pressure is greater than the hole supply pressure.

Defaye *et al.* [34] present an experimental study that analyzes the effects of three different lubricant feeding systems (centered groove, eccentric groove, and orifice holes). The orifice feeding system shows the largest tangential (damping) force and radial (inertia) force compared to the feeding groove configurations. The radial force for all feeding systems has a dramatic drop at whirl radii higher than 60% of the clearance. Different feed pressures only seem to affect the radial force and increasing the oil temperature decreases the tangential force but increases the radial force.

From the reviewed literature it is clear that the majority of research on SFDs with lubricant feed holes focuses on the flow patterns and oil cavitation regimes. Of these research efforts, only one, Defaye *et al.* [34], attempts an experimental comparison to a damper of similar geometry (*D*, *L*, *c*) supplied with oil from a circumferential groove. The proposed work intends to give a more comprehensive and clear understanding of the differences between dampers with oil feed holes and dampers with feed grooves.

Parameter identification and SFD predictive models

Parameter identification techniques for estimating force coefficients in mechanical systems are well developed. There are numerous methods that accurately predict bearing parameters, however some may be more rigorous to implement than others. The following reviews literature relevant to the parameter identification technique used with the currently proposed work.

Tiwari, Lees, and Friswell [35] review methods of identifying bearing parameters in the time and frequency domains and outline, chronologically, the parameter identification techniques developed through the latter part of the 20th century. The assumptions and governing equations of bearing models as well as parameter identification algorithms are discussed.

Fritzen [36] introduces the Instrumental Variable Filter Method (IVFM) to identify parameters for mechanical systems with greater accuracy. The IVFM is a chaser to the least squares method, in which it builds a instrument variable matrix **W** from the least squares identified stiffness, damping, and mass matrices (**K**, **C**, **M**). The matrix **W** is

free of measurement noise and reduces error with each iteration of the IVFM. The iteration ceases when a specified error tolerance is reached, thus delivering coefficients (**K**, **C**, **M**) that are more accurate due to elimination of measurement noise.

San Andrés and Delgado [37, 38, 39] effectively determine force coefficients (stiffness *K*, damping *C*, mass *M*) of a SFD test rig using a frequency domain identification technique. Measurements of applied force and resulting displacements provide measured mechanical impedances, which are then curve fit in the frequency domain to identify the mechanical parameters (*K*, *C*, *M*). The parameters due to the squeeze film alone are extracted from the difference between the dry (un-lubricated) test rig parameters and wet (lubricated) test rig parameters. A slightly modified version of this parameter identification technique incorporating the Fritzen's IVFM [36] is used for the proposed work and is outlined in the experimental procedure section.

While parameter identification techniques are used to determine experimentally bearing parameters, SFD analytical models are implemented to predict the bearing parameters. The following literature outlines analytical models that have proven their worth in accurately predicting SFD forces.

Gehannin, Arghir, and Bonneau [40] discuss analysis of SFDs using the "Bulk-Flow" equations. Comprehensive techniques for integrating a circumferential feeding groove model, feeding orifices model, vapor cavitation model, and piston ring end seal model into the "Bulk-Flow" equations are presented. Integration of these design features into the bulk-flow equations give a more accurate and complete model for predicting SFD performance. The developed model is benchmarked with experimental results from Defaye *et al.* [34]. The enhanced bulk-flow model shows much better correlation with experimental data than the classical Reynolds theory predicts. The conclusions indicate that temperature variations can be taken into account using energy balance or "bulk-flow" energy equations.

San Andrés and Delgado [41] introduce a linear bulk-flow model that predicts damping and added mass coefficients in SFDs and oil seals based on an effective groove depth. The effective groove depth is determined from the depth of the streamline

dividing the thru-flow from the recirculation region across the groove. The analysis shows that damping coefficients decrease rapidly with increasing effective groove depths and that added mass coefficients are much more sensitive to changes in the effective depth. In SFDs with a central groove, a parametric study presented shows good correlation with experimental data for effective depths smaller or equal to 50% of an actual groove depth. The authors give recommendations to find the most appropriate effective depth based on the groove geometry by conducting comparisons with experiments.

Statement of Work

Modern industry continually pushes high performance turbomachinery to the limit by decreasing size and cost, but increasing operating speed and power output. This perpetual quest for increased efficiency presents unique challenges for the rotordynamics and bearings design engineers. With increasing rotor flexibilities and shaft speeds, turbomachinery undergoes large dynamic loads and large displacements. Finding the balance between lightweight, small, and mechanically simple (lower cost) bearings and high performance is ever in demand.

The current experimental work investigates the performance of a short SFD with a simple mechanical design and lubricant hole feeding mechanism. The work identifies and analyzes SFD rotordynamic force coefficients using a 2 degree of freedom (DOF) K-C-M model in which there are two direct coefficients (*XX*, *YY*) and two cross coupled coefficients (*XY*, *YX*), for instance $\mathbf{M}_{\mathbf{SFD}} = \begin{bmatrix} M_{XX} & M_{XY} \\ M_{YX} & M_{YY} \end{bmatrix}_{SFD}$. The work also compares the hole-fed SFD performance with a similar damper configuration incorporating a circumferential feeding groove (tested in [42, 43]). In addition, the identified force coefficients are compared to predicted force coefficients from a physics based computational tool [44]. Although there are unlimited SFD configurations, the knowledge obtained from this research work will assist in enhancing design practices throughout industry.

10

CHAPTER II

SQUEEZE FILM DAMPER (SFD) THEORY

This chapter presents a primer on SFD analysis, including a coordinate system, basic governing equations, assumptions, and formulas for the theoretical force coefficients. Although brief, the material in this chapter is necessary for a complete understanding of the preceding chapters.

Coordinate System

Figure 1 depicts a schematic representation of a simple cylindrical SFD with its journal whirling within a bearing housing of inner diameter D and length L. The journal whirl follows an orbit path around its equilibrium position (O_J) with orbit amplitude, r, and frequency, ω. Static loads on the journal cause the journal equilibrium position (O_J) to be statically offset[2] from the bearing center (O_B) by a static eccentricity, e_S. Lubricant with viscosity μ and density ρ fills the annular clearance (c) between the journal and bearing [4]. The lubricant film thickness h is

$$h(\Theta, t) = c + e_X \cos(\Theta) + e_Y \sin(\Theta) \tag{1}$$

or

$$h(\theta, t) = c + e \cos(\theta) \tag{2}$$

where e is the dynamic eccentricity with components $e_X = r \cos(\omega t) + e_{S_X}$ and $e_Y = r \sin(\omega t) + e_{S_Y}$. X and Y are stationary inertial axes with the origin at the bearing center. Θ is a fixed angular coordinate with origin at the X-axis, while θ is a rotating coordinate with its origin always at the maximum film thickness. θ increases from 0 to 2π in the direction of whirl. The figure shows a circular orbit path with amplitude r about a static eccentricity (e_S) along $\Theta=225°$. These conditions are a generalized operation and

---

[2] SFD do not react to static loads. In this case the static load is reacted by the elastic force from the support structure.

of representative nature only. Note the lubricant film thickness (h) is greatly exaggerated in the figure.
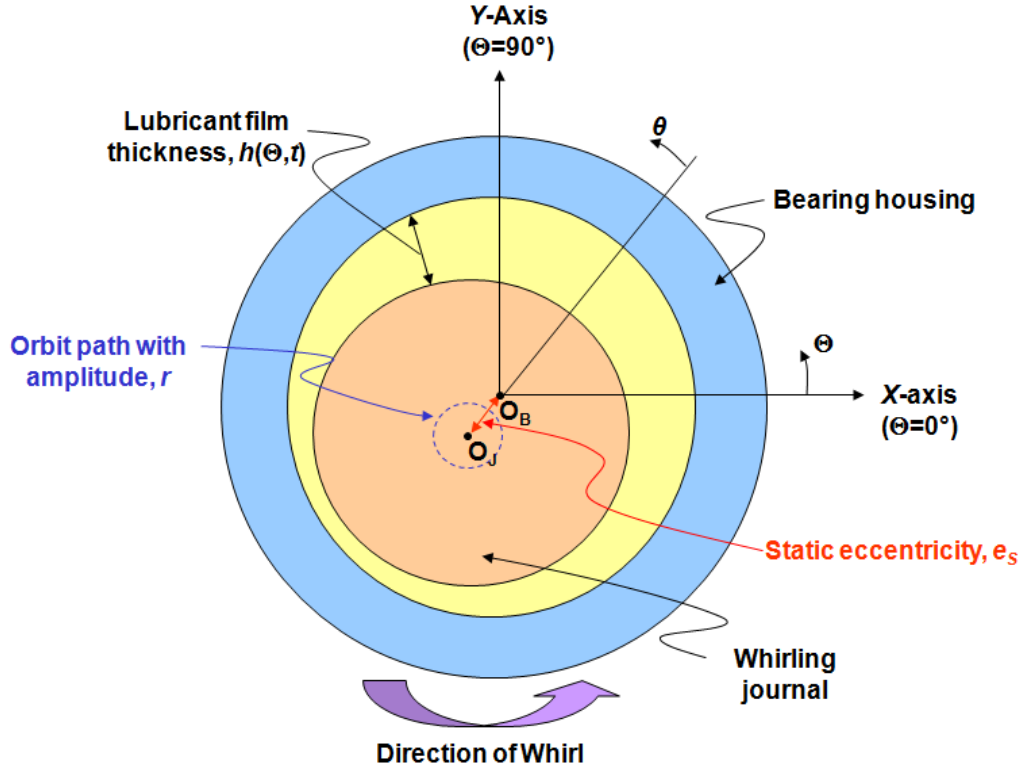
Figure 1. Schematic top view representation of a simple SFD showing operating parameters and coordinate system

Modified Reynolds Equation and Force Coefficients

The classical Reynolds equation for lubrication theory assumes negligible fluid inertia effects. However, the squeeze film Reynolds number $\mathrm{Re}_S = \dfrac{\rho \omega c^2}{\mu}$ gives a measure as to how considerable of a role fluid inertia has on the generation of the dynamic pressure field. In general, fluid inertia effects are important when [45]

$$\frac{\mathrm{Re}_S}{\tilde{\kappa}_z} \geq 1 \tag{3}$$

where the flow shear parameter $\tilde{\kappa}_z = 12$ for laminar flow. Typically, fluid inertia effects must be accounted for in the analysis of SFDs due to their relatively large clearances, use of light viscous lubricants, and operation at high frequencies, which all lead to an increase in Re_S. The modified Reynolds equation governing the generation of the SFD fluid film dynamic pressure field P, including first order fluid inertia effects[3] and considering laminar flow, is [10]

$$\frac{\partial}{\partial x}\left(h^3\frac{\partial P}{\partial x}\right) + \frac{\partial}{\partial z}\left(h^3\frac{\partial P}{\partial z}\right) = 12\mu\frac{\partial h}{\partial t} + \rho h^2\frac{\partial^2 h}{\partial t^2} \tag{4}$$

Using the assumption of a full lubricant film (i.e. without cavitation), open-ends SFD prescribing small amplitude motions ($r/c<0.25$), the modified Reynolds equation is solved analytically to produce the following direct damping (C^*) and mass (M^*) coefficients [6]

$$C^*_{XX} = C^*_{YY} = C^*_{tt} = 12\pi\frac{\mu R^3 L}{c^3}\left[1 - \frac{\tanh\left(L/D\right)}{\left(L/D\right)}\right] \tag{5}$$

and

$$M^*_{XX} = M^*_{YY} = M^*_{rr} = \pi\frac{\rho R^3 L}{c}\left[1 - \frac{\tanh\left(L/D\right)}{\left(L/D\right)}\right] \tag{6}$$

Note that SFDs do not generate stiffness coefficients or reactions forces due to static journal displacements. Later the force coefficients presented in Chapter VI are non-dimensionalized by dividing the actual experimental coefficients by C^* and M^*.

---

[3] This equation considers temporal fluid inertia effects only.

CHAPTER III

EXPERIMENTAL APPARATUS

This chapter describes the SFD experimental apparatus, broken down into its mechanical assembly, instrumentation, lubrication system, and data acquisition system. The test rig was originally built in 2009 for investigation of differing damper geometries [42, 43]. Since, some components were updated reconfigured for the current analysis. The chapter describes the apparatus as configured for the current research only.

Test Rig Mechanical Assembly

Figure 2 depicts the SFD test rig. The test rig consists of two orthogonally placed electromagnetic shakers (max 2450 N [550 lb$_f$], 500 Hz) to excite the test bearing and a hydraulic puller (max 17.8 kN [4 klb$_f$]) located 45° away from the X and Y shakers to create statically eccentric test bearing conditions.
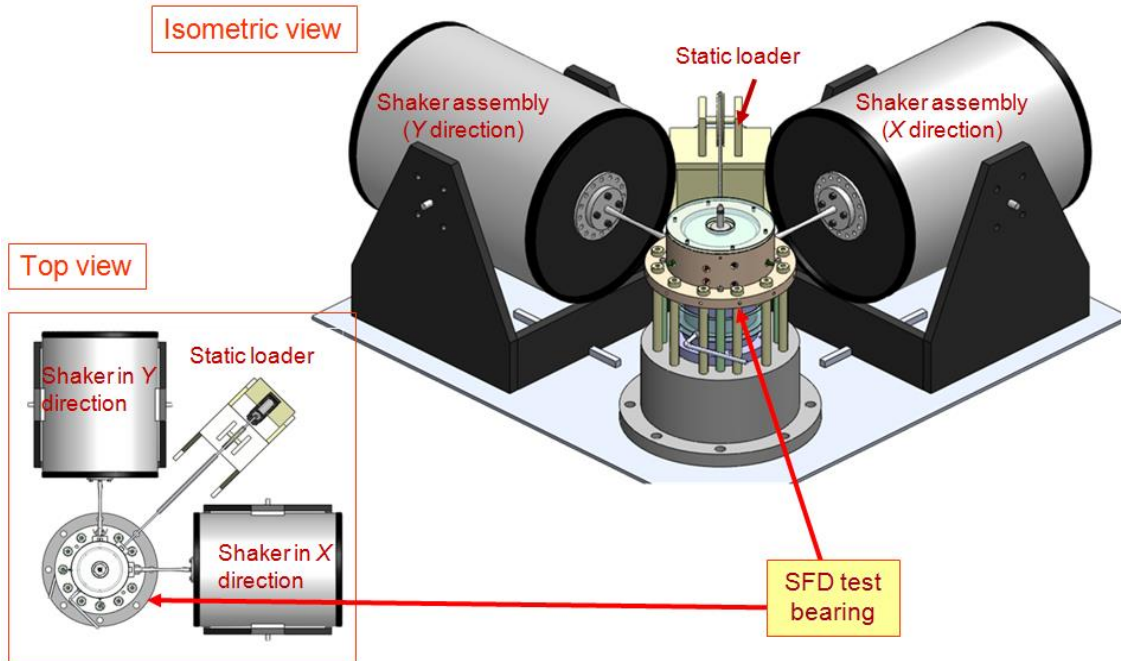
Figure 2. Schematic showing overview of SFD test rig (isometric and top views)

The SFD test bearing, shown in Figure 3, consists of a rigid pedestal and journal base that bolt to the test stand table. The journal base supports the test journal, which makes the inner surface of the squeeze film land. Flexural support rods, attached to the pedestal, support the bearing cartridge (BC), which makes the outer surface of the squeeze film land. The shakers excite the bearing cartridge (through slender stingers) to create a squeeze of lubricant supplied to the annulus between the stationary journal and BC. Variations in number of flexural support rods provide flexibility in achieving desired test rig stiffness.
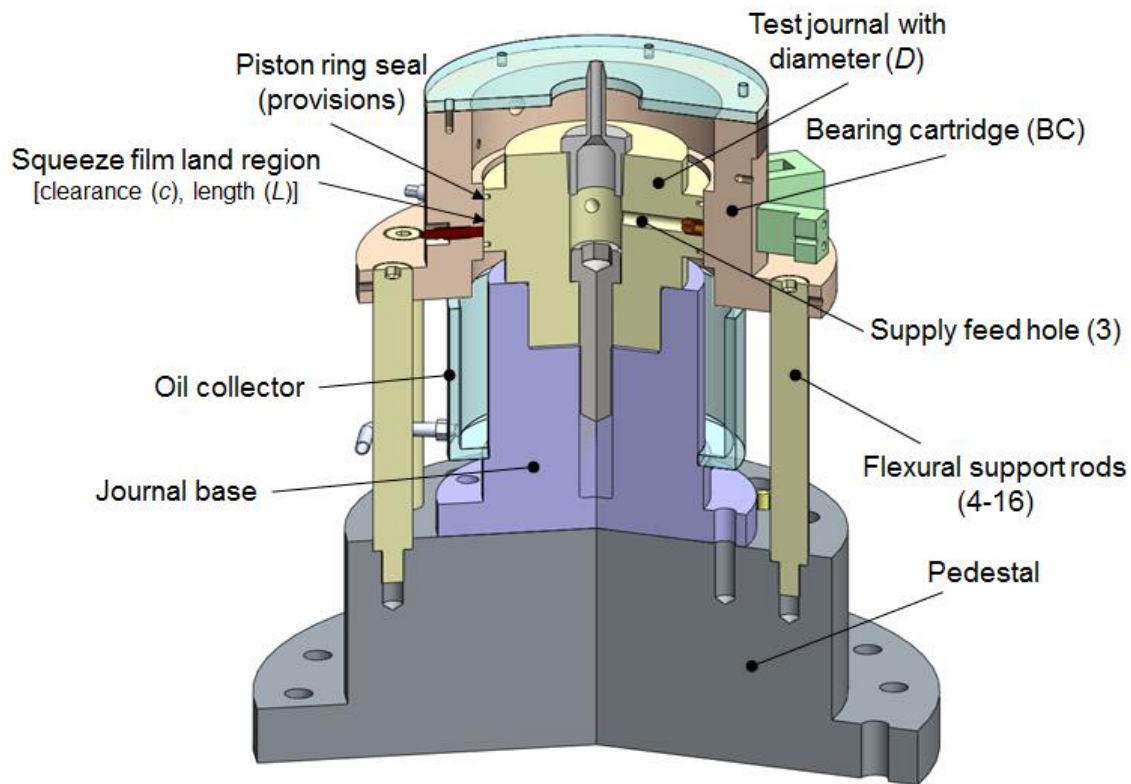
Figure 3. Cut-section view of the SFD test bearing section

The SFD test rig accommodates a damper configuration akin to those existing in industrial gas-turbine aircraft engines[4]. This configuration feeds lubricant directly to the

---

[4] In a real application, the SFD is fed lubricant from the bearing cartridge. In addition, the journal is the component that whirls or vibrates while the bearing cartridge is fixed. For simplicity and ease of testing,

mid plane of a single film land via three radial orifice feed holes (spaced 120° apart). Figure 4 shows a schematic view of the damper configuration with a $D=127$ mm (5 in.) diameter journal. The damper axial land length (L) and clearance (c) are 25.4 mm (1 in.) and 0.127 mm (5 mil), respectively, ($L/D=0.2$). The damper journal has end grooves for installation of piston ring seals.
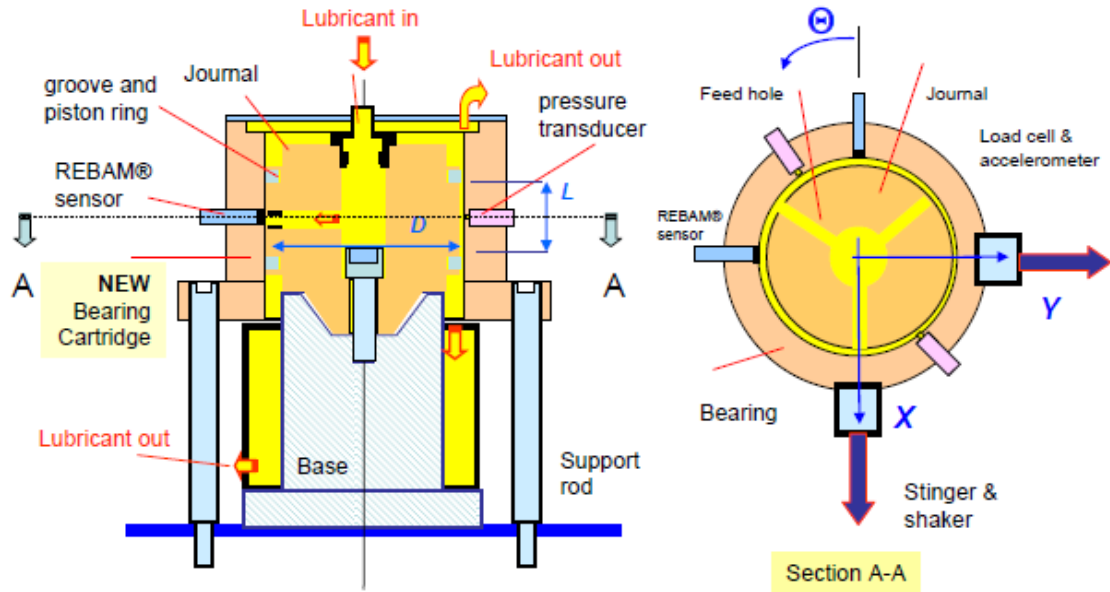
Figure 4. Schematic showing test damper configuration (cut-section view)

In operation, ISO VG 2 lubricant at room temperature (~22°C) flows into the test bearing section thru a hole in the center of the stationary journal. The lubricant is routed to the mid axial plane of the squeeze film land via three holes with orifice diameter equal to 2.56 mm (0.101 in.) and spaced 120° apart. The flow rate and pressure of lubricant into the damper are manually controlled. The BC is excited (at a specified orbit amplitude, r) by the shakers to produce unidirectional, circular, or elliptical orbits about the stationary journal (simulating an actual SFD operation in which the journal whirls inside the bearing housing).

---

the test rig feeds lubricant to the film land via holes in the journal, and excites the bearing cartridge while the journal is stationary. It is assumed that the flow patterns in the test rig are similar to those of an actual application, because the relative motion between the journal and BC is the same.

Test Rig Instrumentation

Bently Nevada REBAM® eddy current sensors installed in the BC record the relative displacement (x, y) between the BC and journal along the X,Y-axes. PCB accelerometers attached to the BC record the BC absolute acceleration (a_X, a_Y) along the X,Y–axes. Load cells attached to the shaker excitation stingers record the dynamic excitation force (F_X, F_Y). Dynamic and static pressure sensors installed around the BC record damper film land pressures (P) for identification and analysis of lubricant gaseous phenomena. K-type thermocouples measure the lubricant supply temperature (T_S) and ambient air temperature (T_a). A stain gauge type load cell measures the force required to statically offset the BC along the 45° direction.

Figure 5 shows a schematic "unwrapped" 360° side view of the BC outlining the disposition of instrumentation. Table 1 lists all instrumentation for the SFD test rig and indicates the sensor functionality.
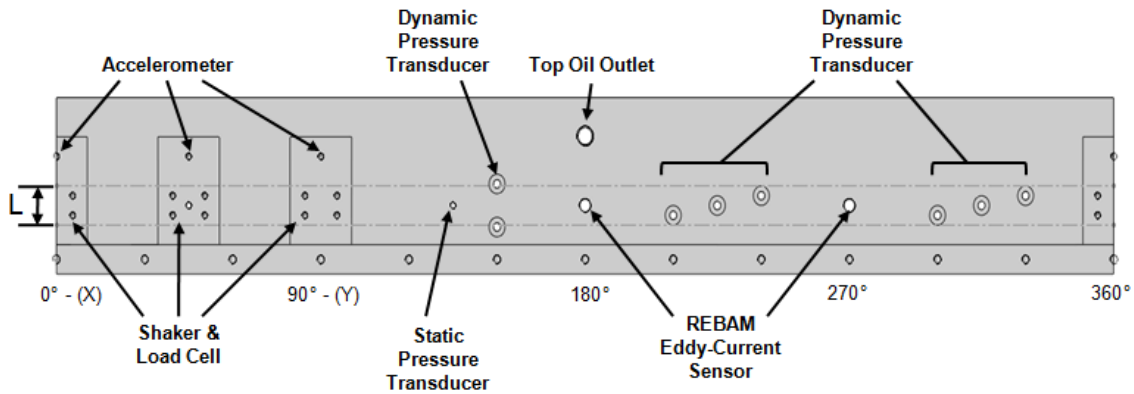
Figure 5. Unwrapped side view of BC showcasing the disposition of instrumentation

Table 1. Instrumentation installed on the SFD test rig with manufacturer and functionality outlined

	Sensor Type (Qty)	Manufacturer	Model	Rated Sensitivity	Measurement Variable
Mounted inside BC	Piezoelectric Load Cell (2)	PCB	208C03	10 mV/lb	Dynamic load on BC applied by shakers along *X* and *Y* directions
	Piezoelectric Accelerometer (2)	PCB	353B33	100 mV/g	BC accelerations along *X* and *Y* axes
	Strain Gage Load Cell (1)	Omega	LC213-500	0.04 mV/lb	Magnitude of force applied on BC thru static loader
	Eddy Current (2)	Bently-Nevada	3300 REBAM	1.0 V/mil	BC displacement with respect to Journal along *X* and *Y* axes
	Strain Gage Static Pressure (2)	Measurement Specialties	EPX-V13	1.25 mv/psi	Static pressure of lubricant in film land
	Piezoelectric Dynamic Pressure (8)	PCB	111A26	10 mV/psi	Dynamic pressure in throughout film land
Mounted outside BC	Strain Gage Pressure Transducer (1)	Omega	PX313-100G5V	.05 mV/psi	Inlet pressure of lubricant in supply line before entering journal
	Flowmeter (1)	Omega	FTB791		Lubricant flow rate into journal
	Thermocouple (3)	Omega	K type	.04 mV/F	Temperature of lubricant at journal inlet, top exit and bottom exit of film land

Test Rig Lubrication System

Figure 6 shows a schematic of the lubricant system for the SFD test rig. The ISO VG 2 oil is stored at room temperature in a 150L storage tank. A 3.5kW pump delivers the oil to the SFD test bearing. The delivery line contains an oil filter for removing debris, a turbine type flowmeter for measuring inlet flow rate Q_{in}, and a bourdon type pressure gauge for measuring the supply pressure P_S. The oil flows through the top and bottom portions of the film land with flow rate Q_T and Q_B, respectively. A 0.75kW pump then delivers oil back to the lubricant storage tank. The lubrication system includes a pressure relief valve in the delivery line and a by-pass line, for proper safe handling.
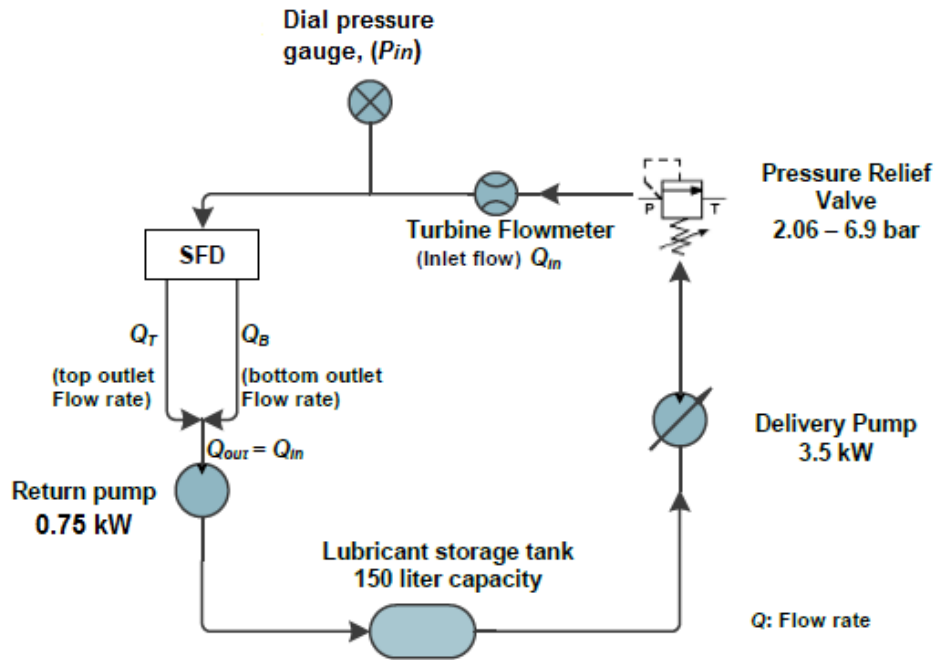
Figure 6. Schematic view of lubricant system for test rig

Test Rig Data Acquisition (DAQ)

The data acquisition system (DAQ) consists of a National Instruments cDAQ-9172 board supporting up to 32 instrument channels. All instrumentation signals (including shaker controllers) are connected to the DAQ board after appropriate signal conditioning. The DAQ board is connected to a PC running Microsoft Windows XP with National Instruments LabVIEW 8.6 software. A custom virtual instrument (VI) allows for recording of all sensor voltages and for output signals to be sent to the shaker amplifiers. User inputs to the VI include sensor gains, excitation frequency (ω), orbit amplitude (r_X, r_Y), and phasing of the *X* and *Y* shakers. The VI automatically adjusts the voltages into the shaker amplifiers to deliver single frequency periodic loads that will produce the desired orbit amplitude (r_X, r_Y). Once the desired orbit amplitude is obtained and the system reaches a (quasi) steady state, the VI records and saves data from all instrumentation. This procedure is performed at several pre-selected whirl frequencies (usually between 10-250 Hz, in steps of 10 Hz). Note the signals from the instrumentation are stored as voltages over a given time span. Typically the sampling rate equals $1.638 \cdot 10^4$ (2^{14}) samples/sec and the elapsed time for a test is 0.25 sec. Hence, the number of saved samples at discrete time intervals equals to 4,096.

Figure 7 shows a wiring diagram from the test rig instrumentation to the user PC. Figure 8 shows the main graphical user interface (GUI) of the LabVIEW VI and notes inputs, outputs, etc. Note, the DAQ gives graphs of real-time measurements for user verification during testing. In addition the load cells, accelerometers, and proximitors are connected to oscilloscopes for real time orbit verification.
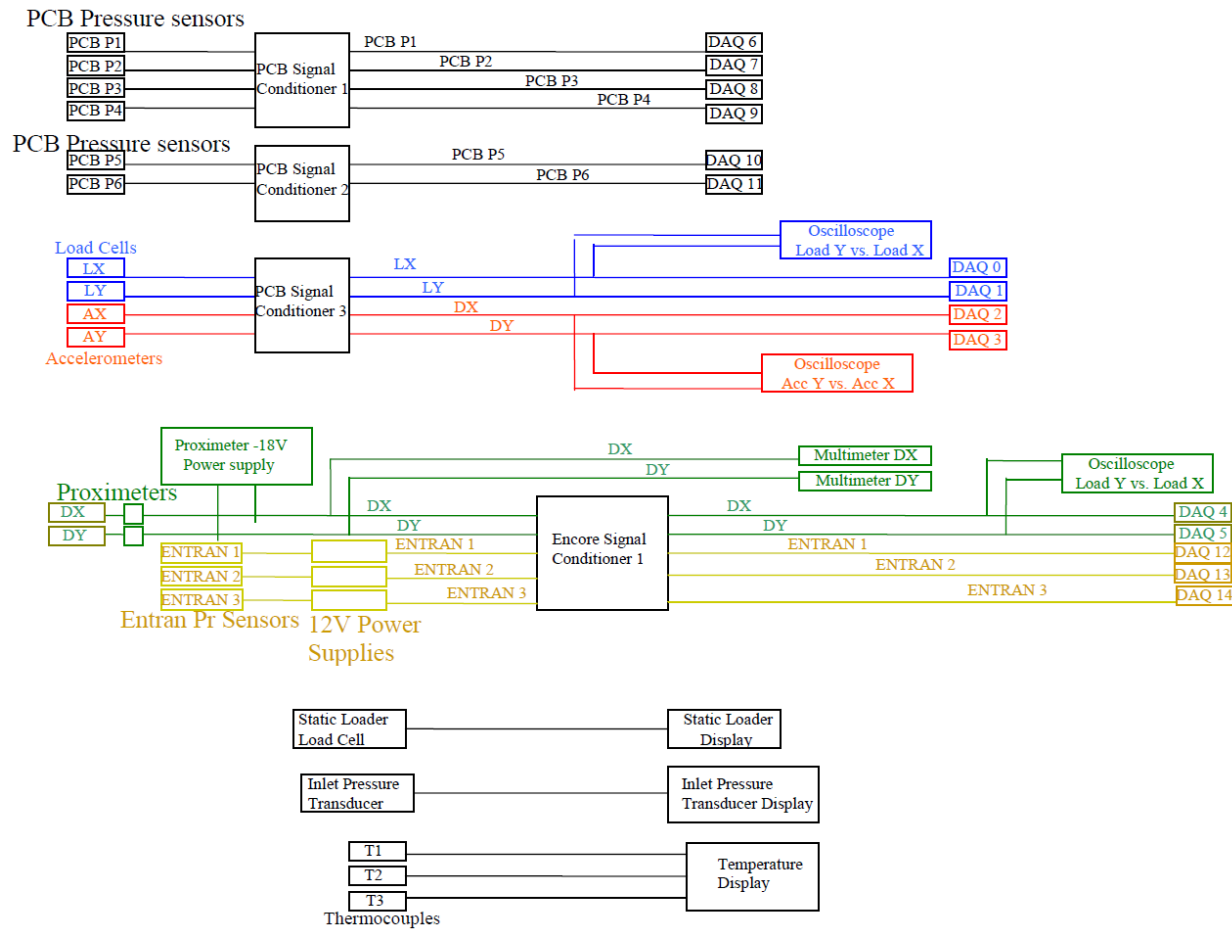
Figure 7. Wiring diagram for data acquisition on SFD test rig
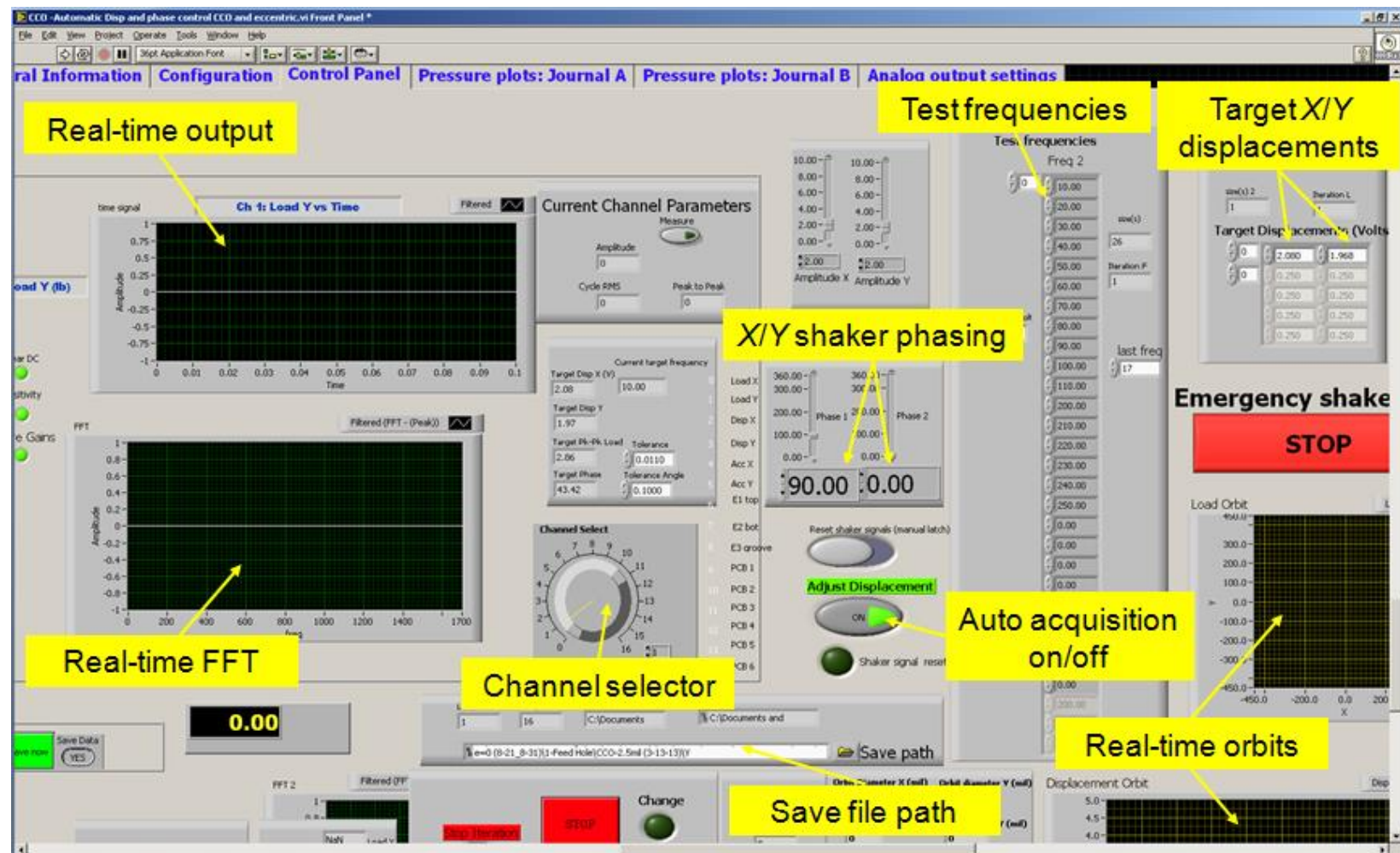
Figure 8. View of LabView VI GUI indicating the user inputs and outputs

CHAPTER IV

EXPERIMENTAL PROCEDURE

A 2-DOF K-C-M model describes the test system, as shown in Figure 9. The model includes mechanical parameters from both the structure $(\mathbf{K}, \mathbf{C}, \mathbf{M})_S$ and the SFD $(\mathbf{K}, \mathbf{C}, \mathbf{M})_{SFD}$, in which each matrix is 2×2 with direct and cross-coupled coefficients, for example $\mathbf{K}_S = \begin{bmatrix} K_{XX} & K_{XY} \\ K_{YX} & K_{YY} \end{bmatrix}_S$.
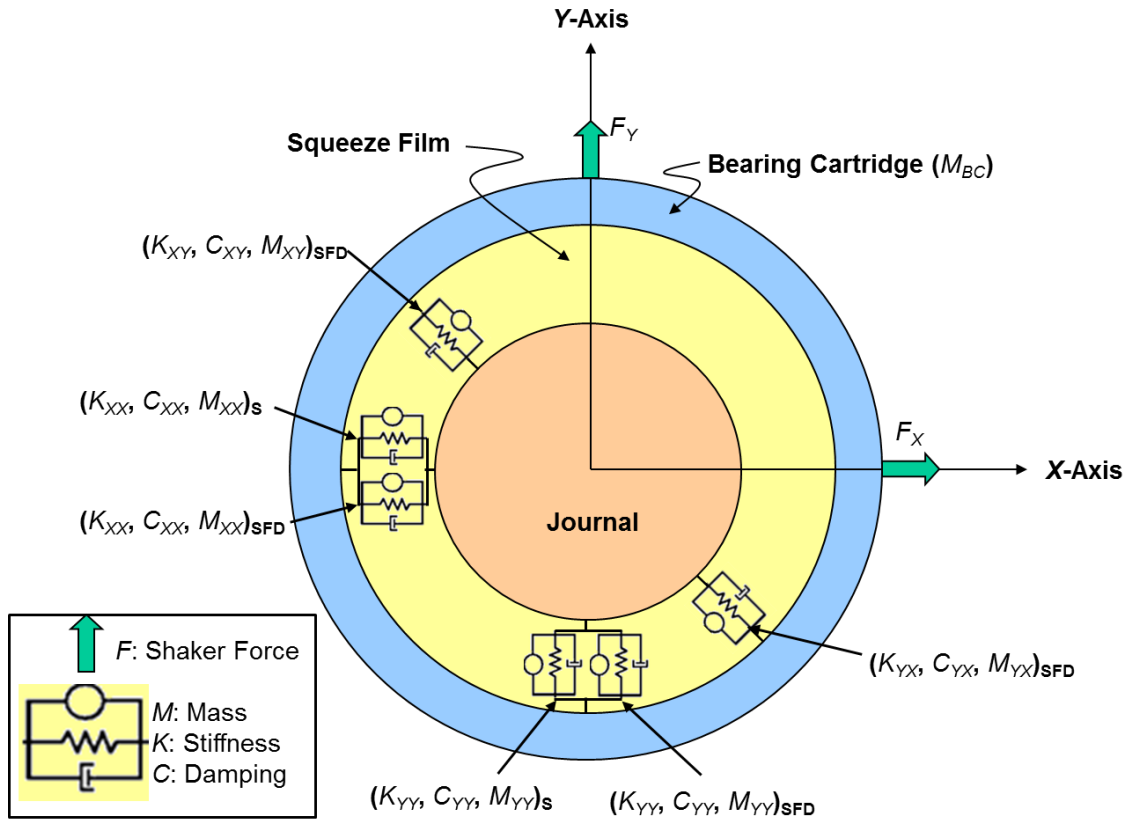
Figure 9. Schematic representation of the SFD test system as a collection of mechanical parameters (K, C, M)

Identification of the SFD stiffness, damping, and mass coefficients $(\mathbf{K}, \mathbf{C}, \mathbf{M})_{SFD}$ is a multistep process. Initially, the structural parameters of the dry test system $(\mathbf{K}, \mathbf{C}, \mathbf{M})_S$ are determined using an identification method as outlined below. The wet (lubricated) test system structural parameters $(\mathbf{K}, \mathbf{C}, \mathbf{M})$ are determined using the same identification

method. The SFD force coefficients are obtained by subtracting the dry system coefficients from the lubricated system coefficients. That is[5]

$$(\mathbf{K}, \mathbf{C}, \mathbf{M})_{SFD} = (\mathbf{K}, \mathbf{C}, \mathbf{M}) - (\mathbf{K}, \mathbf{C}, \mathbf{M})_S \qquad (7)$$

In addition to identification of force coefficients, it is important to experimentally measure lubricant properties (viscosity and density) and flow characteristics, such as the supply pressure and inlet/outlet flow rates. Knowledge of these properties aids in accurately predicting SFD forces from numerical models.

This chapter outlines the experimental procedures for dynamic load tests, the parameter identification procedure, and the operating conditions for experiments. Appendix A describes the procedure and results for static load tests and measurements of lubricant physical properties and flow characteristics.

Dynamic Load Test

Dynamic load tests are conducted using the LabView VI described in Chapter III. First, the desired test conditions (whirl amplitude, frequency range, orbit type) are input into the VI. Statically offset conditions are also set at this time by displacing the BC via the static loader. Next, the VI is run and sends voltage signals to the electromagnetic shakers to excite the BC. The VI contains a control algorithm that measures real time BC displacement and automatically adjusts the voltage outputs to achieve the input orbit type and amplitude at the first frequency step. Once the desired conditions are met, the VI holds the voltage signal and records all measurements for ~0.25 seconds. The VI then adjusts the voltage signals to meet the input conditions at the next frequency step. This process continues until all input frequency steps are complete. This procedure conducts numerous single frequency dynamic load tests across an entire frequency range. The minimum number of frequencies needed for the parameter identification procedure is 3. Additionally the parameter identification requires two linearly independent load vectors, which calls for two different tests at each frequency.

---

[5] Equation 7 assumes the test mechanical system is linear

Note, the VI control algorithm adjusts the shaker voltage based on the measured BC/journal relative displacement. Ideally, the journal should be stationary due to the large stiffness of the pedestal and journal base. However, at certain frequencies the test rig table is excited and creates movement of the journal. This journal motion is accounted for in the identification procedure, but not in the VI control system. There is not an issue when the journal motion is in phase with the BC excitation, however as the journal motion becomes out of phase, the control system has problems adjusting and meeting the desired input whirl amplitude. Frequencies in which the control system fails to properly meet the desired input test conditions are eliminated from use in parameter identification. Appendix B details the process to reject this data.

Parameter Identification Procedure

The following outlines the procedure for identification of SFD force coefficients from experimental measurements. This procedure is updated from that given in Ref. [42], with some portions reproduced ad verbatim.

First, the shakers excite the BC with two independent single frequency (periodic) loads. For unidirectional excitations, the load vectors are

$$
\mathbf{F}_1 = \begin{bmatrix} F_{X_{(t)}} \\ 0 \end{bmatrix}; \quad \mathbf{F}_2 = \begin{bmatrix} 0 \\ F_{Y_{(t)}} \end{bmatrix} \tag{8}
$$

which excite the BC only along the X axis and then only along the Y axis, respectively. For whirl orbit tests (circular), the two independent load vectors are

$$
\mathbf{F}_1 = \mathrm{Re}\left(\begin{bmatrix} F_{X_1} \\ i \cdot F_{Y_1} \end{bmatrix} e^{i\omega t} \right)
$$

$$
\mathbf{F}_2 = \mathrm{Re}\left(\begin{bmatrix} F_{X_2} \\ -i \cdot F_{Y_2} \end{bmatrix} e^{i\omega t} \right)
\tag{9}
$$

creating clockwise and counterclockwise whirl motions. Note the phase difference between the X and Y loads is +90° and -90°, respectively.

Figure 10 shows a simple free body diagram (FBD) of the bearing cartridge and the forces acting on it. **F** denotes the vector of excitation forces from the external shakers. The reaction force from the support structure (**F$_S$**) is a function of its stiffness, damping, and mass coefficients, (**K, C, M**)$_S$. When lubricated, the squeeze film damper reacts with force (**F$_{SFD}$**).
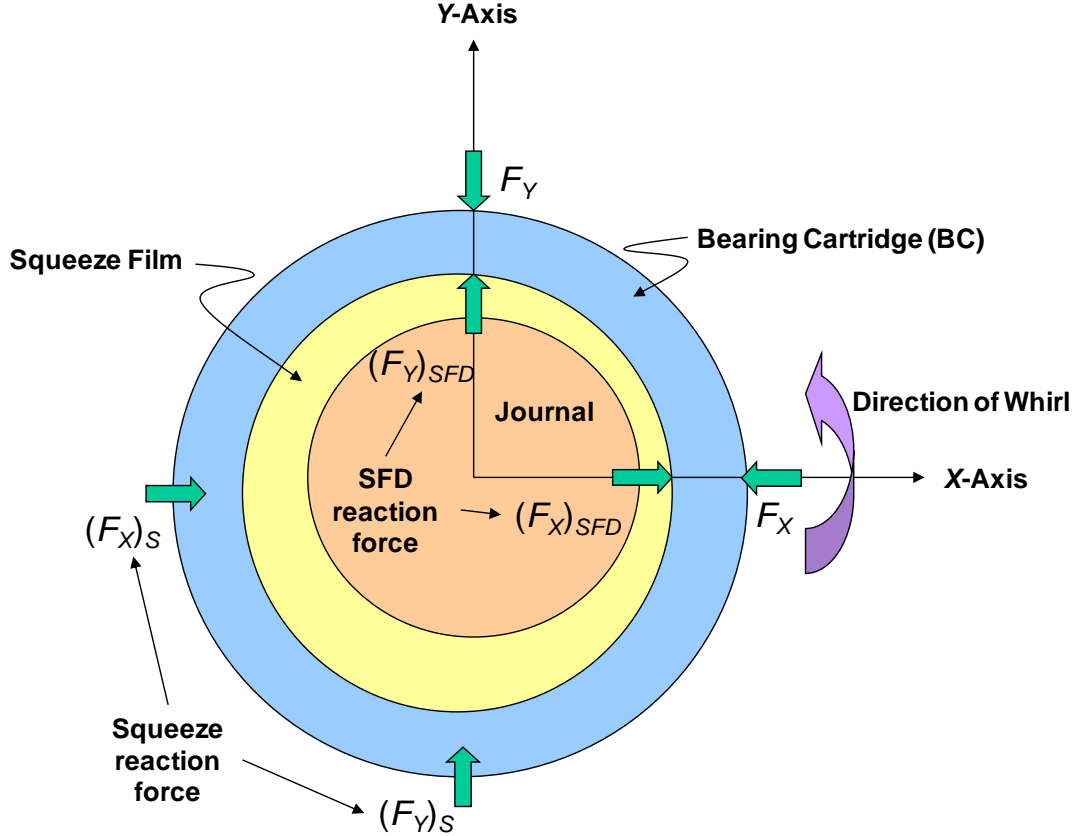
Figure 10. Schematic view of bearing cartridge and forces acting on it

The equation of motion for the (rigid) bearing cartridge is

$$M_{BC} \begin{pmatrix} a_X \\ a_Y \end{pmatrix} = \begin{pmatrix} F_{X_{(t)}} \\ F_{Y_{(t)}} \end{pmatrix} - \begin{pmatrix} F_X \\ F_Y \end{pmatrix}_S - \begin{pmatrix} F_X \\ F_Y \end{pmatrix}_{SFD} \quad \text{or} \quad M_{BC}\,\mathbf{a} = \mathbf{F} - \mathbf{F_S} - \mathbf{F_{SFD}} \tag{10}$$

where M_{BC} is the mass of the BC and $\mathbf{a}=(a_X, a_Y)^\mathrm{T}$ is the BC absolute acceleration. $\mathbf{F}=(F_X, F_Y)^\mathrm{T}$ is the vector of external (periodic) loads exerted by the shakers, $\mathbf{F_S}=(F_X, F_Y)_s{}^\mathrm{T}$ is

the reaction force from the support structure, and $\mathbf{F_{SFD}}=(F_X, F_Y)_{SFD}^T$ is the squeeze film damper force.

The reaction force from the support structure and SFD are modeled, respectively, as

$$\mathbf{F_S} = \mathbf{M}_S\ddot{\mathbf{z}} + \mathbf{C}_S\dot{\mathbf{z}} + \mathbf{K}_S\mathbf{z} \tag{11}$$

and

$$\mathbf{F_{SFD}} = \mathbf{M}_{SFD}\ddot{\mathbf{z}} + \mathbf{C}_{SFD}\dot{\mathbf{z}} + \mathbf{K}_{SFD}\mathbf{z} \tag{12}$$

Vector $\mathbf{z}=(x,y)^T$ is the relative displacement between the BC and journal. ($\mathbf{K_S}$, $\mathbf{C_S}$, $\mathbf{M_S}$) and ($\mathbf{K_{SFD}}$, $\mathbf{C_{SFD}}$, $\mathbf{M_{SFD}}$) are matrices containing the stiffness, damping, and added mass coefficients of the structure and SFD, respectively. The structure and SFD reaction forces act in parallel, thus the force coefficients can be combined as

$$\mathbf{M} = \mathbf{M}_S + \mathbf{M}_{SFD}, \quad \mathbf{C} = \mathbf{C}_S + \mathbf{C}_{SFD}, \quad \mathbf{K} = \mathbf{K}_S + \mathbf{K}_{SFD} \tag{13}$$

Simplifying the EOM to

$$\mathbf{M}\ddot{\mathbf{z}} + \mathbf{C}\dot{\mathbf{z}} + \mathbf{K}\mathbf{z} = \mathbf{F}_{(t)} - M_{BC}\mathbf{a}_{(t)} \tag{14}$$

In the frequency domain, the equation of motion becomes

$$\left[\mathbf{K} - \omega^2\mathbf{M} + i\omega\mathbf{C}\right]\overline{\mathbf{z}}_{(\omega)} = \overline{\mathbf{F}}_{(\omega)} - M_{BC}\overline{\mathbf{a}}_{(\omega)} = \overline{\mathbf{P}} \tag{15}$$

where $\overline{\mathbf{z}}_{(\omega)}$, $\overline{\mathbf{F}}_{(\omega)}$, $\overline{\mathbf{a}}_{(\omega)}$ are the Discrete Fourier coefficients of $\mathbf{z}_{(t)}$, $\mathbf{F}_{(t)}$, $\mathbf{a}_{(t)}$, respectively.

The mechanical impedance matrix $\mathbf{H}$ is defined as

$$\mathbf{H}_{(\omega)} = \begin{bmatrix} H_{XX} & H_{XY} \\ H_{YX} & H_{YY} \end{bmatrix} = \overline{\mathbf{P}} \cdot \left[\overline{\mathbf{z}}_1 \ \overline{\mathbf{z}}_2\right]^{-1} \tag{16}$$

in which $\overline{\mathbf{F}}_1$ and $\overline{\mathbf{F}}_2$ are the two linearly independent forces and $\overline{\mathbf{z}}_1$ and $\overline{\mathbf{z}}_2$ are the corresponding linearly independent displacements. $\overline{\mathbf{a}}_1$ and $\overline{\mathbf{a}}_2$ are the corresponding BC absolute accelerations. The test system impedance, as calculated by measured quantities, equals

$$\mathbf{H}_{(\omega)} = \left[\mathbf{K} - \omega^2\mathbf{M} + i\omega\mathbf{C}\right] \tag{17}$$

Preliminary estimates of the system parameters $\{K, C, M\}_{i,j=X,Y}$ are determined by curve fitting of the discrete set of impedances $(H_{XX}, H_{YY}, H_{XY}, H_{YX})_{k=1,2\ldots}$, one set for each

frequency ω_k, to the analytical formulas over a pre-selected frequency range. That is, for example,

$$\text{Re}(H_{XX}) \to K_{XX} - \omega^2 M_{XX}; \quad \text{Im}(H_{XX}) \to \omega C_{XX} \tag{18}$$

The instrumental variable filter method (IVFM) [36] is then employed to reduce measurement noise and better predict the force coefficients. This method uses the flexibility matrix $\mathbf{G}=\mathbf{H^{-1}}$ rather than directly curve fitting the mechanical impedances. Note that $\mathbf{GH} = \mathbf{I}$, the identity matrix; however, due to measurement or procedure noise there is always an error (**e**), i.e.,

$$\mathbf{GH} = \mathbf{G}\left[\mathbf{K} - \omega^2\mathbf{M} + i\omega\mathbf{C}\right] = \mathbf{I} + \mathbf{e} \tag{19}$$

Minimization of the error (**e**) leads to the final identification equation

$$\begin{bmatrix} \mathbf{M} \\ \underline{\mathbf{C}} \\ \mathbf{K} \end{bmatrix} = (\mathbf{W}^{\mathbf{T}}\mathbf{W})^{-1}\mathbf{W}^{\mathbf{T}}\mathbf{I} \tag{20}$$

where $\mathbf{W}^K = \mathbf{G}^K(\mathbf{I} \vdots - \omega^2\mathbf{I} \vdots i\omega\mathbf{I})$. Eq. (20) is a typical least-squares error estimator.

Finally, the SFD force coefficients (**K, C, M**)$_{SFD}$ are found by subtracting the *structure* force coefficients from the total system coefficients. Note that when the system operates in a "dry" condition the SFD force coefficients are nil, and thus the derived coefficients are the structure force coefficients.

$$(\mathbf{K, C, M})_{SFD =} (\mathbf{K, C, M}) - (\mathbf{K, C, M})_S \tag{21}$$

It is important to note that the identified force coefficients are obtained from test data within a certain frequency range. Hence, the force coefficients are valid only for the specific frequency range of the experiments.

Operating Conditions for Experiments

Comprehensive dynamic load measurements conducted on the SFD test rig aim to assess the effects of BC static eccentricity (e_S), amplitude (r) and frequency (ω) of BC whirl motions, and the feed configuration (central groove vs. direct feed holes) on the

test element force coefficients, mainly squeeze film damping and inertia force coefficients.

The test SFD operates with its axial ends open to ambient (i.e., without end seals). ISO VG 2 lubricant, with measured viscosity μ=2.5 cP (0.362 micro-Reyns) at supply temperature T_S=22.2°C (72°F) and density ρ=799.3 kg/m^3 (49.9 lb/ft^3), flows into the test section thru a hole in the center of the stationary journal. The lubricant is routed to the axial mid-plane of the squeeze film land via three holes with orifice diameter = 2.57 mm (0.101 inch) and spaced 120° apart. The flow rate of lubricant into the damper is maintained at Q_{in}=5.03 LPM (1.33 GPM), as with the prior tested dampers [42, 43]. The lubricant feed pressure well upstream of the orifice feed holes is 1.62 bar (23.5 psig), while the supply pressure (P_S) measured at the exit of one orifice feed hole is P_S=0.97 bar (14 psig)[6]. Appendix A details the measurement of the lubricant physical properties (μ, ρ) and the flow characteristics (P_S, Q_{in}).

The identification procedure requires applying two linearly independent excitation forces to the test SFD. The excitation forces can be unidirectional loads, circular loads, or elliptical loads. Unidirectional loads are achieved by applying forces with either the *X* or the *Y* shaker, one at a time. Circular and elliptical loads are generated by applying periodic single frequency forces, along *X* and *Y*, and 90° out of phase to create orbital motions. Circular orbits have constant amplitude (*r*), while elliptical orbits have differing amplitudes ($r_X \neq r_Y$) along the *X*, *Y* directions.

Figure 11 depicts the different whirl paths induced on the SFD test section. Tests include circular and elliptical orbits (amplitude ratios r_X/r_Y = 1:1, 2:1 and 5:1) with whirl amplitudes varying over *r/c*=0.05 to 0.5 while also varying the static eccentricity ratio e_S/c=0.0 to 0.5. The frequency range for parameter identification is ω=10-250 Hz. At the largest test frequency (ω=250 Hz), the squeeze film Reynolds number is

$$\mathrm{Re}_S = \frac{\rho \omega c^2}{\mu} = 8.4 \ .$$

---

[6] The pressure sensor is ~5 mil away from the feed hole exit plane. The static pressure varies with the BC static eccentricity (closer/farther way from sensor). A more accurate measurement or estimation of the actual feed hole pressure is needed.
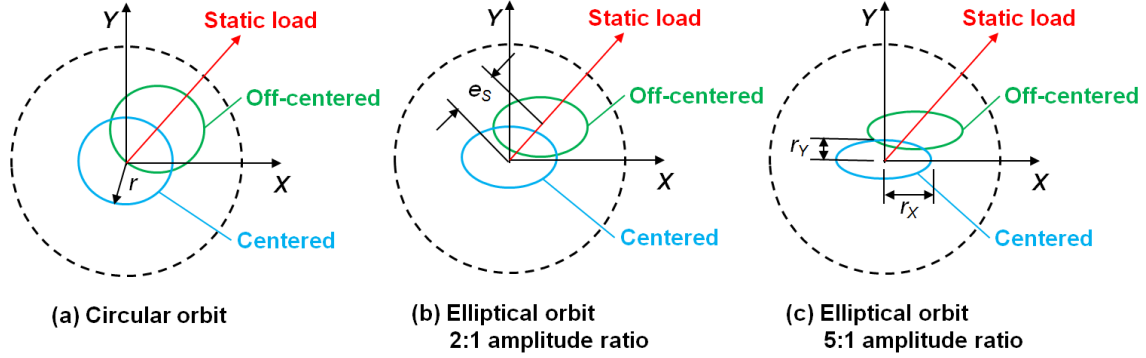
Figure 11. Schematic views of induced BC whirl motions, centered (blue) and off-centered (green): (a) circular orbits (b) elliptical orbits 2:1 amplitude ratio (c) elliptical orbits 5:1 amplitude ratio. Dotted lines represent the clearance circle

Table 2 lists the specific damper geometry and fluid properties and Table 3 summarizes the test variables for the experiments.

Table 2. Test damper geometry and oil properties

Nominal Journal diameter (D)	126.9 ± 0.003 mm [4.9964 ± 0.0001 inch]
Nominal Film clearance (c)	129 ± 2.5 μm [5.1 ± 0.1 mil]
Film land length (L)	25.4 ± 0.01 mm [1.0 inch]
End grooves: depth $\times$ width	3.81×2.54 mm [0.15×0.10 inch]
3 feed holes, diameter	2.57 ± 0.10 mm (120° apart)
Support Stiffness (K_S)	13.3 ± 0.2 MN/m [75.7 klb$_f$/inch]
BC mass (M_{BC})	15.15 ± 0.02 kg [33.4 lb]
ISO VG 2 viscosity (μ)	2.5 ± 0.025 cP @ T_S=$22.2 \pm 0.05°$C [0.362 micro-Reyns @ T_S=72°F]
ISO VG 2 density (ρ)	799.3 ± 0.02 kg/m^3 [49.9 lb/ft^3]

30

Table 3. Test conditions for experimentation

Ends Condition	Motion Type	Structure stiffness (MN/m)	Frequency Range (Hz)	Whirl amplitude r/c (-l)	Static eccentricity e_S/c (-)	Upstream supply pressure P_{in} (bar)	Flow rate Q_{in} (LPM)
Open	Circular 1:1	13.25	10-250	0.05 -0.6	0 – 0.5	1.62	5.03
	Elliptical 2:1, 5:1			0.05 – 0.6	0 – 0.5		

CHAPTER V

MEASUREMENTS OF FILM PRESSURES

Measurement of film land pressures gives insight to how the SFD pressure generation changes with excitation frequency (ω), whirl amplitude (r), and static eccentricity (e_S), as well as providing evidence on the occurrence and/or persistence of oil cavitation and/or air ingestion. This section discusses the major characteristics seen in recorded dynamic pressures measured with the current test damper.

Layout of Pressure Sensors

Figure 12 depicts the disposition of pressure sensors around the BC circumference as well as their placement along the BC axial length. Two strain-gauge type pressure sensors, noted as E_1 and E_2 record the static pressure at the mid plane of the film land ($z=0$). Two sets of three piezoelectric pressure sensors (P_{1-3}, P_{4-6}) measure the film land dynamic pressures at the top, mid plane and bottom sections of the film land length. The axial positions are $z=\frac{1}{4} L$, 0, $-\frac{1}{4} L$ for the noted planes. The sensors are staggered in the circumferential direction as shown in the unwrapped view in Figure 12. For reference, the placement of the middle plane transducers (P_4, P_1) is at angles $\Theta= 225°$ and $315°$, respectively. The top and bottom sensors are spaced $\pm 15°$ from this angular location. Two other piezoelectric pressure sensors (P_7, P_8) record the dynamic pressures in the grooves at the ends of the squeeze film land section, $z= \frac{1}{2} L$, $- \frac{1}{2} L$, as shown in the figure.
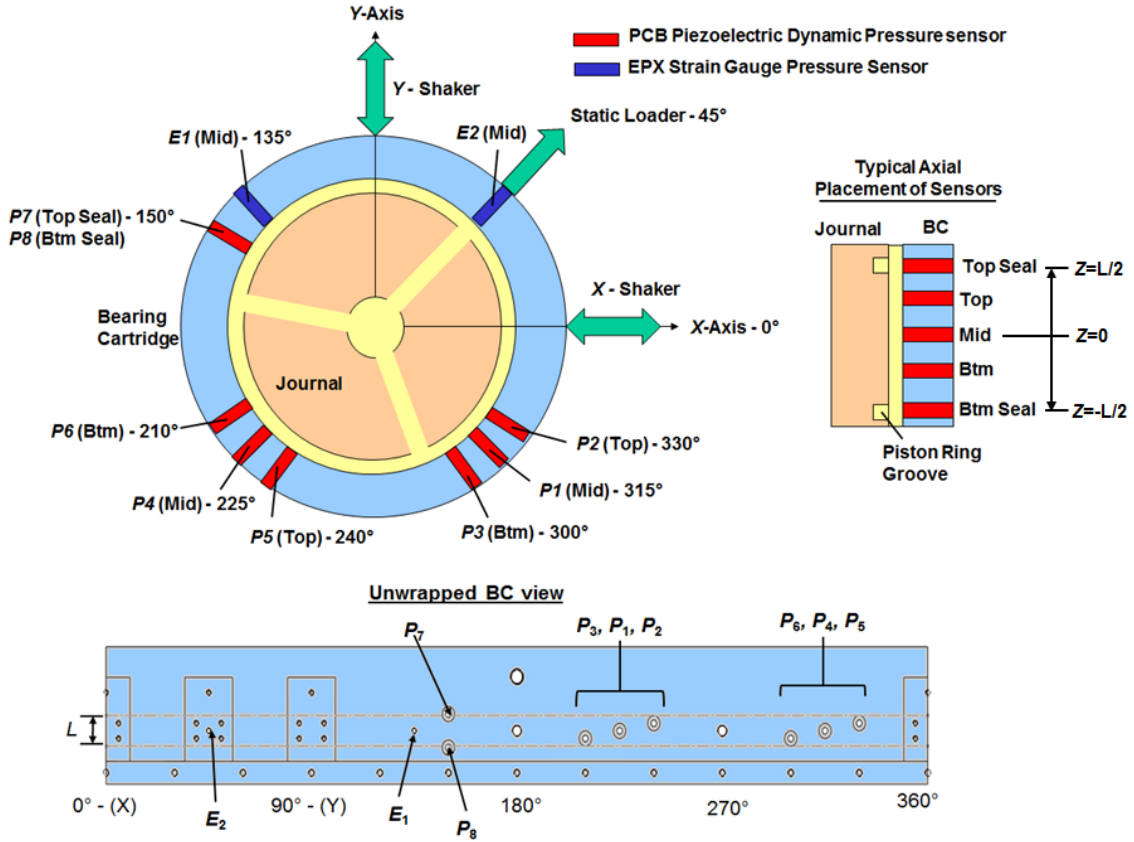
Figure 12. Schematic view showcasing disposition of pressure sensors in the test damper

Experimental Pressure Measurements

Figure 13 shows the measured peak-peak dynamic pressures from sensors P_1-P_8 versus excitation frequency (ω). The data corresponds to tests with a centered (e_S=0) circular orbit with radius r=0.30c. The test results show the dynamic pressures[7] at the top, middle and bottom planes of the film lands are proportional to the whirl frequency, i.e., $P{\sim}\omega$. As expected, the pressures at the film land mid-plane (z=0) are the largest. The top and bottom film pressures (z=±0.25L) are nearly similar in magnitude and at ~50% of the film pressure at the middle feed plane (z=0). Remarkably, the film pressures at the end groove locations are not equal to 0.

---

[7] Note the figure does not show data for $P6$ since the sensor did not function during the test.
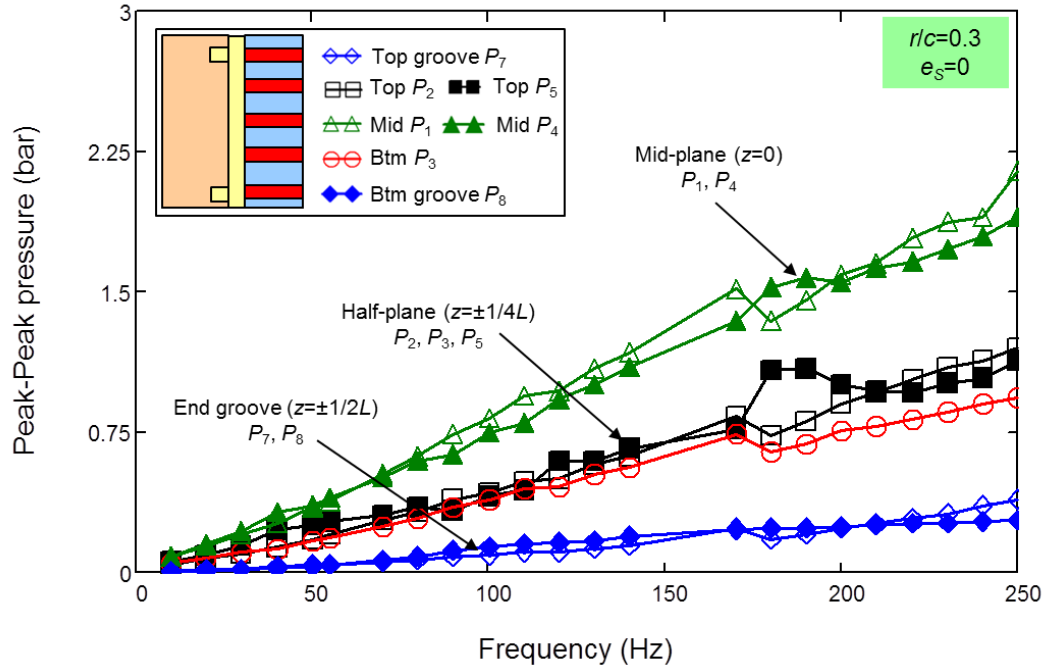
Figure 13. Recorded peak-to-peak film dynamic pressures versus excitation frequency. Centered circular orbit tests with radius *r/c*=0.30. Measurements at damper mid-plane, top and bottom (half-planes) and end grooves

Recall, the damper is configured in an open ends condition (i.e., no end seals are installed). The sensors P_7 and P_8 show peak-peak pressures in the end grooves that are not nil. In fact, at an excitation frequency of 250 Hz, the groove dynamic pressures are ~20% of those at the mid-plane pressure (P_1, P_4). The existence of significant dynamic pressures at the end grooves demonstrates that the grooves and end lips contribute to the SFD forces.

Figure 14 shows a schematic of the damper cross-section with an inset showing the end grooves with depth (3.87 mm) and width (2.49 mm) and the lips at the journal ends with a width of 3.18 mm. Hence, the physical length of the journal, including the film land (L=25.4 mm) and the two grooves and lips, equals L_{tot}=36.73 mm. Note the groove depth is ~ 30 times the nominal film clearance (c=129.54 μm).
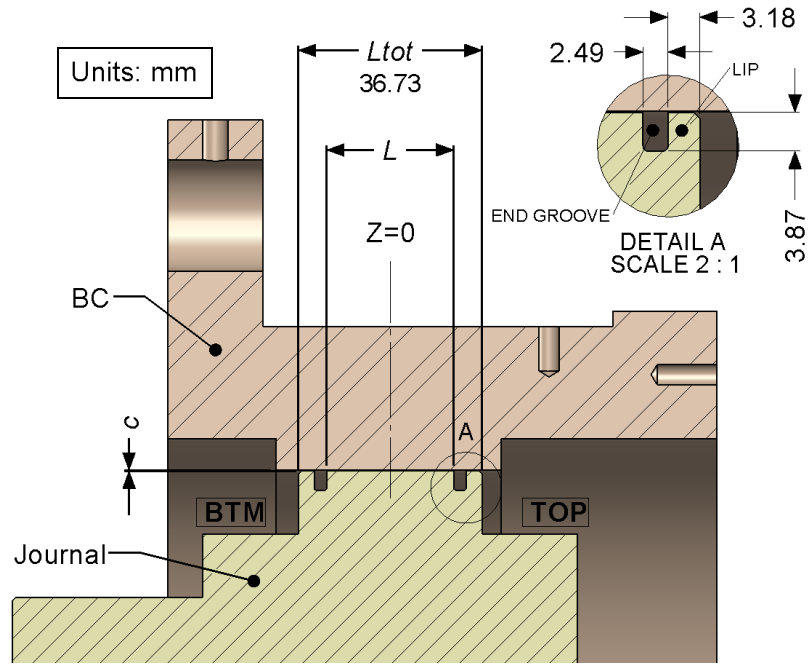
Figure 14. Cross-section schematic of SFD journal and BC showing the film land length (*L*) and adjacent groove and lip sections. Total damper length (*L_{tot}*) noted

Figure 15 and Figure 16 show the mid-plane (P_4) peak-peak dynamic pressures versus excitation frequency (ω) for all test orbit radii (r=0.05c-0.6c) at e_S=0 and all test static eccentricities (e_S=0-0.5c) at r=0.20c, respectively. Increases in both static eccentricity and orbit radius render increased peak-peak fluid film pressures. However, the film pressure tends to be more sensitive to increases in orbit amplitude than to increases in static eccentricity.
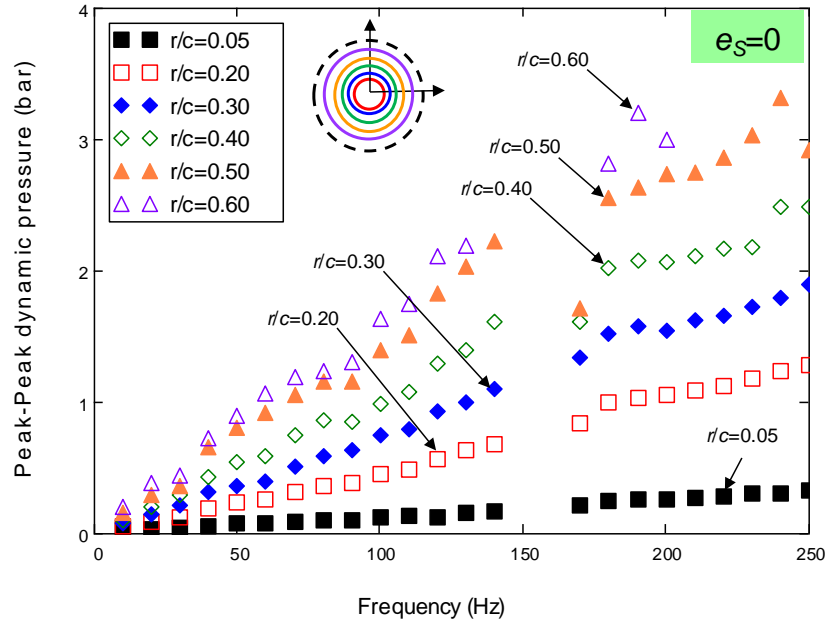
Figure 15. Measured mid-plane (P_4) peak-peak pressure versus whirl frequency for various orbit radii (r/c). Measurements for tests at a centered condition (e_S=0)
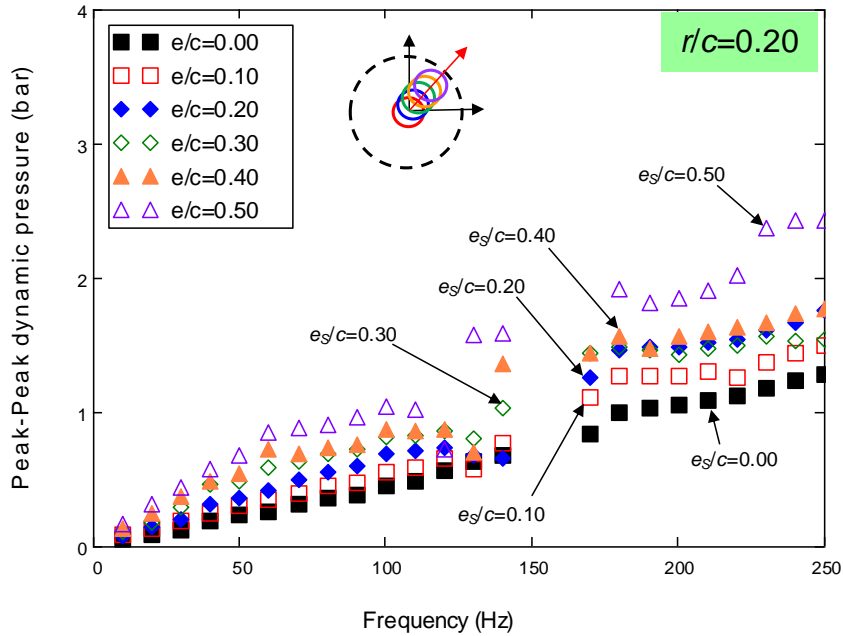
Figure 16. Measured mid-plane (P_4) peak-peak pressure versus whirl frequency for various static eccentricities (e_S). Measurements for tests with whirl amplitude r/c=0.20

Note the SFD dynamic pressure can be either viscous ($P_{viscous}{\sim}\omega$) or inertial ($P_{inertial}{\sim}\omega^2$) in nature or even most likely a combination of the two ($P \propto P_{viscous} + P_{inertial}$). The measurements presented above show some degree of proportionality to the whirl frequency ω. Following classical lubrication theory for the short length open ends SFD [10], a dimensionless pressure is defined as[8]

$$P^* = \frac{P_{P-P}}{\mu\omega\varepsilon}\left[1-\varepsilon^2\right]^{\frac{3}{2}}\left(\frac{c}{L}\right)^2 \tag{22}$$

with $\varepsilon = \dfrac{r}{c}$ as the dimensionless orbit radius. The normalization removes the effects of orbit radius (r), oil viscosity (μ), and frequency (ω), helping to decipher the nature of the dynamic pressure.

Figure 17 shows dimensionless peak-peak pressures at the mid-plane (z=0), half-plane (z=0.25L), and end grooves (z=0.5L) for tests with circular orbits of growing amplitude (r/c=0.05-0.40). Lines in the figure indicate the measurement trends at each respective axial plane. The mid-plane dimensionless pressures (P^*) are nearly constant versus frequency, having a similar magnitude for different orbit radii. Close examination of the half-plane and end groove measurements shows a slight increase of P^* over the frequency range. The increase indicates that the local film pressures indeed show some fluid inertial effect (i.e. $P{\sim}\omega^2$).

In Figure 17, the viscous contribution of the pressure could be estimated as the pressure at ω=0. Interestingly, the pressure in the end groove tends towards ~0.1 (a negligible amount when compared to the half- and mid-plane pressure) as $\omega{\rightarrow}0$, indicating that the grooves provide dynamic pressure that is almost purely inertial in nature. In fact, the end groove pressure doubles over the course of the frequency range (10-250 Hz) due to fluid inertia effects.

---

[8] Other choices for normalization are also available. The current one obeys simplicity.
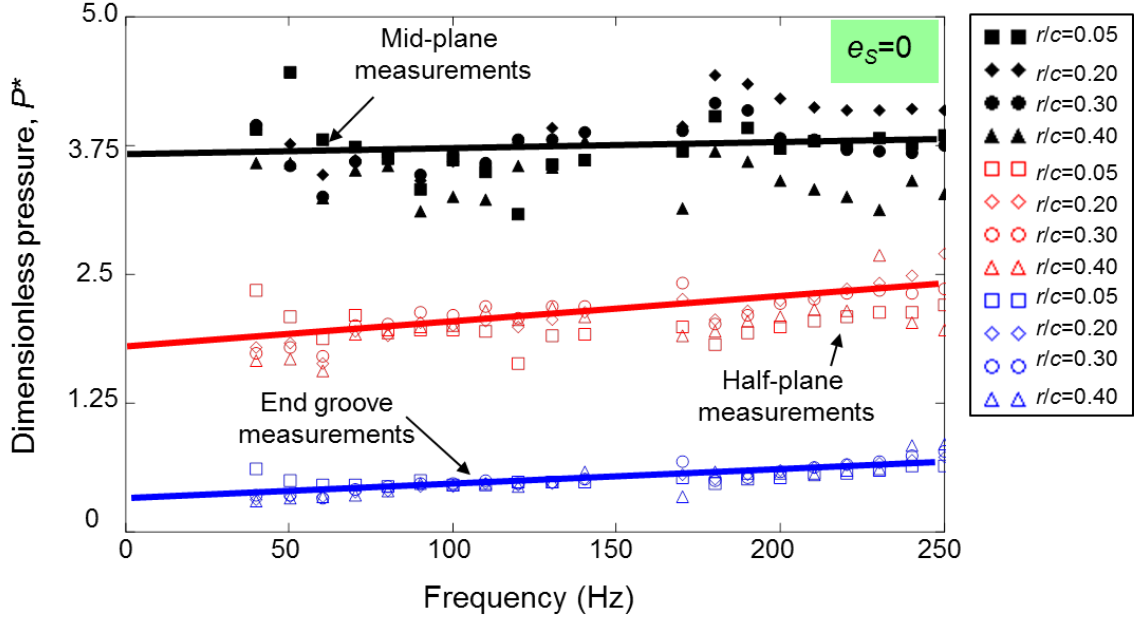
Figure 17. Dimensionless peak-peak pressure (P^*) versus excitation frequency for centered (e_S=0) test conditions (r/c=0.05-0.40). Lines represent trends of measured data

Evidence of Oil Film Cavitation

For measurements with a centered circular orbit at a whirl frequency of ω=100 Hz and increasing orbit amplitudes (r/c) = 0.05 to 0.060, Figure 18 shows the periodic variation of the film land dynamic pressure (at z=0) and the film thickness. The figure reproduces test data for three periods of whirl motion (T_P=2π/ω=0.01 s) from sensor P_4 (Θ=225°). In the figure, the dashed line denotes the radial clearance c=129.5 μm. The film thickness is generated from

$$h_{(\Theta,t)} = c + X_{(t)} \cos \Theta + Y_{(t)} \sin \Theta \qquad (23)$$

with
$$X_{(t)} = r_X \cos(\phi_X + \omega t)$$
$$Y_{(t)} = r_Y \cos(\phi_Y + \omega t) \qquad (24)$$

where r_x, r_y are the magnitudes, and ϕ_x, ϕ_y the arguments of the fundamental component of the Fourier series built functions from the measured displacements along the X, Y axes.
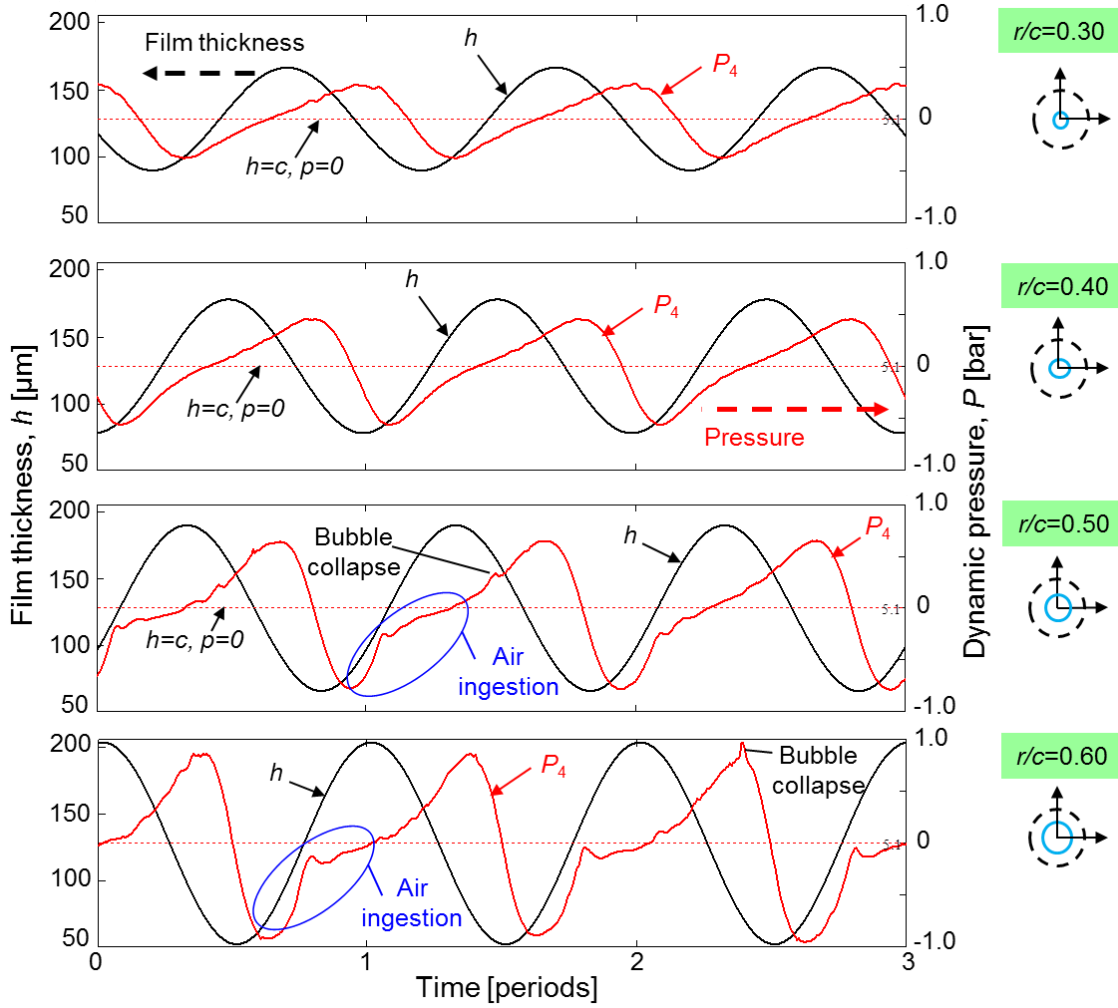
Figure 18. Dynamic film pressures (P) and film thickness (h) versus time (t/T) for measurements at the damper mid-plane (z=0). Circular centered orbit (e_S=0) at frequency ω=100 Hz. Graphs show orbits of magnitude, r/c=0.30 − 0.60 at Θ=225°

The dynamic pressures increase with an increase in orbit amplitude and are periodic in nature. For small orbit radii, $r/c < 0.4$, the pressures follow the BC velocity, i.e,

39

$p \sim -\partial h / \partial t$, having a null value when h=maximum and with a peak value just a few instants after the maximum squeeze velocity $-\partial h / \partial t \big|_{max} = r\omega$ occurs.

However, for whirl orbits with amplitudes $r \geq 0.5c$, the pressure waves show signs of randomness between periods, do not evolve monotonically (increase or decrease), and begin to make a *flat* pressure zone around the region of largest film thickness. The (high frequency) distortions, most peculiar for the test with r/c=0.6, are a persistent phenomenon likely due to air ingestion. The phenomenon is common in SFDs operating with ends open to ambient.

Diaz and San Andrés [23] introduce a feed-squeeze flow parameter (γ) that relates the lubricant supply flow rate to the dynamic change in volume in the squeeze film gap by

$$\gamma = \frac{Q_{in}}{\pi D L r \omega} \tag{25}$$

where r is the orbit radius and Q_{in}=5.03 LPM is the total flow rate supplied to the damper. If $\gamma>1$, the flow rate is sufficient to fill the volume change and no air ingestion will occur. On the other hand, if $\gamma < 1$ air ingestion will occur [23].

With the current SFD, $\gamma <1$ at $r/c\sim0.1$ and ω=100 Hz, and lessens as the amplitude (r) or the whirl frequency (ω) increases. Although air ingestion may occur at r/c=0.20, the dynamic pressure profile recorded at the **mid-plane** (Figure 18 above) does not show significant signs of ingestion until r=0.5c, at which the feed-squeeze parameter is $\gamma\sim0.20$. The ingested air creates the *flat* pressure zone as the film at that location is void of lubricant. As lubricant fills the annular gap again, pressure rises and air becomes entrapped in the lubricant forming air pockets or bubbles. The bubbles collapse randomly causing large spikes in pressure.

In addition to being prone to air ingestion, the test damper shows signs of lubricant vapor cavitation, occurring when the film absolute pressure drops to the lubricant saturation pressure ($P_{sat}=\sim0$ bar absolute). Figure 19 shows the measured pressure profile for a certain test case that produces large dynamic film pressures (r=0.60c, e_S=0,

ω=200 Hz). Vapor cavitation is identified as a flat area in the pressure profile at pressures approximately equal to zero absolute pressure (0 bar absolute). As pressure at this location (P_1) begins to rise, large vapor pockets collapse showing spikes in the pressure profile. The gas pocket or bubble collapsing is random from period to period and overpowers the effects of air ingestion shown previously. Prior literature, such as Refs. [22, 23], discusses in detail the characteristics and effects of air ingestion and lubricant vapor cavitation in SFDs operating with axial ends open to ambient. Note the characteristics of vapor cavitation shown here are evident in all tests with absolute pressures that drop to P_{sat}=~0 bar absolute. The film static pressure at Θ=30° away from a feed hole is P_{static}=1.3 bar absolute as measured by sensor E_1 (Θ=30°). Note the static pressure of the film is ~2.0 bar absolute at the feed-hole locations and significantly decreases circumferentially between hole locations, as shown in Appendix A.

Figure 19. Absolute film pressure and film thickness versus time (t/T) showing characteristics of vapor cavitation and gas bubble collapse. Circular centered orbit with orbit amplitude r/c=0.60 at frequency ω=200 Hz. Pressure measurement at mid-plane, P_1 (Θ=315°, z=0). P_{static}=1.3 bar absolute.

The characteristics shown above provide a way to identify the SFD operating regime (with or without oil cavitation) at any test condition. Analysis of the experimental pressures measured can be used to create a "map" of the degree of oil cavitation (gaseous or vapor) at any operating condition. Figure 20 and Figure 21 show the degree of gaseous cavitation and vapor cavitation, respectively, for tests with whirl frequency

(a) ω=100 Hz, (b) ω=220 Hz, and any combination of orbit amplitude (r/c) and static eccentricity (e_S/c). The severity of cavitation ranges from 0-3 with 0 indicating no oil cavitation and 3 indicating oil cavitation across the entire axial length of the film land. Note, the cavitation maps are based purely on experimental film land pressure measurements at the various axial locations. The occurrence of lubricant cavitation likely varies circumferentially due to higher film land static pressure near the feed-holes.
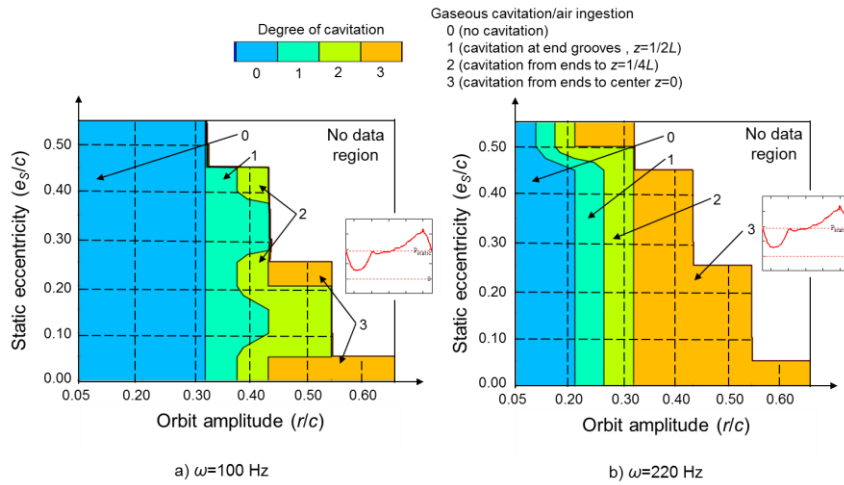
Figure 20. <u>Lubricant gaseous cavitation/air ingestion</u> maps for tests with whirl frequency (a) 100 Hz and (b) 220 Hz. P_{in}=2.63 bar absolute, 3 feed-holes 120 degrees apart
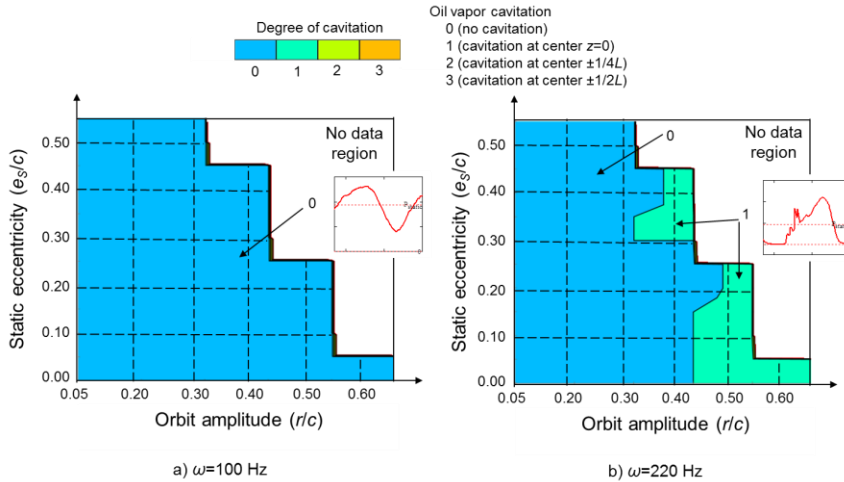
Figure 21. <u>Lubricant vapor cavitation</u> maps for tests with whirl frequency (a) 100 Hz and (b) 220 Hz. P_{in}=2.63 bar absolute, 3 feed-holes 120 degrees apart

CHAPTER VI

EXPERIMENTAL FORCE COEFFICIENTS

This section presents the squeeze film damping and added mass coefficients obtained for the test SFD (c=0.127 mm, D=127 mm, L/D=0.2). Circular orbit tests conducted on the dry structure provide estimations of the un-lubricated (dry) system stiffness, damping, and mass coefficients ($\mathbf{K}$, $\mathbf{C}$, $\mathbf{M}$)$_S$. Circular and elliptical orbit tests with ISO VG 2 oil flowing to the damper film land yield the lubricated system coefficients ($\mathbf{K}$, $\mathbf{C}$, $\mathbf{M}$). The SFD force coefficients are obtained by subtracting the dry system coefficients from the lubricated system coefficients, i.e.[9],

$$(\mathbf{K},\mathbf{C},\mathbf{M})_{SFD} = (\mathbf{K},\mathbf{C},\mathbf{M}) - (\mathbf{K},\mathbf{C},\mathbf{M})_S \qquad (26)$$

Chapter IV details the measurement and parameter identification procedure, and the operating conditions. Table 4 states the BC whirl amplitude (r), static eccentricity (e_S), and orbit type for all tests conducted. Table 5 lists the identified test rig structural (i.e. dry) stiffness, damping, and mass coefficients, along with the natural frequencies and damping ratios (ξ). The structural parameters presented in the table are identified from a circular centered orbit (CCO) test with r/c=0.1. The structural stiffness is similar to that identified from static load tests (see Appendix A). There is a small amount of damping and "remnant" mass in the structural system. The damping ratio (ξ) is ~0.02 which is typical of steel structures and the test system natural frequencies are ~150 Hz. Note the direct coefficients are similar along both X and Y directions, whereas the cross-coupled coefficients are almost nil. Hence, the test results demonstrate the test rig is nearly isotropic.

---

[9] Equation (26) assumes the mechanical system is linear

Table 4. BC whirl amplitude (r), static eccentricity (e_S), and orbit type for SFD tests

Test Variables		Type of orbit
Whirl radius (-)	**Static eccentricity (-)**	
r/c = 0.05, 0.2, 0.3, 0.4, 0.5, 0.6	$e_S/c = 0.0$	Circular Orbits
r/c = 0.05, 0.2, 0.3, 0.5	$e_S/c = 0.1$	
r/c = 0.05, 0.2, 0.3, 0.4, 0.5	$e_S/c = 0.2$	
r/c = 0.05, 0.2, 0.3, 0.4	$e_S/c = 0.3$	
r/c = 0.05, 0.2, 0.3, 0.4	$e_S/c = 0.4$	
r/c = 0.05, 0.2, 0.3	$e_S/c = 0.5$	
Major Axis: r/c = 0.1, 0.35, 0.6	$e_S/c = 0.0$	Elliptical Orbits (2:1, 5:1)
Major Axis: r/c = 0.1, 0.35, 0.6	$e_S/c = 0.1$	
Major Axis: r/c = 0.1, 0.35, 0.6	$e_S/c = 0.2$	

Table 5. SFD test rig structural (dry) coefficients

Structural Parameter identified from circular orbit test with r/c=0.1			Direct Coefficients		Cross Coupled	
			XX	**YY**	**XY**	**YX**
Stiffness	K_S	[MN/m]	13.9	13.0	0.0	0.0
	U_{KS}		±0.6	±0.6	±0.1	±0.1
Damping	C_S	[kN-s/m]	0.6	0.5	0.1	0.2
	U_{CS}		±0.1	±0.1	±0.1	±0.1
Mass	M_S	[kg]	3.4	2.4	0.7	0.2
	U_{MS}		±0.3	±0.2	±0.2	±0.2
BC Mass	M_{BC}	[kg]	15.2	15.2	-	-
	U_{MBC}		±0.05	±0.05	-	-
Natural frequency	ω_n	[Hz]	153	147	-	-
	$U_{\omega n}$		±3.5	±3.5	-	-
Damping ratio	ξ	[-]	0.02	0.02	-	-
	U_ζ		±0.005	±0.003	-	-

*Uncertainty for each parameter calculated using procedure outlined in Appendix C.

44

Measured SFD Force Coefficients (Circular Orbits)

Force coefficients for the lubricated configuration are identified from circular orbit tests over a frequency range of 10-250 Hz. Recall, circular and elliptical loads, via the *X* and *Y* shakers, create orbital motion by applying sinusoidal forces that are 90° out of phase. Circular orbits have constant amplitude (*r*), while elliptical orbits have differing amplitudes ($r_X \neq r_Y$) along the *X*, *Y* directions. Note, the natural frequency of the <u>lubricated</u> test rig is $\omega_n \sim 130$ Hz, which is lower than the dry test rig natural frequency (~150 Hz) due to the added mass of the SFD.

Figure 22 presents typical measured single frequency whirl orbits for circular orbit tests. The orbits represent (a) a centered (e_S=0) BC condition, and (b) an offset (e_S/c=0.2) BC condition with orbit amplitude *r*/*c*=0.5.
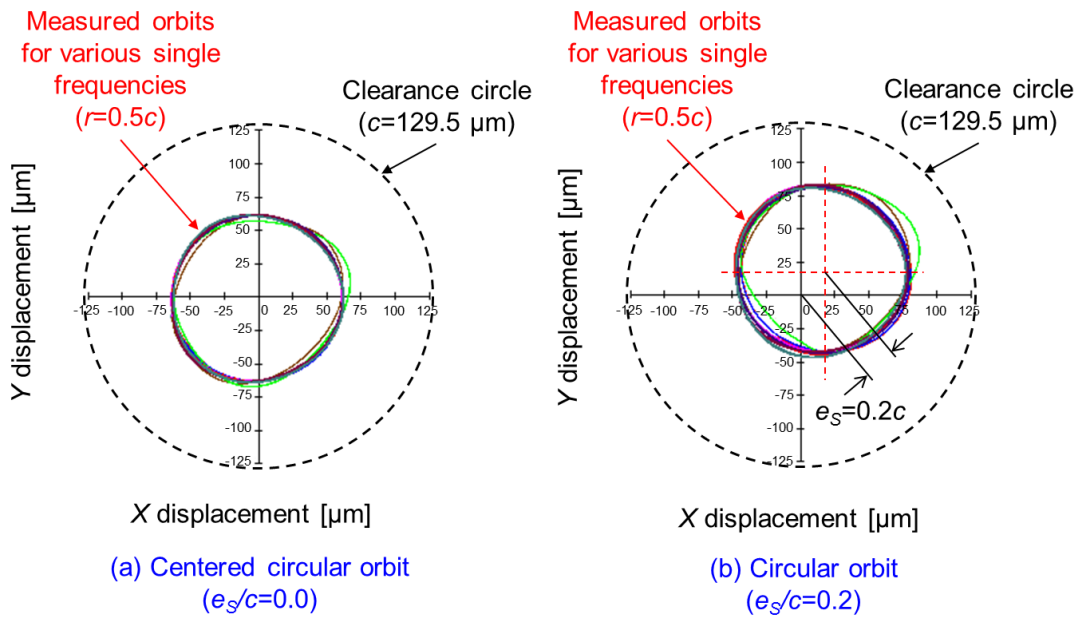
Figure 22. Measured circular orbits for several single frequency tests (ω=10-250 Hz). (a) Centered (e_S/c=0) test and (b) offset (e_S/c =0.2) test with *r/c* = 0.5

In general, for all operating conditions, the test SFD does not show stiffness coefficients (K_{SFD}~0). The test SFD cross-coupled mass coefficients (M_{XY}, M_{YX}) are at

least one order of magnitude lesser than the direct coefficients and thus considered negligible. Cross-coupled damping coefficients (C_{XY}, C_{YX}) are important at large static eccentricity ratios ($e_S/c>0.4$) for a small orbit amplitude ($r=0.05c$) only. Note the damping and mass coefficients are non-dimensionalized as $\overline{C} = C/C^*$ and $\overline{M} = M/M^*$, respectively, with C^* and M^*, for this damper geometry and lubricant, equal to

$$C^* = 12\pi \frac{\mu R^3 L}{c^3} \left[1 - \frac{\tanh\left(L/D\right)}{\left(L/D\right)} \right] = 3.70 \frac{\text{kN} \cdot \text{s}}{\text{m}} \tag{27}$$

and

$$M^* = \pi \frac{\rho R^3 L}{c} \left[1 - \frac{\tanh\left(L/D\right)}{\left(L/D\right)} \right] = 1.65 \text{ kg} \tag{28}$$

For tests with a centered journal ($e_S=0$), Figures 23 and 24 depict the SFD direct damping and added mass (inertia) coefficients versus orbit amplitude (r/c), respectively. The largest orbit amplitude amounts to nearly 60% of the film clearance. In the figure, the bars denote the uncertainty for the noted parameter ($U_C=8.4\%$, $U_M=11.6\%$ max). The damping coefficients ($\overline{C}_{XX} \sim \overline{C}_{YY}$)$_{\text{SFD}}$ increase little with an increase in orbit amplitude. The added masses ($\overline{M}_{XX} \sim \overline{M}_{YY}$)$_{\text{SFD}}$ appear to decrease linearly with an increase in orbit amplitude. At small orbit radius ($r \ll c$), $\overline{M}_{XX} \sim \overline{M}_{YY}$ is ~27% of the BC actual mass ($M_{BC}=33.4$ lb). The results, as expected, show that fluid inertia effects are more important for small amplitude motions rather than for motions with large amplitudes.

Appendix C presents the procedure for calculation of uncertainty in force coefficients. In general each SFD direct damping coefficients have a total uncertainty U_C <8.4% and SFD direct inertia coefficients have a total uncertainty U_M <11.6% at small orbit amplitudes. Note the force coefficients and uncertainties are valid exclusively for the identification frequency range noted ($\omega=10$-250 Hz).

46
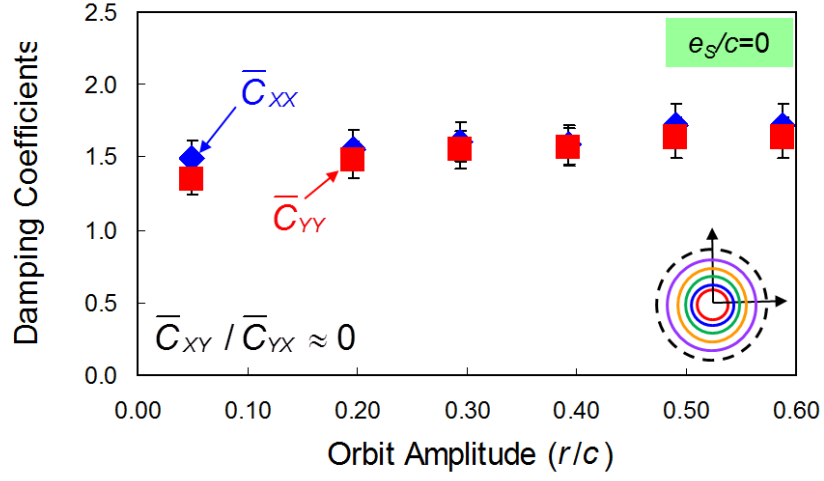
Figure 23. SFD direct damping coefficients ($\overline{C}_{XX}$, $\overline{C}_{YY}$) versus orbit amplitude. Static eccentricity e_S=0. Open ends SFD with c=129.5μm
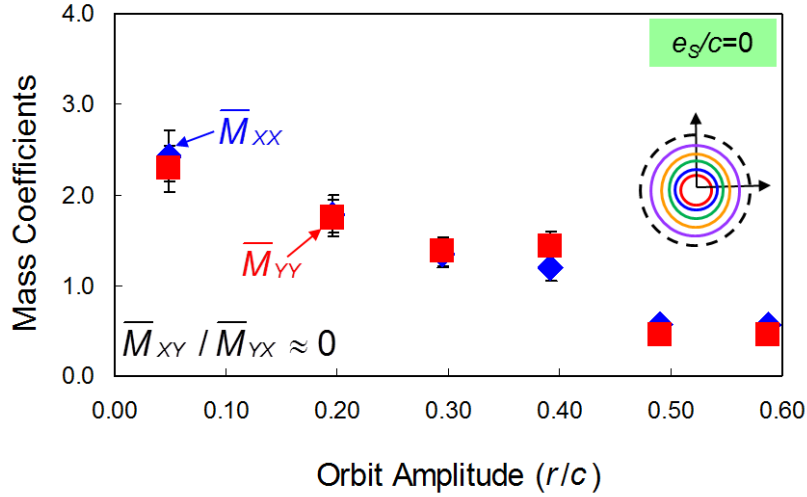
Figure 24. SFD direct added mass coefficients ($\overline{M}_{XX}$, $\overline{M}_{YY}$) versus orbit amplitude. Static eccentricity e_S=0. Open ends SFD with c=129.5μm

For tests with a small amplitude whirl orbit (r/c~0.05), Figure 25 and Figure 26 show the SFD damping and added mass coefficients versus static eccentricity (e_S/c), respectively. The damping coefficients ($\overline{C}_{XX}$ ~ $\overline{C}_{YY}$)$_{SFD}$ increase with static eccentricity,

nearly doubling at $(e_S/c)=0.50$. The mass coefficients $(\overline{M}_{XX} \sim \overline{M}_{YY})_{SFD}$ are relatively constant, i.e., not sensitive to the static eccentricity.
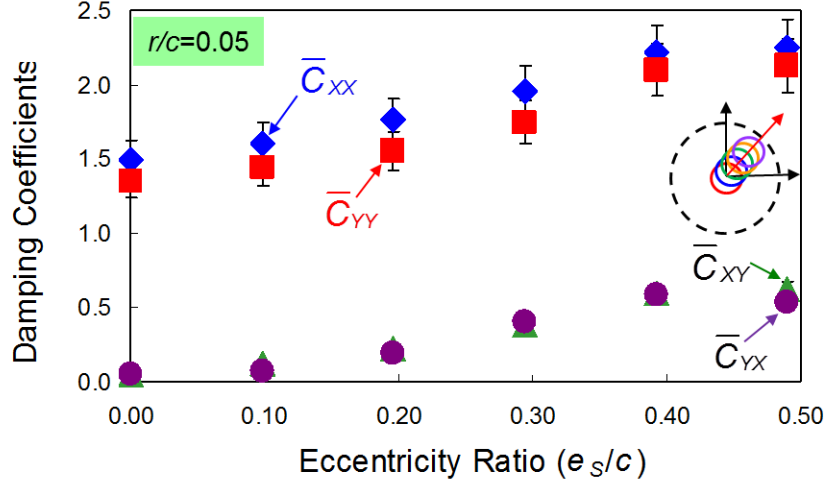
Figure 25. SFD direct damping coefficients ($\overline{C}_{XX}$, $\overline{C}_{YY}$) versus static eccentricity (e_S/c). Small amplitude orbit with $r=0.05c$. Open ends SFD with $c=129.5\mu m$
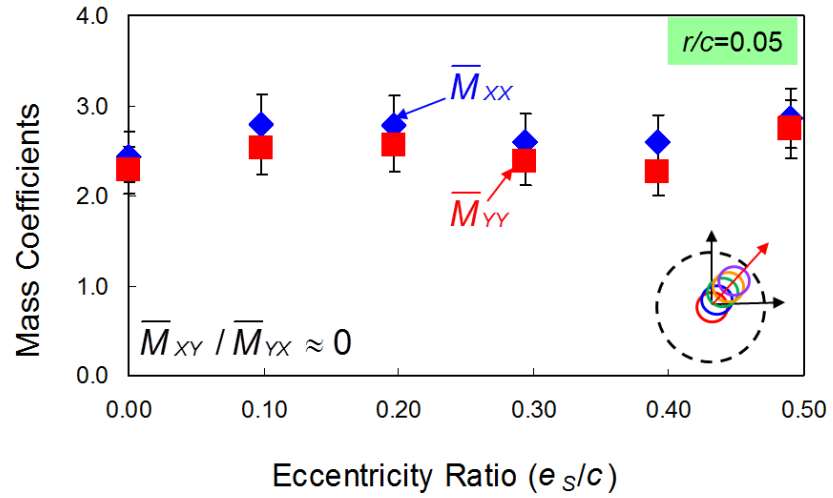
Figure 26. SFD added mass coefficients ($\overline{M}_{XX}$, $\overline{M}_{YY}$) versus static eccentricity (e_S/c). Small amplitude orbit with $r=0.05c$. Open ends SFD with $c=129.5\mu m$

Figure 25 (above) also shows the increase of cross-coupled damping coefficients ($\overline{C}_{XY}, \overline{C}_{YX}$) with static eccentricity (e_S/c). Cross-coupled damping ($\overline{C}_{XX}, \overline{C}_{YY}$) is negligible at small static eccentricity ratios but becomes significant for $e_S \geq 0.2c$. In fact, the cross-coupled damping is as large as 25% of the direct damping at static eccentricities that are 40% and 50% of the damper clearance. On the other hand, the cross-coupled damping coefficients are negligible at all other orbit radii tested ($r=0.2-0.6c$) for all static eccentricities ($e_S=0-0.50c$).

Industry commonly refers to SFDs as having a stiffness (K_{SFD}); however, as found in this research and numerous other research efforts, SFDs do not produce stiffness coefficients. In actuality the stiffness referred to by industry is a "dynamic stiffness", that is $K_{DYN}=\omega C_{XY}$. The maximum cross-coupled damping measured is $C_{XY}\sim 0.62C^*$ at ($e_S/c=0.5$, $r/c=0.05$). For this test condition over the identification frequency range ($\omega=10-250$ Hz), the dynamic stiffness ranges from $K_{DYN}=0.14-3.57$MN/m. Recall, the test rig structural stiffness is $K_S=13.5$MN/m. Therefore, the test damper shows a considerable dynamic stiffness ($\left| \dfrac{K_{DYN}}{K_S} \right| > 0.1$) at small orbit amplitudes ($r=0.05c$), large static eccentricities ($e_S \geq 0.4c$), and high frequencies ($\omega>100$ Hz), only.

Figure 27 and Figure 28 show surface plots of the identified damping, and inertia coefficients, respectively, versus orbit amplitude (r/c) and static eccentricity (e_S/c). Notice, the trends presented in Figure 23 thru Figure 26 are consistent for all combinations of orbit amplitude and static eccentricity. For brevity only the direct X-axis coefficients are shown; typically $\overline{C}_{XX} \sim \overline{C}_{YY}$ and $\overline{M}_{XX} \sim \overline{M}_{YY}$.

Recall, the analytical damping (C^*) and mass (M^*) coefficients are valid for small amplitude motions ($r/c<0.25$). The experimental coefficients show, for small orbit radii ($r/c=0.05$ and $r/c=0.20$) at a centered condition ($e_S=0$), to be ~1.4 times greater than the analytical damping coefficient and ~2.3 times greater than the analytical mass

coefficient[10]. At large orbit amplitudes and statically eccentric positions the difference between the experimental damping coefficient the analytical damping coefficient is even greater. Note, the end grooves are not accounted for in the analytical mass coefficient, thus reasoning for the much higher experimental coefficients.
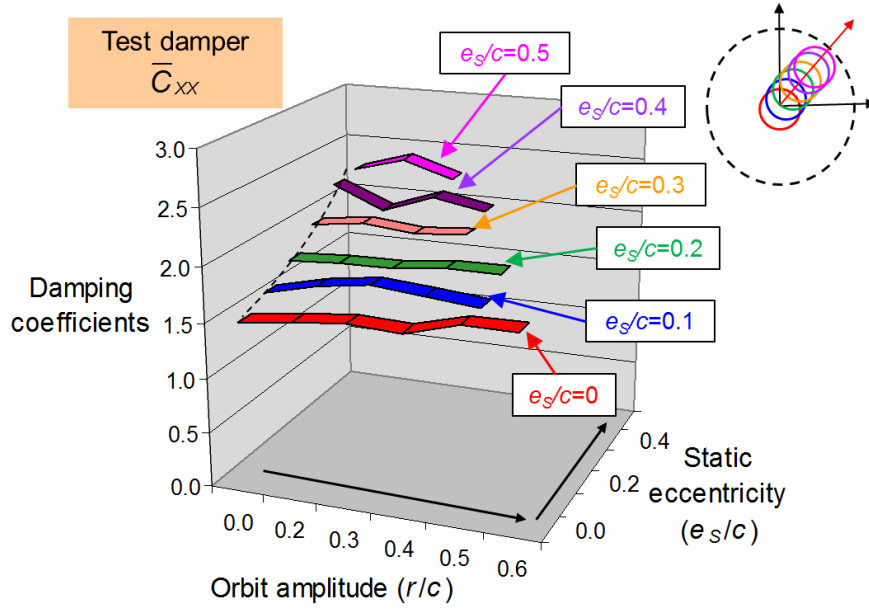
Figure 27. SFD direct damping coefficients ($\overline{C}_{XX}$) versus static eccentricity (e_S/c) and orbit amplitude (r/c). Open ends SFD with c=129.5μm

---

[10] Calculation of the analytical damping coefficient with an L_{eff}=28.5 mm gives a $\overline{C}_{XX} \sim \overline{C}_{YY} \sim 1$ for orbit radii of r=0.05c and r=0.20c with static eccentricity e_S=0. L_{eff} is the total axial length of the damper that has clearance c (i.e. film land length (L) plus end lip length, excluding end groove length).
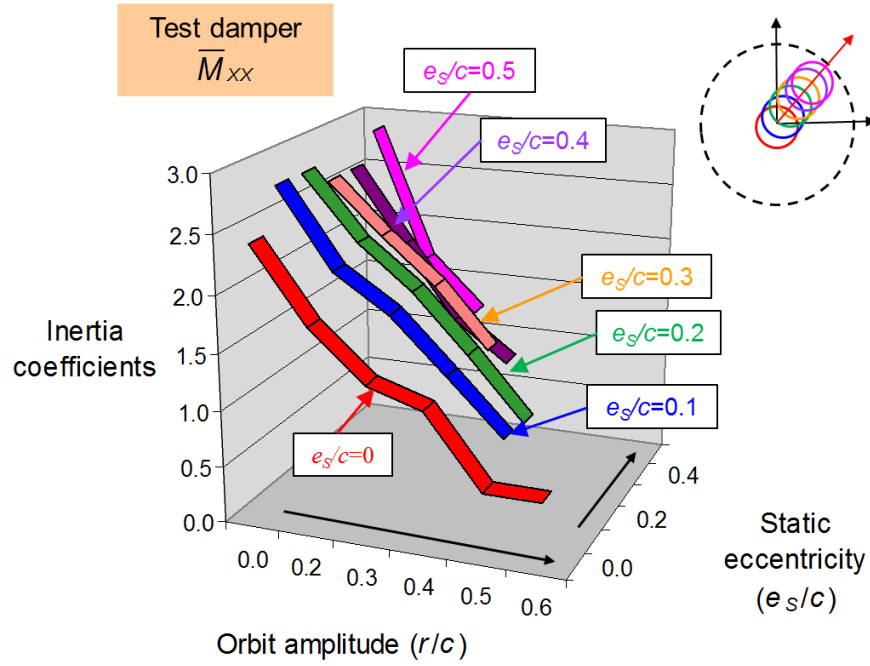
Figure 28. SFD direct inertia coefficients ($\overline{M}_{xx}$) versus static eccentricity (e_S/c) and orbit amplitude (r/c). Open ends SFD with c=129.5µm

Measured Force Coefficients (Elliptical Orbits)

More force coefficients for the test damper are identified from elliptical orbit tests over a frequency range of ω=10-250 Hz. Elliptical orbits have differing amplitudes ($r_X \neq r_Y$) along the X, Y directions. The damper was tested with whirl BC motions at two amplitude ratios (r_X:r_Y=2:1 and r_X:r_Y=5:1) and static eccentric conditions as outlined in Table 4 above. Note, the major axis for the elliptical orbit tests is along the X-axis. Figure 29 shows actual measured elliptical orbits for several single frequency tests at a centered condition (e_S=0).
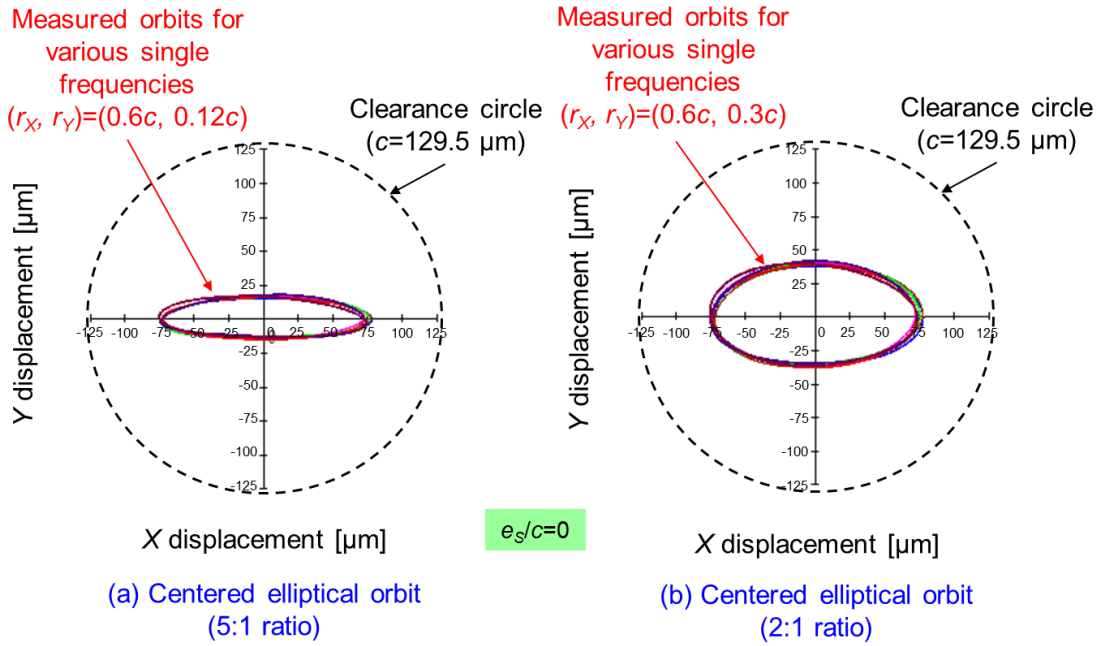
Figure 29. Measured (a) 5:1 elliptical orbits and (b) 2:1 elliptical orbits for several single frequency tests (ω=10-250 Hz). Centered orbit test with (r_X, r_Y) = (0.6, 0.12)c and (0.6, 0.3)c, respectively

In general, the identified force coefficients do not depend upon the whirl amplitude aspect ratio (r_X:r_Y). In other words $(\mathbf{K}, \mathbf{C}, \mathbf{M})_{2:1} \sim (\mathbf{K}, \mathbf{C}, \mathbf{M})_{5:1}$ for the tests conducted[11].

Figure 30 and Figure 31 present damping coefficients ($\overline{C}_{XX} \sim \overline{C}_{YY}$)$_{SFD}$ identified from circular and elliptical orbits. For the test orbit amplitude range (r=0.05c-0.60c) and static eccentricity range (e_S=0-0.50c), the coefficients identified from elliptical orbits are nearly identical to those identified from circular orbits with a similar orbit amplitude (r=r_X).

---

[11] Force coefficients from a whirl amplitude aspect ratio of 2:1 are not shown for brevity.
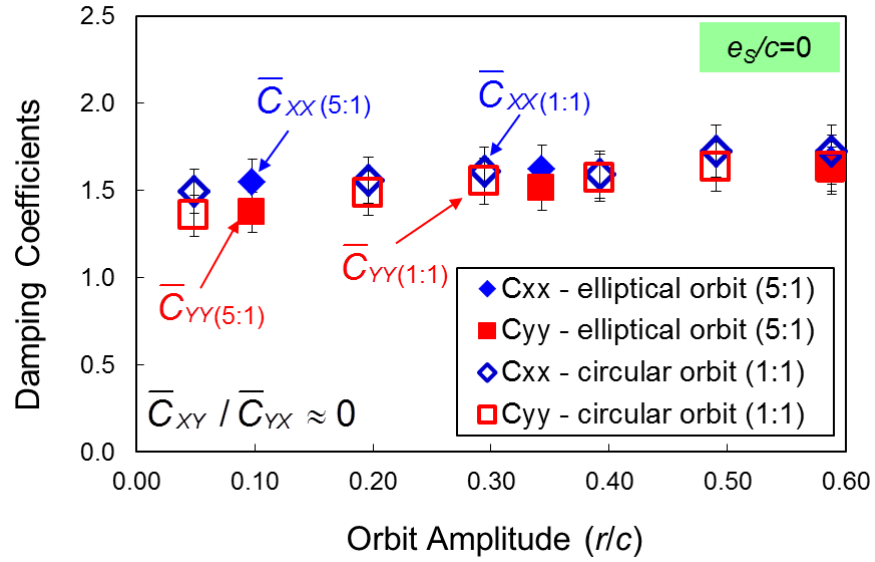
Figure 30. SFD direct damping coefficients ($\overline{C}_{XX}$, $\overline{C}_{YY}$) versus orbit amplitude (r/c). Parameters identified for centered (e_S=0) circular orbits (1:1) and elliptical (5:1) orbits
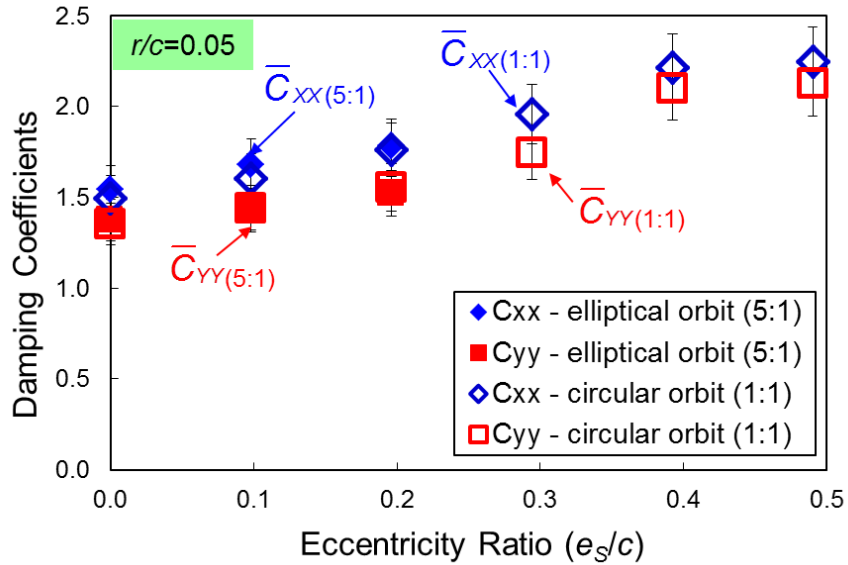
Figure 31. SFD direct damping coefficients ($\overline{C}_{XX}$, $\overline{C}_{YY}$) versus static eccentricity (e_S/c). Parameters identified for circular orbits (1:1) with r=0.05c and elliptical (5:1) with r_X=0.1c orbits

53

Figure 32 and Figure 33 depict the direct inertia coefficients $(\overline{M}_{XX} \sim \overline{M}_{YY})_{SFD}$ identified from circular and elliptical orbits. For elliptical orbits the identified mass coefficients decrease with an increase in the whirl amplitude. On the other hand, the mass coefficients are rather constant with an increase in static eccentricity. Over the static eccentricity range (e_S/c=0-0.2) and for small amplitude motion (r_X/c=0.05), the coefficients identified from elliptical orbits are nearly identical to coefficients identified from circular orbits with a similar orbit amplitude (r_X=r).
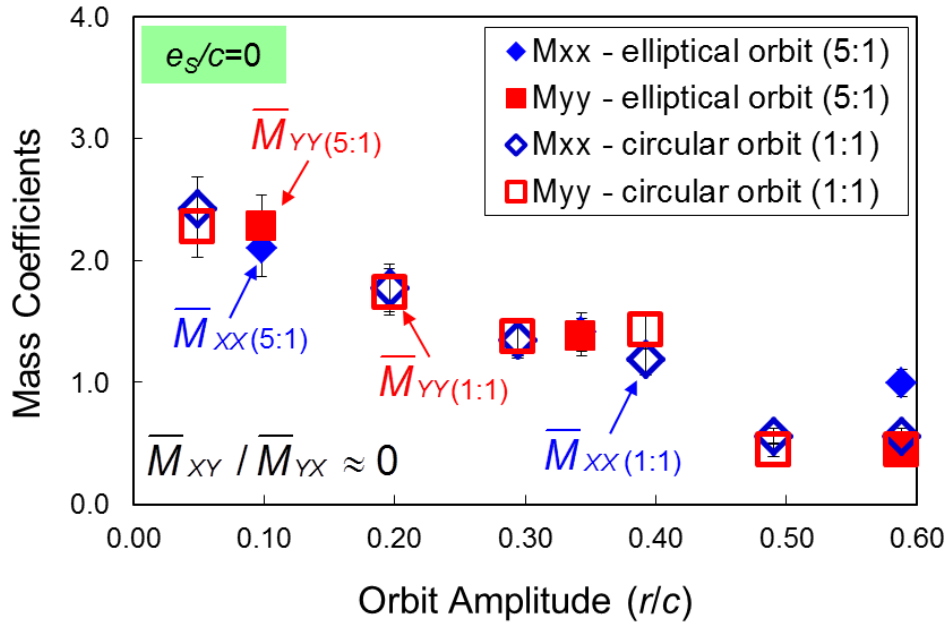
Figure 32. SFD direct inertia coefficients ($\overline{M}_{XX}$, $\overline{M}_{YY}$) versus orbit amplitude (r/c). Parameters identified for centered (e_S=0) circular orbits (1:1) and elliptical (5:1 ratio) orbits
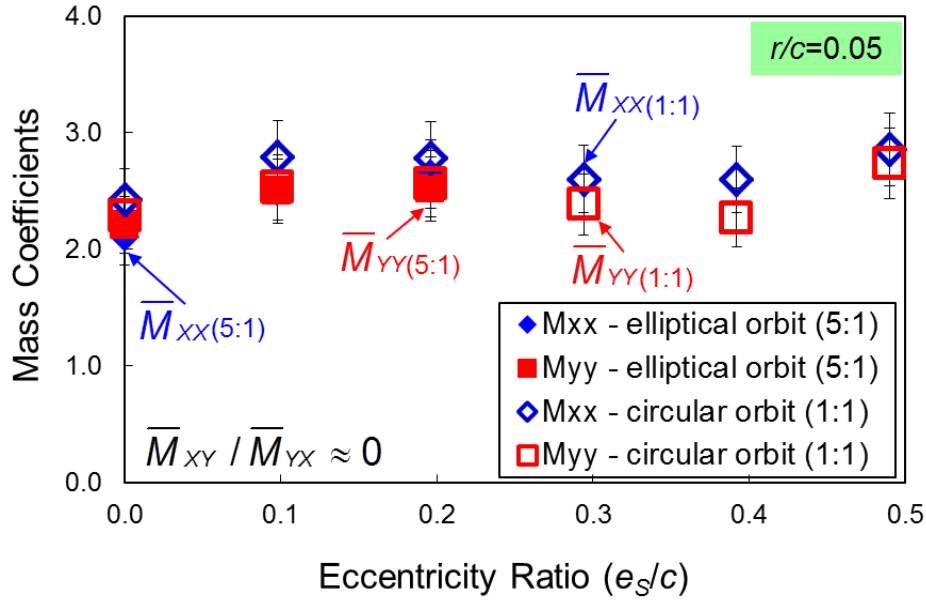
Figure 33. SFD direct inertia coefficients ($\overline{M}_{XX}$, $\overline{M}_{YY}$) versus static eccentricity (e_S/c). Parameters identified for circular orbits ($r=0.05c$) and elliptical ($r_X=0.1c$ - 5:1 ratio) orbits

The results of the elliptical orbit tests imply that the major amplitude of motion, in this case r_X, dictates the magnitude of the force coefficients. That is, the SFD force coefficients for an elliptical orbit with major amplitude r_X are the same as SFD force coefficients for a circular orbit with amplitude r. This finding is congruent with those in Refs. [42, 43].

Comparison of Force Coefficients with a Grooved SFD

Refs [42, 43] report force coefficients for damper configurations with a central groove by conducting numerous dynamic load tests. One of the damper configurations consists of two $L=12.7$ mm (0.5 inch) damper film lands separated by a deep central feeding groove. Figure 34 shows the grooved damper side by side with the aforementioned non-groove damper. For simplicity in this section the grooved damper will be referred to as test damper B and the non-groove damper as test damper C.
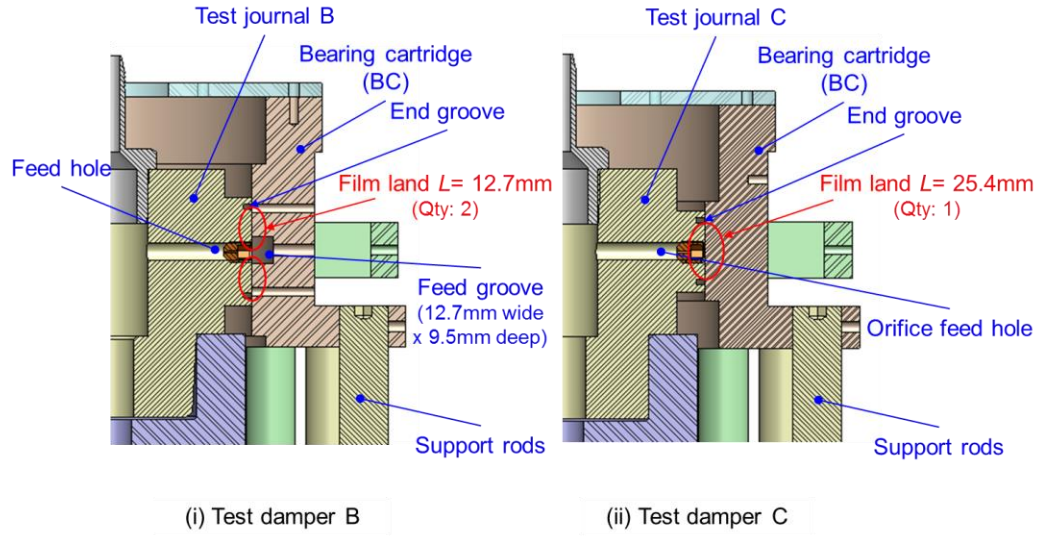
Figure 34. Cross-section views comparing two test damper configurations. (i) Test damper B, *L*=12.7mm, *D*=127mm, *c*=127µm (nominal), 12.7 x 9.65 mm feed groove (ii) Test damper C, *L*=25.4mm, *D*=127mm, *c*=127µm (nominal), no feed groove.

Table 6 shows the dimensions of test dampers B and C. Damper B has similar physical dimensions as damper C with the exception of its larger clearance, c_B=137.9µm (5.43 mil), and the 12.7mm wide x 9.5mm deep feed groove at its mid-plane. Note the total land length of each damper is 25.4mm (1 inch). In addition, both dampers contain similar end-grooves and end-lips for future installation of piston ring end seals.

Table 6. Critical dimensions and parameters of the grooved[42] and non-grooved test dampers

Damper Config.	Film land length, L (mm)	Journal Diameter, D (mm)	Radial clearance, c (µm)	Feed groove dimensions (mm)	Structure stiffness, K_S (MN/m)	BC mass, M_{BC} (kg)	Identification Frequency, ω (Hz)
Grooved (B)	12.7 (Qty: 2)	127	137.9	12.7 x 9.5	4.38	16.9	5-75
non-grooved (C)	25.4	127	129.5	None	13.45	15.2	10-250

The frequency range for parameter identification for test damper C is ω=10-250 Hz. Previous tests with test damper B (groove) were conducted for a frequency range of ω=5-75 Hz only. For comparisons between the two dampers (this section only), the identification range for damper C is limited to ω=10-80 Hz. Note that limiting the frequency range for identification, as shown in Table 7, decreases the damping coefficients by approximately 10% and increases the inertia coefficients by as much as 50%. This difference in force coefficients is due to the inherent nature of the identification curve fit to the measured mechanical impedance. When the frequency range for identification is small, the resulting mass coefficient in the curve fit $\mathrm{Re}(H) = K - M\omega^2$ is higher than the actual value. The damping coefficient in the curve fit $\mathrm{Im}(H) = C\omega$ is less sensitive to the width of the frequency range.

In addition to the frequency range being different, the structural stiffness for tests with damper B is about 1/3 the stiffness for test with damper C. Prior experimentation shows that the magnitude of the structural stiffness, representing a squirrel cage, has little to no effect on the damper forced performance [42].

Table 7. Example of identified system force coefficients from two different frequency ranges (test damper C)

Frequency Range	Orbit amplitude, r/c	Identified Direct Coefficients					
		Stiffness *K* [MN/m]		Mass *M* [kg]		Damping *C* [kN-s/m]	
		XX	*YY*	*XX*	*YY*	*XX*	*YY*
10-80 Hz	0.2	13.8	13.3	6.8	5.9	5.6	5.3
10-250 Hz	0.2	13.3	13.0	4.5	4.5	6.3	6.0
Difference (%)		3%	3%	51%	31%	-11%	-12%

Figure 35 and Figure 36 show the ratio of direct damping coefficients ($\dfrac{C_{(\text{damper C})}}{C_{(\text{damper B})}}$) and inertias ($\dfrac{M_{(\text{damper C})}}{M_{(\text{damper B})}}$), respectively, for centered circular orbit tests (e_S=0) with orbit radii r=0.05c-0.60c. The ratio of damping coefficients is ~1.1-1.3 for all orbit

amplitudes, indicating test damper C provides 10-30% more damping force than test damper B. However, recall that damper B and C have different clearances. Since the damping coefficient $C \sim \left(\dfrac{1}{c}\right)^3$, the ratio of clearances $\left(c_B \middle/ c_C\right)^3 = \left(5.43 \middle/ 5.10\right)^3 = 1.20$ shows that test damper C will produce 20% higher damping coefficients. The simple correlation demonstrates both dampers exhibit similar damping capability, that results mainly from the squeeze pressure in the film lands.

On the other hand, test damper B produces much higher inertia force coefficients, approximately 60% more, than test damper C. Note, simple theory shows $M \sim \left(\dfrac{1}{c}\right) \rightarrow \left(c_B \middle/ c_C\right) = \left(5.43 \middle/ 5.10\right) = 1.06$, indicating damper C should in fact have 6% greater inertia coefficients. The ratio of inertia coefficients (C/B) is <1 for the entire range of whirl orbit amplitudes. The large difference in inertia coefficients is due to the deep central feed groove of test damper B [4, 42, 43].
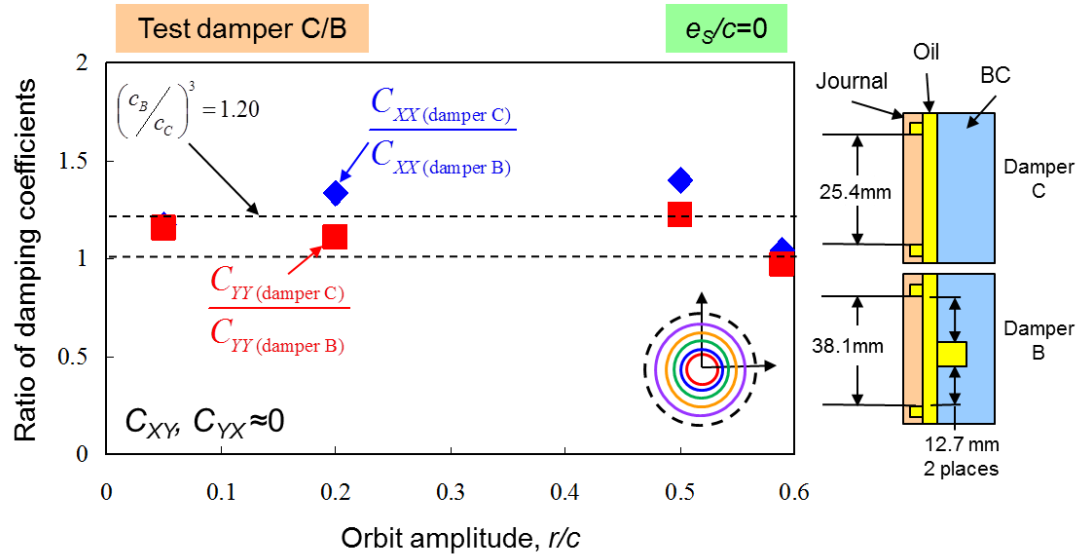
Figure 35. Ratio of direct damping coefficients, for dampers C and B versus orbit amplitude. Experimental data from centered (e_S=0) circular orbit tests with dampers B and C (open ends)
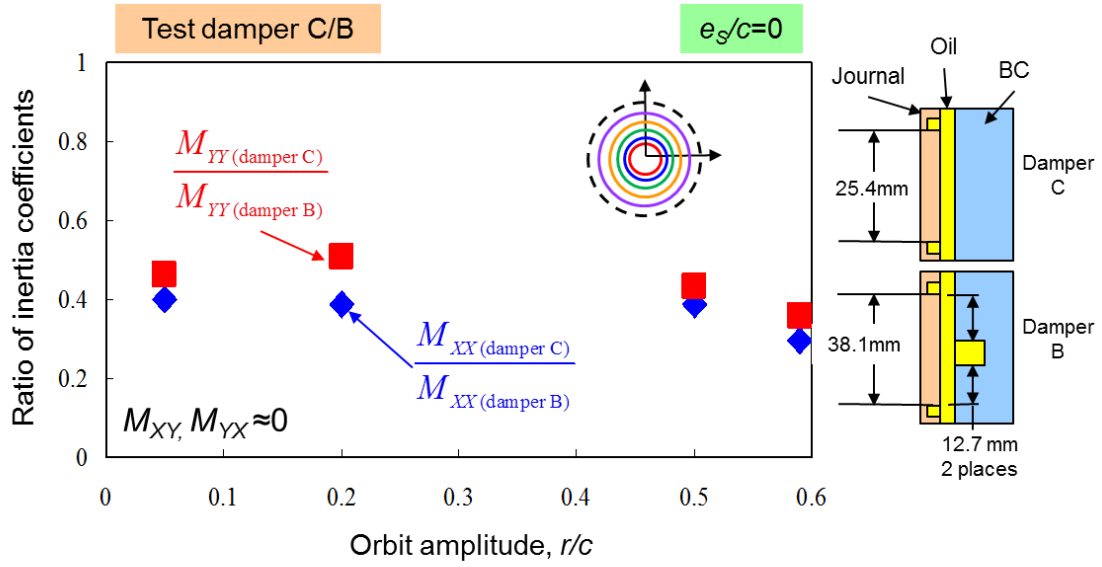
Figure 36. Ratio of direct inertia coefficient, SFD(C/B), versus orbit amplitude. Experimental data from centered (e_S=0) circular orbit tests with dampers B and C (open ends)

Figure 37 and Figure 38 show the ratio of direct damping coefficients ($\frac{C_{(damper\,C)}}{C_{(damper\,B)}}$) and direct inertia coefficients ($\frac{M_{(damper\,C)}}{M_{(damper\,B)}}$), respectively, for small amplitude orbit tests (r=0.05c) versus static eccentricity e=0.0-0.50c. The results show similar trends, $C_{(damper\,C)} > C_{(damper\,B)}$ and $M_{(damper\,C)} < M_{(damper\,B)}$, as in Figure 35 and Figure 36. The ratio of damping coefficients increases with an increase in static eccentricity (e_S), thus indicating damper C is more sensitive to the static eccentricity than test damper B.
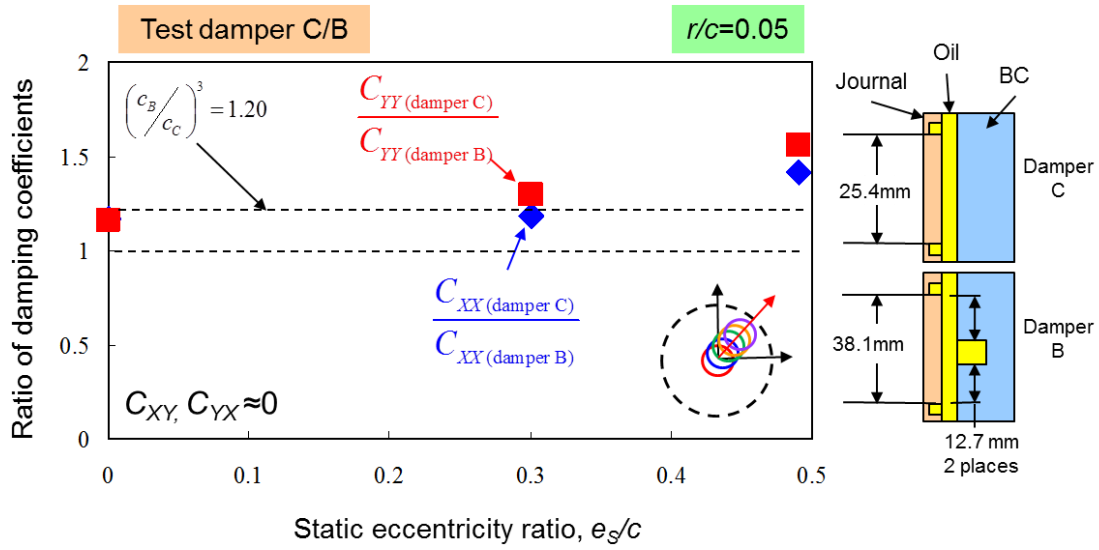
Figure 37. Ratio of direct damping coefficients, SFD(C/B), versus static eccentricity (e_S/c). Experimental data from small amplitude (r=0.05c) circular orbit tests with dampers B and C (open ends)
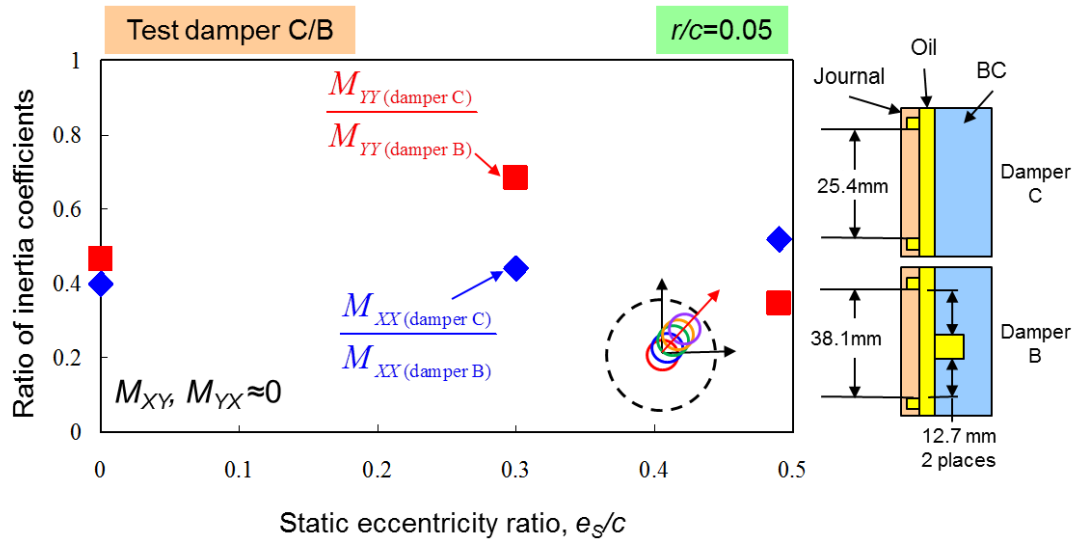
Figure 38. Ratio of direct inertia coefficients, SFD(C/B), versus static eccentricity (e_S/c). Experimental data from small amplitude (r=0.05c) circular orbit tests with dampers B and C (open ends)

In general, the comparisons of force coefficients for dampers B and C show that the deep central feed groove has little to no effect on the film damping coefficients (C_{SFD}) but significantly increases the damper inertia coefficients (M_{SFD}). Realize the configuration without a central groove is 12.7 mm (0.5 inch) shorter axially, which is desirable for saving space and weight. Also note that too large added inertia coefficients may affect system natural frequencies significantly.

One might question: why use a damper with a circumferential feed groove if it does not actually increase its damping? Recall from chapter V, vapor cavitation occurs when the dynamic film land pressure drops below the saturation pressure (P_{sat}~0 bar) of the oil. This can be prevented by raising the static pressure of the film land. Figure 39 and Figure 40 show representative (predicted) circumferential and axial static pressure profiles for the non-groove damper (C) and the grooved damper (B), respectively [44]. Both pressure profiles assume the same supply pressure from the feed holes.
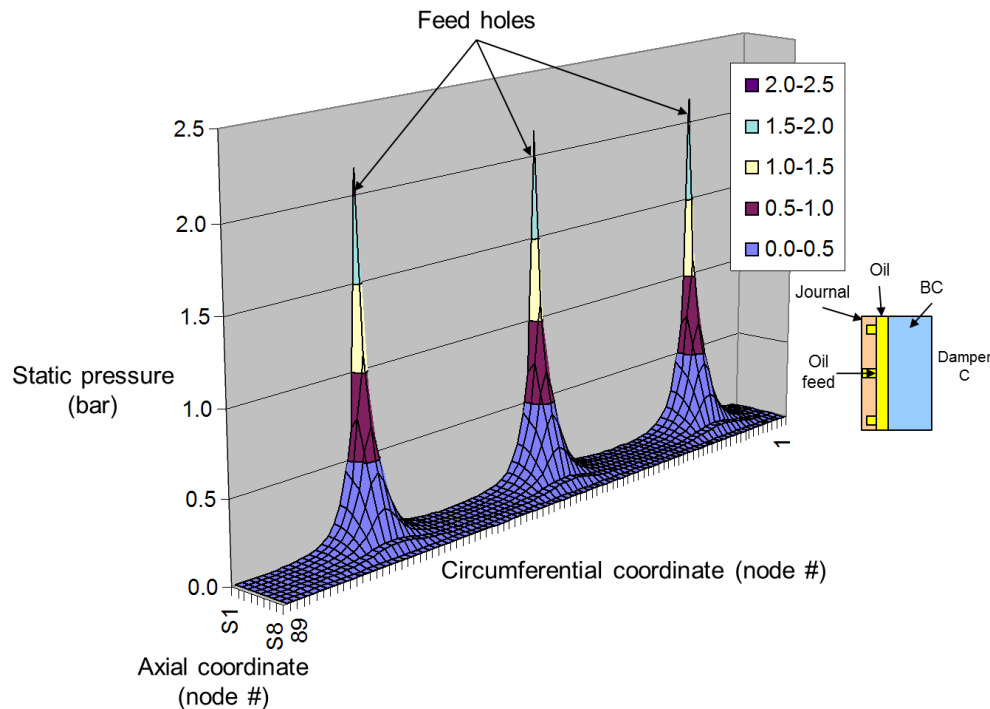
Figure 39. Static pressure profile of damper C as predicted by an in-house numerical program [44]

61
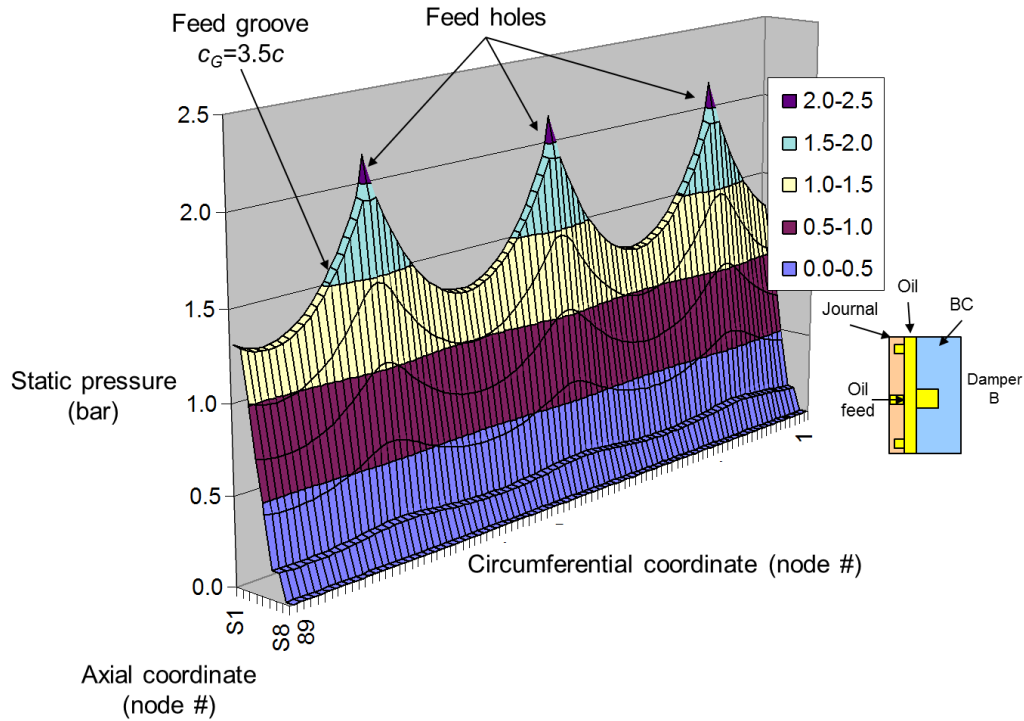
Figure 40. Static pressure profile of damper B as predicted by an in-house numerical program [44]

Between feed holes, damper C's film land static pressure is approximately ambient (~1 bar). The grooved damper (B) disperses the lubricant around the circumference of the damper better, which effectively maintains a higher static pressure between feed holes. Since the dynamic pressure oscillates about the static film land pressure damper B can operate at higher pressure regimes without lubricant vapor cavitation.

The choice between a grooved and non-groove dampers is a definite engineering trade-off. The operating conditions as well as the weight and space must all be taken into consideration. The film land static pressure of either damper can be raised and more evenly distributed by restricting the axial flow with the addition of end seals. This also aids to increase the damping capability and to reduce lubricant through flow rate. Experimental force coefficients and film land pressures for damper C with end seals is the focus of future investigation.

Force Coefficients with Variation in Number of Feed Holes

In addition to tests with the damper fed via three feed holes spaced 120° apart, experiments were also conducted with two and only one feed holes. The feed holes were plugged using an epoxy sealant and sanded smooth to match the contour of the journal surface, as shown in Figure 41. Figure 42 depicts top view schematics of the three variations in lubricant supply feed holes.
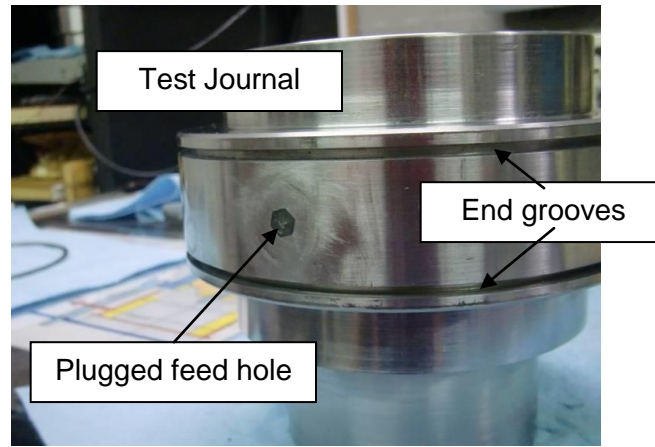
Figure 41. Picture of plugged feed-hole in test journal

a) 3 feed holes   b) 2 feed holes   c) 1 feed holes
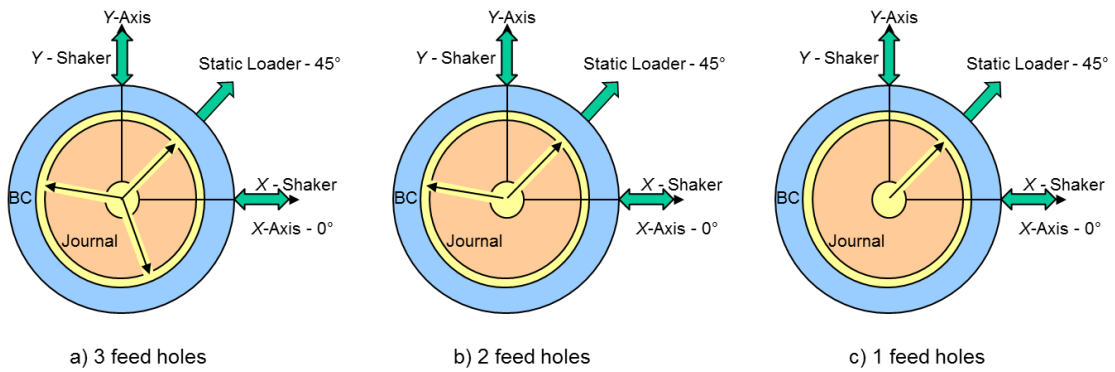
Figure 42. Variations of feed-hole supply configuration (a) 3 feed holes (b) 2 feed holes (c) 1 feed hole

For tests with a centered journal (e_S=0), Figure 43 and Figure 44 depict the dimensionless SFD direct damping and added mass (inertia) coefficients versus orbit

amplitude (*r/c*), respectively, for oil feed configurations with 1, 2, and 3 supply (open) holes. The frequency range of parameter identification is ω=10-250 Hz. The lubricant supply pressure upstream of the feed holes was maintained at P_{in}~1.62 bar. The lubricant flow rate as measured by the upstream turbine flow meter (Q_{in}) equals 5.0 LPM for operation with 3 holes and 2 holes[12], whereas Q_{in}=3.0 LPM for test with 1 open hole.
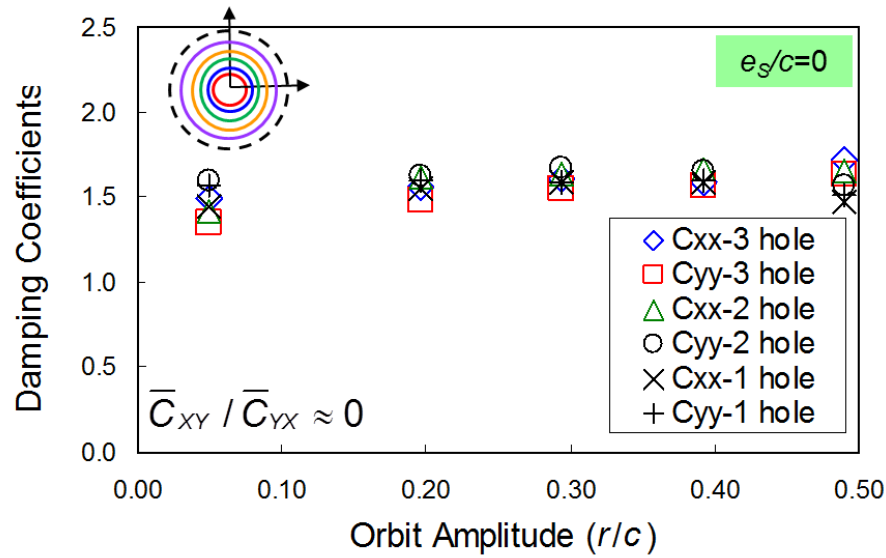
Figure 43. SFD direct damping coefficients ($\overline{C}_{XX}$, $\overline{C}_{YY}$) versus orbit amplitude. Static eccentricity e_S=0. Open ends SFD with c=129.5µm. Tests with 1, 2, and 3 active feed-holes shown

---

[12] Note, the flow rate (Qin=5 LPM) and the upstream pressure (Pin=1.62 bar) are the same for the tests with 3 and 2 holes. This implies that the pressure at the feed holes drops when testing with only 2 feed holes. Currently, sound reasoning on the drop in feed hole pressure is not available.
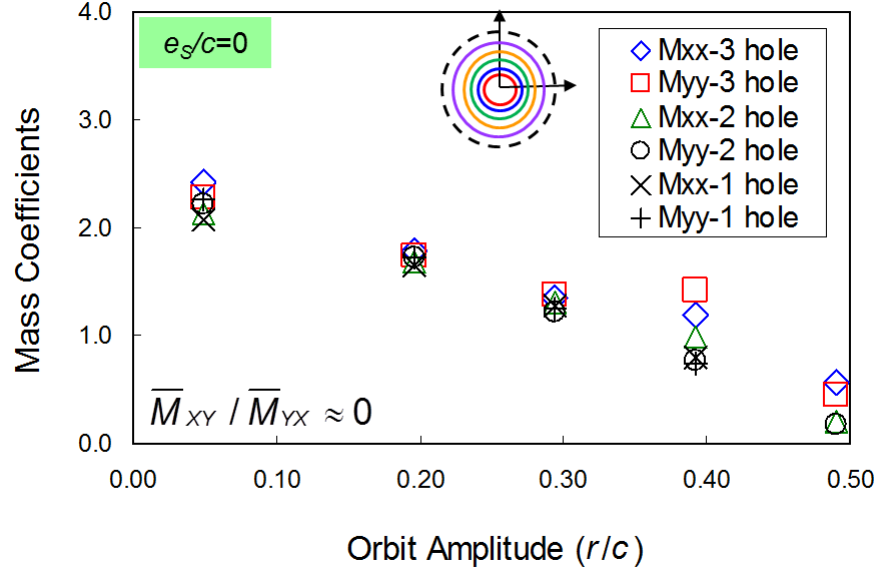
Figure 44. SFD direct added mass coefficients ($\overline{M}_{XX}$, $\overline{M}_{YY}$) versus orbit amplitude. Static eccentricity e_S=0. Open ends SFD with c=129.5µm. Tests with 1, 2, and 3 active feed-holes shown

The (centered) SFD damping coefficients obtained for the configurations with the different numbers of open feed holes are within 14% of each other (recall the uncertainty in damping coefficient U_C~8.4%). In general, the damping coefficient is not affected much by an increase in orbit amplitude. The SFD mass coefficients for the different numbers of feed holes are essentially the same up to an orbit amplitude of r/c=0.30. Above r/c=0.30, the mass coefficients are higher when more feed holes are used for lubricant supply. In general, the SFD force coefficients appear to be independent of the number of feed holes open supplying the damper film land, when operating in an centered condition (e_S=0).

Figure 45 and Figure 46 show representative static pressure profiles for the damper operating with one and two feed-holes, respectively. As discussed prior, the static pressure away from the feed-holes is approximately ambient, which make these areas of the damper more prone to oil vapor cavitation.
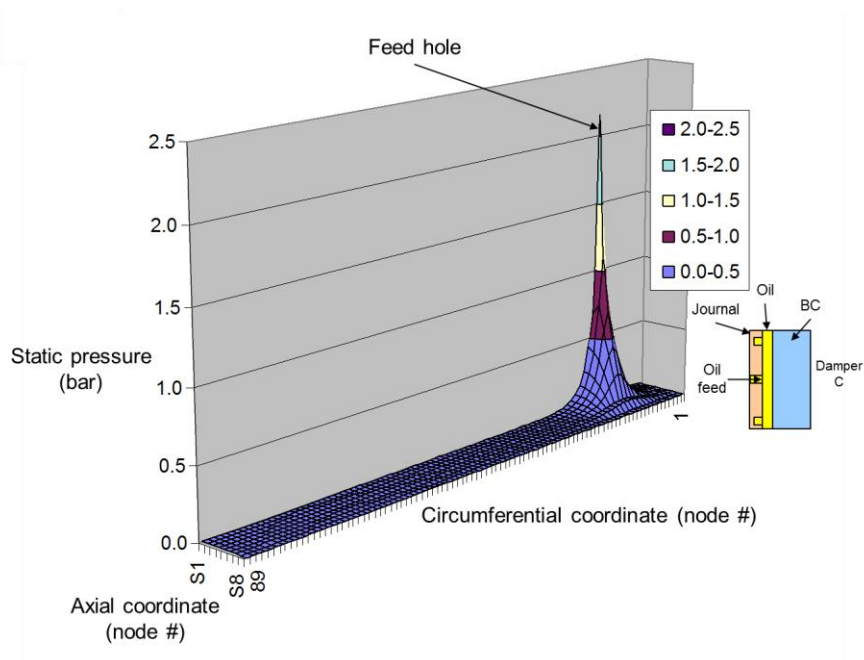
Figure 45. Static pressure profile of test damper with 1 feed hole as predicted by an in-house numerical program
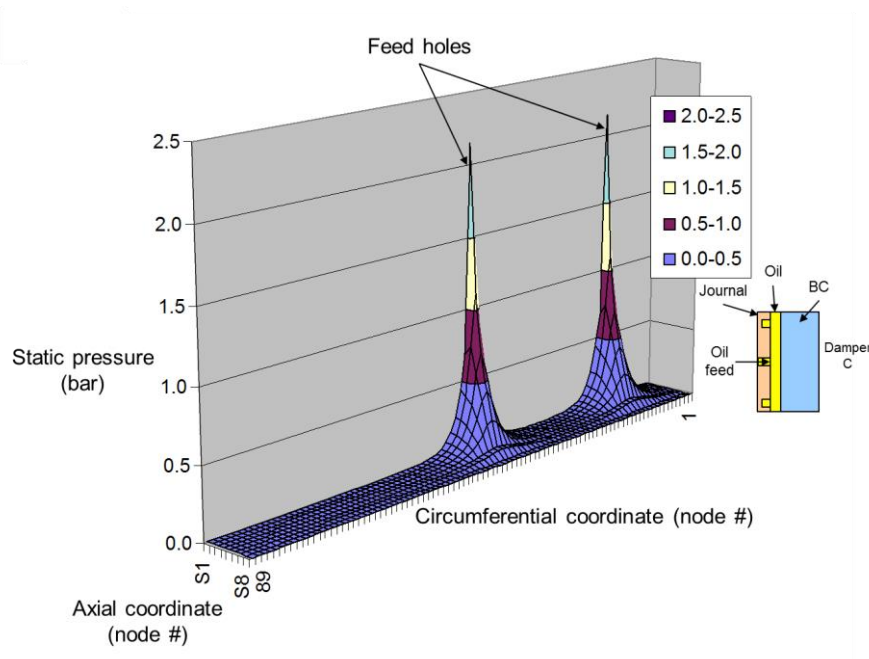
Figure 46. Static pressure profile of test damper with 2 feed holes as predicted by an in-house numerical program

66

Predicted Versus Experimental SFD Force Coefficients

The advanced computational physics code XL_SFD© [44] has proven to provide accurate predictions of SFDs force coefficients for configurations with a central feeding groove [42, 43]. The code, however, has yet to be benchmarked for configurations containing only orifice feed holes without a central feed groove, such as the current test damper. This section presents comparisons between experimental and predicted force coefficients for the test damper in operation with three feed-holes.

The computational model uses a finite element method to solve the modified Reynolds equation (including temporal fluid inertia effects) for various types of SFD configurations and journal whirl motions, centered and off-centered. Ref. [44] details on the physical model for the computational code. Table 8 gives the input parameters for predictions of the test damper. Figure 47 illustrates how the damper axial length and clearance are modeled in XL_SFD©. Note the end grooves and end lips are modeled in the computational program. The end groove depth is modeled with an effective clearance of $3.5c$, whereas the actual groove depth is $\sim 30c$. The effective clearance is determined from iteration to find the best fit between the predicted force coefficients and measured force coefficients (one case only). This type of estimation follows the process in Refs. [42, 43] for predictions of the effective depth of the central feed groove. Note, eight elements are used to model half the damper axial length and 90 elements are used to model the circumference of the damper.

Table 8. Input parameters for orbit analysis predictions of forced response of the test damper. Three feed holes at damper mid-plane (120° apart)

Parameter	Value	Units
Journal Diameter, D	127.15	mm
Nominal Axial Film Land Length, L	25.4	mm
Actual Total Damper Length	36.8	mm
End Groove Dim (width × depth)	2.54×30c	mm
Nominal Radial Clearance, c	129.54	μm
Ambient pressure at ends	0	bar
Supply pressure (holes)	1.62	bar
Cavitation pressure	-1.01	bar
Supply Temperature, T_S	22.2	°C
Viscosity	2.5	cP
Density	799.3	kg/m^3

a)

b)

Element #:	1	2	3	4	5	6	7	8
Length (mm)	2.54	2.54	2.54	2.54	2.54	2.54	1.52	1.59
Depth (*c)	1	1	1	1	1	3.5	1	10
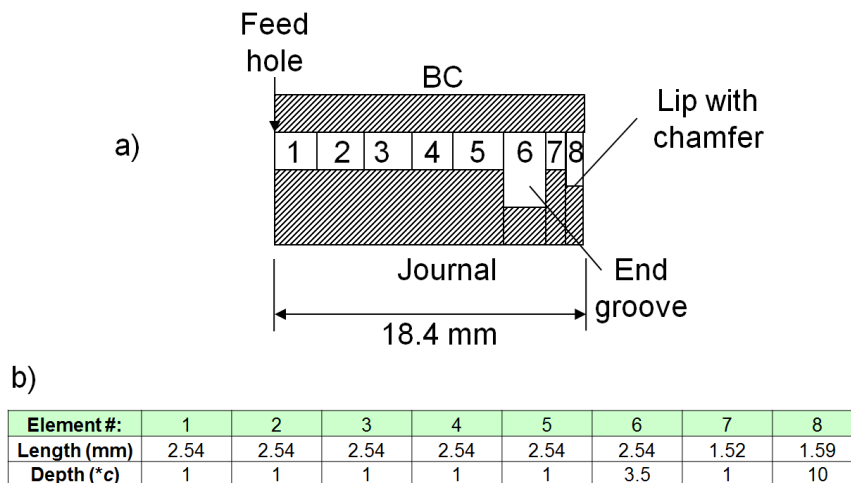
Figure 47. (a)Depiction of elements used to model half the damper axial length and (b) element input to computational program. Note the input end groove (element 8) clearance is ~3.5c (actual physical clearance ~30c)

The "orbit analysis" feature of the program is used for estimation of force coefficients. This feature requires inputs of orbit amplitude (r_X, r_Y) and static eccentricity (e_X, e_Y) along with frequency (ω) range for identification. The parameters (r, e_S, ω) as in the experimental tests are duplicated into computational program, which outputs predicted force coefficients. Using the inputs, the program performs a perturbation analysis, at all selected frequencies, to find the SFD forces versus time. Then the program transforms the forces into the frequency domain and performs a curve fit to the real and imaginary parts of the mechanical impedances (i.e. $\mathrm{Re}(\mathbf{H}) \rightarrow \mathbf{K} - \omega^2\mathbf{M}$; $\mathrm{Im}(\mathbf{H}) \rightarrow \mathbf{C}\omega$) to determine the linearized force coefficients. The orbit analysis procedure is a numerical replication of the actual experimental conditions.

As with the experimental results, over the same frequency range (10-250 Hz), the SFD predictions show negligible stiffness coefficients $K_{SFD}\sim0$, and negligible cross-coupled mass coefficients (M_{XY}, $M_{YX}\sim0$). Predicted cross-coupled damping coefficients (C_{XY}, C_{YX}) show similar trends as the experimental force coefficients.

For small to large amplitude whirl motions ($r=0.05c$-$0.60c$) about a centered condition ($e_S=0$), Figure 48 shows the predicted and experimental damping coefficients identified over the frequency range $\omega=10$-250 Hz. Figure 49 displays the predicted and experimental direct damping coefficients for the damper performing small amplitude motions ($r=0.05c$) at small ($e_S=0$) to moderate ($e_S=0.50c$) static eccentricities.
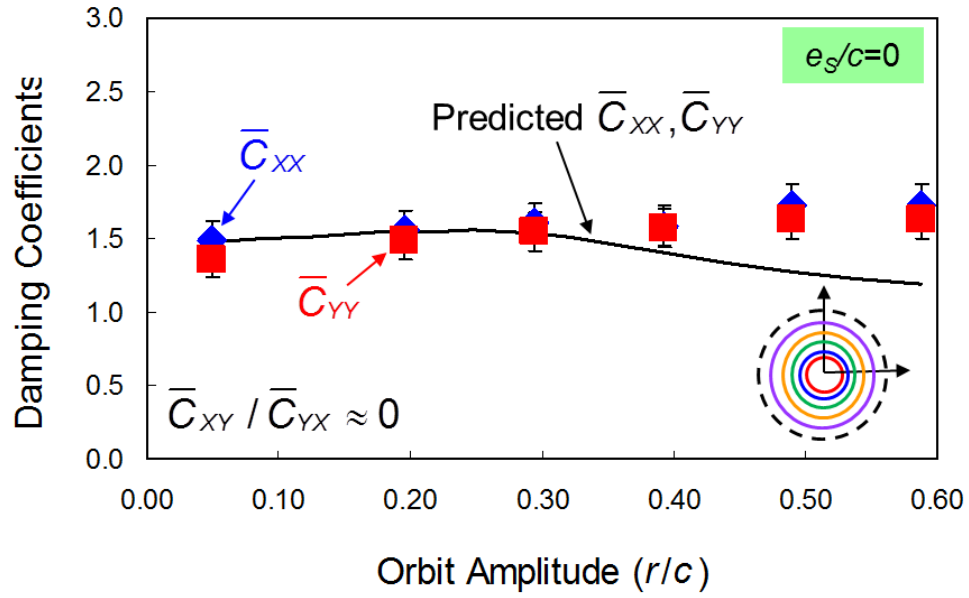
Figure 48. Experimental and predicted SFD direct damping coefficients
($\overline{C}_{XX}$, $\overline{C}_{YY}$) versus circular orbit amplitude (r/c). Static eccentricity e_S=0.
Open ends SFD with c=129.5μm
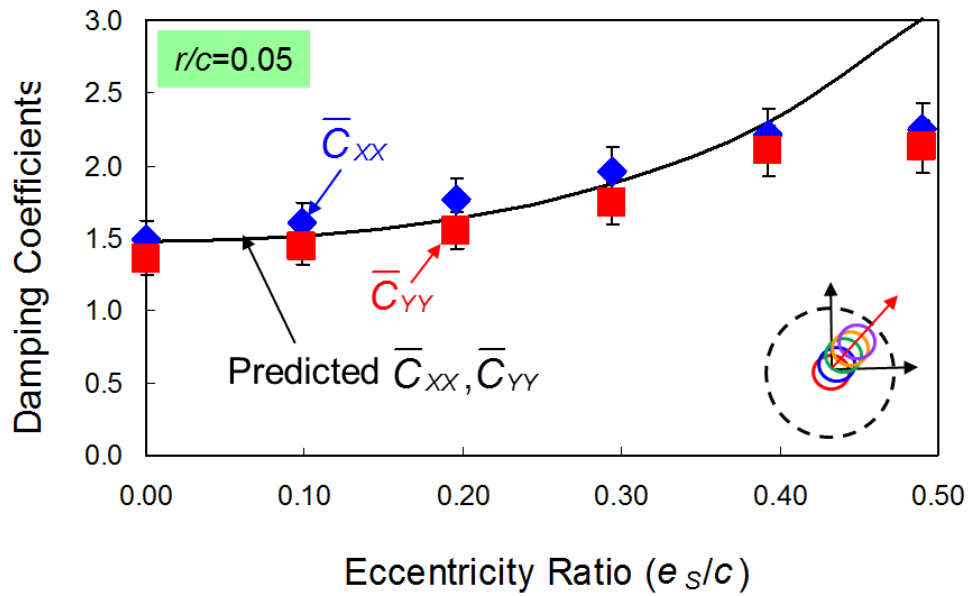
Figure 49. Experimental and predicted SFD direct damping coefficients
($\overline{C}_{XX}$, $\overline{C}_{YY}$) versus static eccentricity (e_S/c). Small amplitude orbit with
r/c=0.05. Open ends SFD with c=129.5μm

There is good correlation between the experimental and predicted damping coefficients ($\overline{C}_{XX}, \overline{C}_{YY}$) for orbit amplitudes r/c=0.05 to 0.30. Above r=0.30c, the predictions show a decrease in the damping coefficient, while the measured coefficients show a slight increase. The damping coefficients increase with static eccentricity, as the predictions also attest. The correlation with the test data is less compelling at the highest static eccentricities, $e/c \geq 0.40$. The test SFD damping coefficients shows less non-linearity with respect to the static eccentricity (e_S) than the predicted model results show.

For small to large amplitude whirl motions (r=0.05c-0.60c) about a centered condition (e_S=0), Figure 50 shows the predicted and experimental SFD inertia coefficients identified over the frequency range ω=10-250 Hz. Figure 51 displays inertia coefficients for the damper performing small amplitude motions (r=0.05c) at small to moderate static eccentricities (e_S=0-0.50c). The predictions for added mass (inertia) coefficients ($\overline{M}_{XX}, \overline{M}_{YY}$) agree well with the experimental coefficients at a small orbit radius, r/c=0.05 (see both Figures 50 and 51). However, with increased orbit amplitudes (Figure 50), the mass coefficients are well over predicted. The mass coefficients increase gradually with increased static eccentricity at r/c=0.05, as both the experimental and predicted values attest (Figure 51). However, for orbit amplitudes $r/c>$ 0.05 the inertia coefficients exhibit a slight increase and then decrease as static eccentricity increases, as shown in Figure 52. This trend is very different from that at small amplitudes of r/c=0.05.

Recall, that a majority of the fluid inertia effects comes from the end grooves, and that the groove depth is ~30c. The deep grooves likely give rise to recirculation regions with transitional or even turbulent flow at orbit amplitudes $r \geq 0.05c$. This type of flow regime leads to convective inertia effects that actually subtract from the temporal inertia effects [46], thus the reasoning for the drop in the experimental coefficients. The computational tool does not include modeling of the convective fluid inertia, which explains over prediction of the inertia coefficients at moderate to large amplitudes ($r \geq 0.05c$).
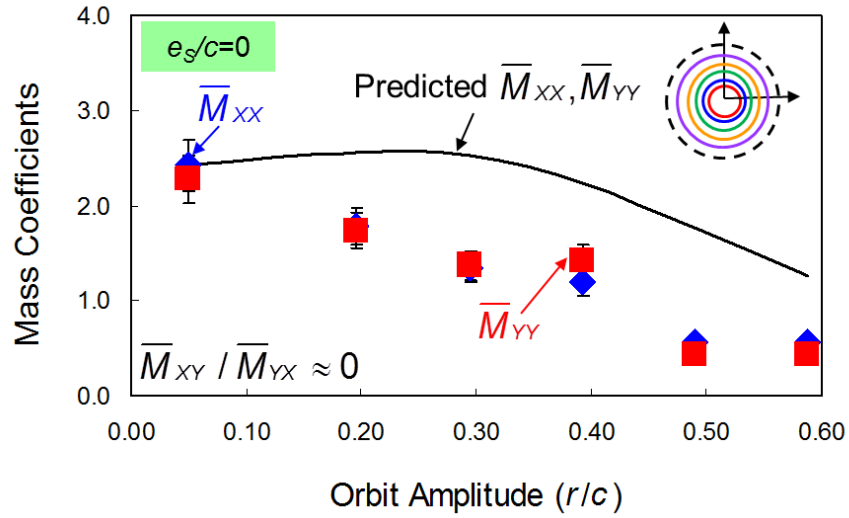
Figure 50. Experimental and predicted SFD direct added mass coefficients ($\overline{M}_{XX}$, $\overline{M}_{YY}$) versus orbit amplitude (*r/c*). Static eccentricity *e$_S$*=0. Open ends SFD with *c*=129.5µm
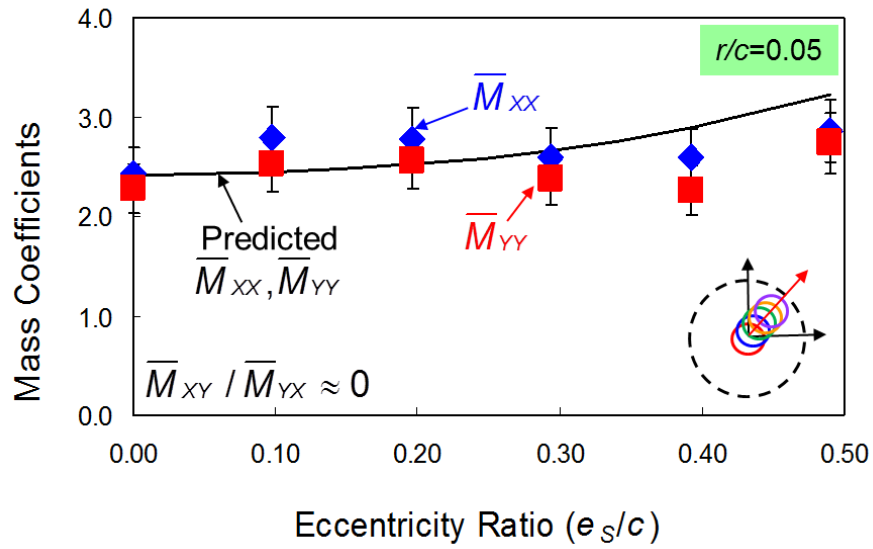
Figure 51. Experimental and predicted SFD added mass coefficients ($\overline{M}_{XX}$, $\overline{M}_{YY}$) versus static eccentricity (*e$_S$/c*). Small amplitude orbits with *r/c*=0.05. Open ends SFD with *c*=129.5µm

72
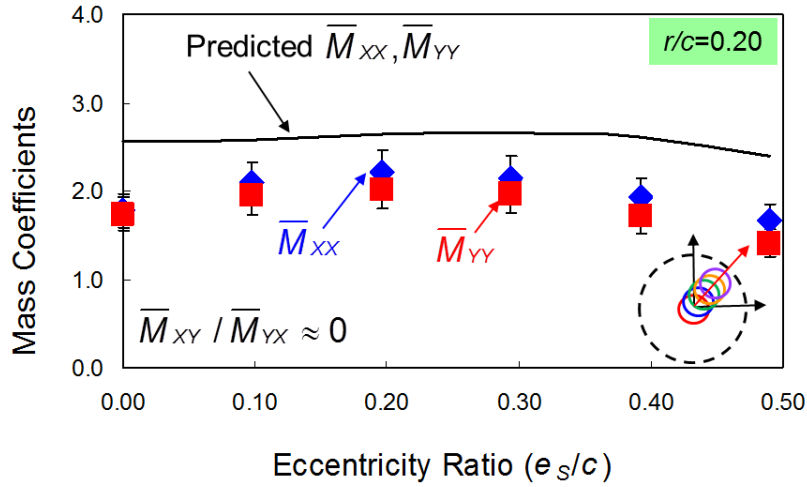
Figure 52. Experimental and predicted SFD added mass coefficients ($\overline{M}_{XX}$, $\overline{M}_{YY}$) versus static eccentricity (e_S/c). Circular orbit tests with *r/c*=0.20. Open ends SFD with *c*=129.5μm

As with the experimental coefficients, the predictions show that the damping coefficient is more sensitive to the static eccentricity (e_S) than to the orbit amplitude (r). On the other hand, the inertia force coefficients tend to be more sensitive to orbit radius than to static eccentricity for both predictions and experimental results.

The computational tool contains a model for oil vapor cavitation, however currently does not incorporate an air ingestion model. Although the analysis of the film land dynamic pressures (at ω=100 Hz) shows significant air ingestion at orbit amplitudes r>0.40c, sound observations about this effect on the force coefficients cannot be made from the current analysis. The force coefficients are identified from a model that curve fits to the measured impedances over a wide frequency range. Air ingestion and cavitation are shown to occur only at certain frequencies.

Validity of the Identified Linearized Force Coefficients

Presently, most rotordynamic predictive models use linearized force coefficients for modeling of bearings and seals; however, SFDs are inherently non-linear systems. The experimental force coefficients presented in this analysis assume the system is linear; nevertheless, the linearized force coefficients may still represent the actual SFD non-linear forces with some degree of accuracy. More importantly, the energy dissipated by the squeeze film damper must be considered.

The equation of motion for the bearing cartridge is

$$M_{BC} \begin{pmatrix} a_X \\ a_Y \end{pmatrix} = \begin{pmatrix} F_X \\ F_Y \end{pmatrix} - \begin{pmatrix} F_X \\ F_Y \end{pmatrix}_S - \begin{pmatrix} F_X \\ F_Y \end{pmatrix}_{SFD} \quad \text{or} \quad M_{BC}\, \mathbf{a} = \mathbf{F} - \mathbf{F_s} - \mathbf{F_{SFD}} \tag{29}$$

where M_{BC} is the mass of the BC and $\mathbf{a}=(a_X,a_Y)^T$ its acceleration of the BC. $\mathbf{F}=(F_X, F_Y)^T$ is the vector of external (periodic) loads exerted by the shakers, and $\mathbf{F_s}=(F_X, F_Y)_s^T$ is the reaction force from the support structure, and $\mathbf{F_{SFD}}=(F_X, F_Y)_{SFD}^T$ is the squeeze film damper force. Note that Eq. (29) does not account for any static load exerted on the BC by the hydraulic piston acting at 45° from the (X,Y) axes.

The reaction force from the system structure is assumed linear and modeled as

$$\mathbf{F_S} = \mathbf{M}_s \ddot{\mathbf{x}} + \mathbf{C}_s \dot{\mathbf{x}} + \mathbf{K}_s \mathbf{x} \tag{30}$$

where $\mathbf{x}=(x,y)^T$ and $(\mathbf{K_S}, \mathbf{C_S}, \mathbf{M_S})$ are matrices containing the support stiffness, remnant (dry) damping and virtual mass coefficients. These physical parameters are estimated earlier through independent experiments with the test system free of any lubricant; i.e., a dry condition. In general, $\mathbf{K_s} = \begin{pmatrix} K_{XX} & K_{XY} \\ K_{YX} & K_{YY} \end{pmatrix}_S$ for example. Note that the structure force $(\mathbf{F_s})$ relates to the kinematics of the BC motion **relative** to the journal, i.e., it uses the measured displacements (x,y). In addition, the identification procedure for the structural parameters consistently gives $K_{XX} \sim K_{YY} >> |K_{XY}|, |K_{YX}|$; $M_{XX} \sim M_{YY} < M_{BC}$, $M_{XY} = M_{YX} = 0$; and $C_{XX} \sim C_{YY} >> |C_{XY}|, |C_{YX}|$

Substituting Eq. (30) into the equation of motion Eq. (29) leads to the actual SFD reaction (possibly non-linear) as

74

$$\mathbf{F_{SFD}} = \mathbf{F} - M_{BC}\mathbf{a} - (\mathbf{M_s}\ddot{\mathbf{x}} + \mathbf{C_s}\dot{\mathbf{x}} + \mathbf{K_s}\mathbf{x}) \qquad (31)$$

Note that the preceding parameter identification procedure (see chapter IV) identifies the SFD force coefficients from tests spanning a range of whirl frequencies and models the SFD force as

$$\mathbf{F_{SFD}} \cong \mathbf{M_{SFD}}\ddot{\mathbf{x}} + \mathbf{C_{SFD}}\dot{\mathbf{x}} + \mathbf{K_{SFD}}\mathbf{x} \qquad (32)$$

where ($\mathbf{K_{SFD}}$, $\mathbf{C_{SFD}}$, $\mathbf{M_{SFD}}$) are the matrices of stiffness, damping and inertia force coefficients for the test SFD[13].

Figure 53 overlays the actual measured SFD reaction force orbit and the SFD force orbit as estimated with the linearized force coefficients, Eq. (32). Each graph represents a different test operating condition (r, e_S, ω).

---

[13] Note, the Fourier series of shaker load ($\mathbf{F}$), BC/journal relative displacement ($\mathbf{x}$), and BC acceleration ($\mathbf{a}$) are used for the calculations shown in equations (31) and (32). The number of Fourier coefficients used is 4 (i.e. 4 x freq), and the number of periods considered varies from 2-62 depending on the test frequency, ω.

a) $r = 0.2c$, $e_S = 0$, $\omega = 220$ Hz b) $r = 0.3c$, $e_S = 0.3c$, $\omega = 100$ Hz

c) $r = 0.5c$, $e_S = 0$, $\omega = 100$ Hz d) $r = 0.05c$, $e_S = 0.3c$, $\omega = 100$ Hz
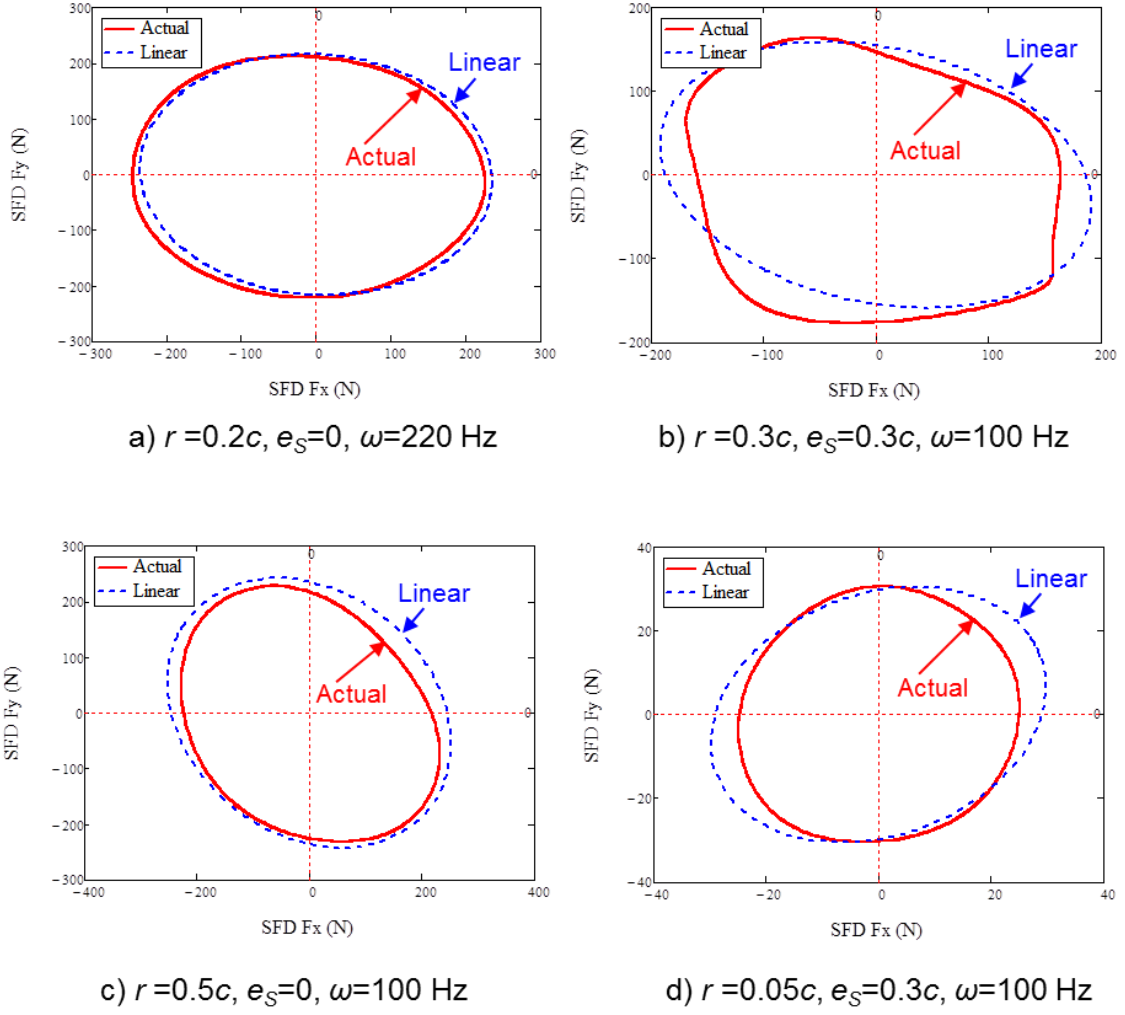
Figure 53. Comparison of actual SFD forces (F_Y vs. F_X) with the linear SFD forces as calculated with the estimated force coefficients. Note static offset removed

As seen in Figure 53, the SFD force built from the identified force coefficients can vary greatly from the actual SFD forces. However, forces can be conservative or dissipative in nature or both. In the case of SFDs, the dissipative forces are the key ingredient. The dissipated energy (E_v) over one period of motion for a circular orbit with amplitude r and frequency ω is [47]

$$E_v = \oint \left(F_X \dot{x} + F_Y \dot{y} \right) dt \tag{33}$$

76

The energy dissipated in a full period of motion can be calculated from both the actual SFD forces and the linearized SFD forces[14]. A simple percent difference calculation between the amount of energy dissipation gives a measure of how well the linearized force coefficients represent the actual system as [47]

$$E_{diff} = \frac{E_{actual} - E_{linear}}{E_{actual}} \cdot 100 \ \%$$ (34)

Figures 54, 55, and 56 show contour plots of the percent difference in the dissipated energy for tests at 40 Hz, 100 Hz, and 220 Hz, respectively. Recall, the identified force coefficients are applicable to only the range ω=10–250 Hz. The changing contour shades represent the differing precentage difference. The *X*-axis represents orbit radii (*r*), while the *Y*-axis represents static eccentricity for all experiments conducted. Recall, the max uncertainty in calculated force coefficients is U_C~8.4% and U_M~11.6%, which leads to a max uncertainty in the calculated force (F_{SFD}) of U_{FSFD}~13.8% and dissipated energy (E_v) of U_{Ev}~19.5%.

---

[14] Conservative forces give $\oint F \, dx = 0$ over a full period of motion.
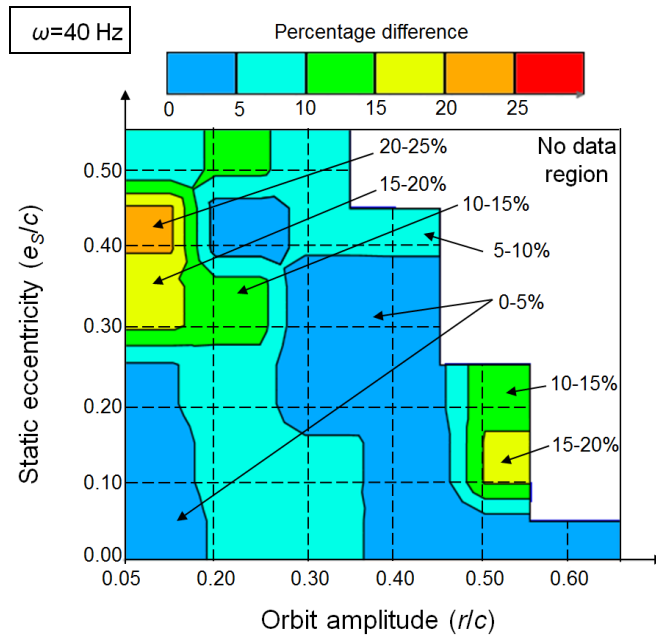
Figure 54. Contour plot mapping the percent difference between the actual (non-linear) SFD dissipated energy and the estimated (linearized) SFD dissipated energy. Tests at various orbit amplitudes and static eccentricities. Whirl frequency ω=40 Hz
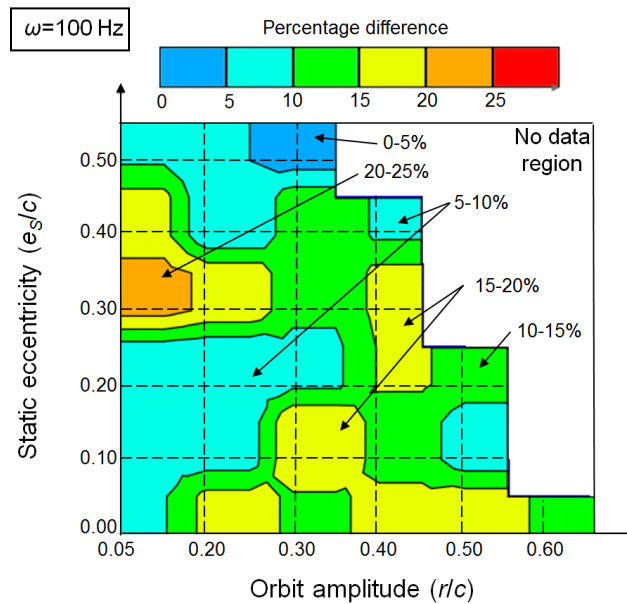
Figure 55. Contour plot mapping the percent difference between the actual (non-linear) SFD dissipated energy and the estimated (linearized) SFD dissipated energy. Tests at various orbit amplitudes and static eccentricities. Whirl frequency ω=100 Hz
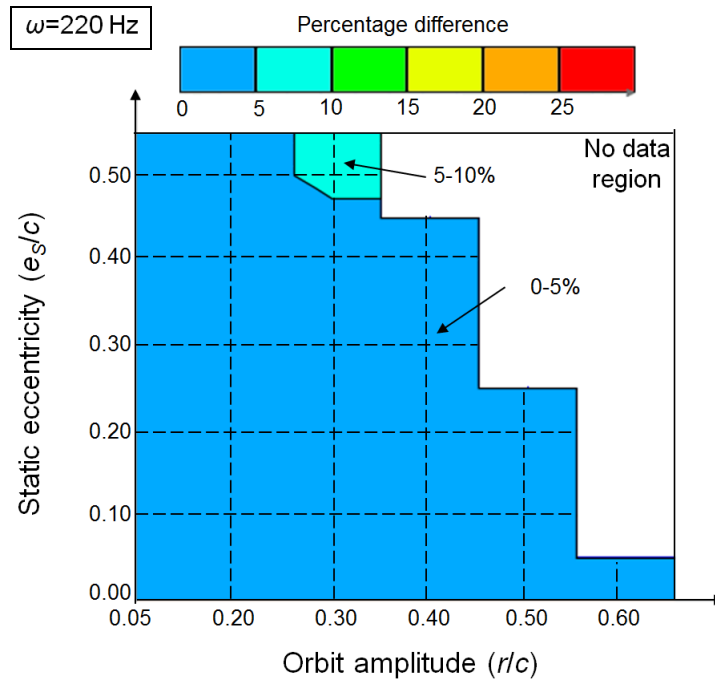
Figure 56. Contour plot mapping the percent difference between the actual (non-linear) SFD dissipated energy and the estimated (linearized) SFD dissipated energy. Tests at various orbit amplitudes and static eccentricities. Whirl frequency ω=220 Hz

For all cases the difference is less than 25%. In fact, at a large frequency of 220 Hz the dissipated energies exhibit <10% difference across all orbit radii and static eccentricities. For the tests with frequencies 40 Hz and 100 Hz, the calculated difference does not show unique trends but is rather sporadic in increases/decreases. Perhaps, the closeness to the system natural frequency (ω_n~130 Hz when lubricated) gives rise to the large differences at 100 Hz.

In any case, the presented analysis of dissipated energy gives credance to the validity of the linearized SFD force coefficients. For most test conditions, the linearized force coefficients can be utilized with confidence.

CHAPTER VII

CONCLUSIONS

This report consolidates work to assess the overall performance of a short land length (L=25.4 mm) SFD supplied with lubricant via radial orifice feed holes. The damper was tested in an open ends condition and its force coefficients identified. The force coefficients are identified from circular and elliptical orbit tests, and tests with 1, 2, and 3 feed holes supplying oil to the film land. In addition, the identified force coefficients are compared to test data from experiments on a similar damper with a central feed groove and two film lands (total land length L=25.4 mm). The major observations derived from the design, comprehensive testing, and analysis are:

From design and testing,

(a) The entire test rig, as currently configured, when excited near 160 Hz shows a large shift in measured impedances, causing poor correlation between a 2-DOF mechanical system model and the measured data in the range of 110-200 Hz. The identification model gives excellent correlation away from this frequency range. Therefore, the range used for parameter identification is 10-250 Hz, excluding data at 110-200 Hz. See Appendix B for further details.

From analysis of film land pressures,

(b) Deep end grooves (c_g~30c, L_g~0.1L) for end seals machined in the journal, actually contribute to the damper forced response when lubricated and operating in an open-end condition. The dynamic pressure generated in the end grooves is almost purely inertial in nature, giving rise to significant added mass coefficients. Note, the total length of the damper including the end grooves and lips is L_{tot}~1.45L.

(c) Significant air ingestion into the oil film is evident for operation with large orbit amplitudes and high frequencies; however, the effects on damper force coefficients is not readily apparent from the current analysis.

(d) Oil vapor cavitation is evident at certain combinations of frequency, orbit amplitude, and static eccentricity combinations in which the pressure drops, from

80

negative squeeze motion, to the lubricant saturation pressure ($P_{sat}{\sim}0$ bar absolute).

(e) Oil cavitation "maps" provide insight into the severity of cavitation at certain test conditions.

From analysis of experimental force coefficients,

(f) SFD direct damping coefficients are insensitive to the amplitude of circular orbital motion. The direct damping coefficients increase with static eccentricity up to e_S=0.3c, but tend to level off at $e_S{\geq}$0.4c. SFD direct inertia coefficients decrease almost linearly as the amplitude of whirl orbit increases. The inertia coefficients remain almost constant with an increase in static eccentricity (e_S).

(g) In general, SFD cross-coupled damping and inertia force coefficients are a small fraction of the direct force coefficients. However, the cross-coupled damping coefficients are significant at large static eccentricities for a small amplitude orbit (r=0.05c, e_S>0.4c) only. SFD stiffness coefficients, direct and cross-coupled, are nearly zero for all tests conducted.

(h) Damping coefficients derived from elliptical orbit tests show nearly identical results as coefficients derived from circular orbit test with amplitude equal to the elliptical major amplitude (r=r_X). Inertia coefficients show differences depending on the orbit amplitude. Importantly enough, little to no difference is observed in force coefficients from elliptical orbit tests with 2:1 and 5:1 amplitude ratios.

(i) SFD damping and mass coefficients are identical for any variation in number of active (open) feed holes (3, 2, 1). In fact, the identified force coefficients still show symmetry ($C_{XX}{\sim}C_{YY}$, $M_{XX}{\sim}M_{YY}$) even though the oil is supplied asymmetrically in the 2 and 1 hole configurations. The lesser number of feed holes is expected to be more prone to oil vapor cavitation due to the low static pressure away from the feed holes.

From comparison between a grooved damper and a non-grooved damper,

(j) The SFD damping coefficients of a damper with two film lands separated by a central feed groove (damper B) are similar ($\pm 10\%$) to the damping coefficients of a damper with the same total film land length fed by 3 orifice feed holes (damper C). The damper with a central feed groove (damper B) has a longer axial physical length and exhibits much larger (~60%) inertia coefficients due to the large feed groove ($c_g \sim 70c$, $L_g \sim 0.5L$).

From comparison between predicted and experimental coefficients,

(k) Predictions from a SFD predictive tool agree very well with the test damping coefficients. However, the tool over predicts the inertia coefficients. This over prediction is due to the SFD predictive tool lacking modeling of the convective fluid inertia.

In conclusion, this thesis analysis provides a comprehensive assessment of the test SFD configuration. The analysis of this specific configuration also brings to light design characteristics, such as a circumferential feed groove, that in fact does not behave as conventionally thought. The same analysis can be conducted with any other SFD configuration to provide an overall dynamic forced performance of the fluid film bearing.

Recommendations for Future Work

Future work should include a similar forced performance assessment of the same damper configuration with end seals installed. The current test rig has the versatility and should be utilized to test novel SFD designs. The current experimental campaign included tests with orbit amplitudes and static eccentricities only up to 50% of the damper clearance. When possible larger amplitudes and eccentricities should be tested[15].

In addition, the in-house numerical program should be updated to include a convective inertia model for accurate predictions of the SFD inertia coefficients. The predictive program can also be improved by modeling the feed holes as source and sink flow models, not just source as they currently are modeled. The computational program can be utilized for preliminary analysis to determine design features for future testing.

---

[15]The size of amplitude is limited by the capacity of the electromagnetic shakers. Large funds are needed to equip the test rig for testing at amplitude $r>0.50c$.

REFERENCES

[1] Cooper, S., 1963, "Preliminary Investigation of Oil Films for Control of Vibration," Proc. of Lubrication and Wear Convention, IMechE, pp. 305-315.

[2] Della Pietra, L., and Adiletta, G., 2002, "The Squeeze Film Damper Over Four Decades of Investigations. Part I: Characteristics and Operating Features," Shock and Vib. Dig., **34**(1) pp. 3-26.

[3] Della Pietra, L., and Adiletta, G., 2002, "The Squeeze Film Damper Over Four Decades of Investigations. Part II: Rotordynamic Analyses with Rigid and Flexible Rotors," Shock and Vib. Dig., **34**(2) pp. 97-126.

[4] San Andrés, L., 2012, *Modern Lubrication Theory*, "Squeeze Film Dampers: Operation, Models and Technical Issues," Notes 13, Texas A&M University Digital Libraries, http://repository.tamu.edu/handle/1969.1/93197 [4/30/2013]

[5] Zeidan, F., San Andrés, L., and Vance, J., 1996, "Design and Application of Squeeze Film Dampers in Rotating Machinery," Proceedings of the 25th Turbomachinery Symposium, Turbomachinery Laboratory, Houston, TX, pp. 169-188.

[6] Reinhardt, F., and Lund, J. W., 1975, "The Influence of Fluid Inertia on the Dynamic Properties of Journal Bearings," ASME J. Lubr. Technol., **97**(1), pp. 154-167.

[7] Tichy, J.A., and Modest, M.F., 1980, "A simple Low Deborah Number Model for Unsteady Hydrodynamic Lubrication Including Fluid Inertia," J. Rheology, **24**(6), pp. 829-845.

[8] Tichy, J.A., 1982, "Effects of Fluid Inertia and Viscoelasticity on Squeeze-Film Bearing Forces," ASLE Trans., **25**(1), pp. 125-132.

[9] Tichy, J.A., 1984, "Measurements of Squeeze-Film Bearing Forces and Pressures, Including the Effect of Fluid Inertia," ASLE Trans., **28**(1), pp. 520-526.

[10] San Andrés, L., 1985, "Effect of Fluid Inertia Effect on Squeeze Film Damper Force Response," Ph.D. Dissertation, Texas A&M University, College Station, TX, December.

[11] San Andrés, L., 1992, "Analysis of Short Squeeze Film Dampers with a Central Groove," ASME J. Tribol., **114**(4), pp. 659-665.

[12] Arauz, G., and San Andrés, L., 1994, "Effect of a Circumferential Feeding Groove on the Dynamic Force Response of a Short Squeeze Film Damper," ASME J. Tribol., **116**(2), pp. 369-377.

[13] Arauz, G., and San Andrés L., 1996, "Experimental Study on the Effect of a Circumferential Feeding Groove on the Dynamic Force Response of a Sealed Squeeze Film Damper," ASME J. Tribol., **118**(4), pp 900-905

[14] Zhang J. X., and Roberts J. B.,1996, "Force Coefficients for a Centrally Grooved Short Squeeze Film Damper," ASME J. Tribol., **118**(3), pp. 608-616

[15] Ellis, J., Roberts, J. B., and Hosseini, S. A., 1990, "The Complete Determination of Squeeze-Film Linear Dynamic Coefficients from Experimental Data," ASME J. Tribol., **112**(4), pp. 712-724.

[16] Qingchang, T., Ying, C., and Lyjiang, W., 1997, "Effect of a circumferential feeding groove on fluid force in short squeeze film dampers," Tribol. Int., **30**(6), pp. 409-416.

[17] Lund, J., W., and Myllerup, C., M., Hartmann, H., 2003, "Inertia Effects in Squeeze-Film Damper Bearings Generated by Circumferential Oil Supply Groove," J. Vib. Acoust., **125**(4), pp. 495-499

[18] Kim, K. J., and Lee, C. W, 2005, "Dynamic Characteristics of Sealed Squeeze Film Damper with a Central Feeding Groove," ASME J. Tribol., **127**(1), pp. 103-111.

[19] Delgado, A., 2008, "A Linear Fluid Inertia Model for Improved Prediction of Force Coefficients in Grooved Squeeze Film Dampers and Grooved Oil Seal Rings," Ph.D. Dissertation, Texas A&M University, College Station, TX, December.

[20] Sun, D., and Brewe, D., 1991, "A High Speed Photography Study of Cavitation in a Dynamically Loaded Journal Bearing," ASME J. Tribol., **113**(2), pp. 287-294.

[21] Sun, D., and Brewe, D., 1993, "Simultaneous Pressure Measurement and High-Speed Photography Study of Cavitation in a Dynamically Loaded Journal Bearing," ASME J. Tribol., **115**(1), pp. 88-95.

[22] Xing, C., and Braun, M., 2010, "Experimental Investigation of the Development of Cavitation in a Squeeze Film Damper," Proceedings of the STLD/ASME 2010 International Joint Tribology Conference, San Francisco, CA, October 17-20, IJTC2010-41144, pp. 1-3.

[23] Diaz, S.E., and San Andrés, L., 2001, "Air Entrainment Versus Lubricant Vaporization in Squeeze Film Dampers: An Experimental Assessment of Their Fundamental Differences," ASME J. Eng. Gas Turbines and Power, **123**(4), pp. 871-877.

[24] Jakobsson, B. and Floberg, L., 1957, "The Finite Journal Bearing Considering Vaporization," Trans. Chalmers University of Technology (Guthenberg, Sweden), **190**.

[25] Olsson, K. O., 1965, "Cavitation in Dynamically Loaded Bearings," Trans. Chalmers University of Technology (Guthenberg, Sweden), **308**.

[26] Elrod, Jr. H.G., 1981, "A Cavitation Algorithm," ASME J. Lub. Tech., **103**(3), pp. 350-354.

[27] Vijayarahavan, D. and Keith, T. G., 1990, "An Efficient, Robust and Time Accurate Numerical Procedure Applied to a Cavitation Algorithm," ASME J. Tribol., **112**(1), pp. 44-51.

[28] Diaz, S., and San Andrés, L., 1999, "A Method for Identification of Bearing Force Coefficients and its Application to a Squeeze Film Damper with Bubbly Lubricant," STLE Tribol. Trans., **42**(4), pp. 739-746.

[29] Mendez, T., Torres, J., Ciaccia, M., and Diaz, S., 2010, "On the Numerical Prediction of Finite Length Squeeze Film Dampers Performance with Free Air Entrainment," ASME J. Eng. Gas Turbines and Power, **132**, pp. 1-7.

[30] Younan, A., Cao, J., Dimond, T., and Allaire, P., 2011, "Nonlinear Analysis of Squeeze Film Damper with Entrained Air in Rotordynamic Systems," STLE Tribol. Trans., **54**(2), pp. 132-144.

[31] Levesley, M.C., and Holmes, R. 1996, "The Effect of Oil Supply and Sealing Arrangements on the Performance of Squeeze-Film Dampers: An Experimental Study," Proceedings of the IMechE, Part J: J. Eng. Tribol., pp. 210-221**.**

[32] Chen, P.Y., and Hahn, E.J. 1994, "Pressure Distribution in Squeeze Film Dampers with Oil Hole Feed," Proceedings of the IMechE, Part J: J. Eng. Tribol., pp. 105-112**.**

[33] Walton II, J. F., Walovit, J. A., Zorzi, E. S., and Schrand, J. 1987, "Experimental Observation of Cavitating Squeeze-Film Dampers," ASME J. Tribol., **109**(2) pp. 290-295.

[34] Defaye, C., Arghir, M., and Bonneau, O., 2006, "Experimental Study of the Radial and Tangential Forces in a Whirling Squeeze Film Damper," STLE Tribol. Trans., **49**(2) pp. 271-278.

[35] Tiwari, R., Lees, A. W., and Friswell, M.I., 2004, "Identification of Dynamic Bearing Parameters: A Review," Shock Vib. Dig., **36**(2) pp. 99-124.

[36] Fritzen, C.-P., 1986, "Identification of Mass, Damping, and Stiffness Matrices of Mechanical Systems," J. Vib. Acoust., **108**, pp. 9-16.

[37] San Andrés, L., and Delgado, A., 2007, "Identification of Force Coefficients in a Squeeze Film Damper with a Mechanical End Seal—Part I: Unidirectional Load Tests," ASME J. Eng. Gas Turbines and Power, **129**(3) pp. 858.

[38] San Andrés, L., and Delgado, A., 2007, "Identification of Force Coefficients in a Squeeze Film Damper with a Mechanical End Seal—Centered Circular Orbit Tests," ASME J. Tribol., **129**(3) pp. 660.

[39] Delgado, A., and San Andrés, L., 2009, "Nonlinear Identification of Mechanical Parameters in a Squeeze Film Damper with Integral Mechanical Seal," ASME J. Eng. Gas Turbines and Power, **131**(4) pp. 042504.

[40] Gehannin, J., Arghir, M., and Bonneau, O., 2010, "Complete Squeeze-Film Damper Analysis Based on the "Bulk Flow" Equations," STLE Tribol. Trans., **53**(1), pp. 84-96.

[41] San Andrés, L. and Delgado, A., 2007, "Parameter Identification of an End Sealed SFD Part II: Improved Predictions of Added Mass Coefficients for Grooved SFDs and Oil Seals," Research Progress Report to the Turbomachinery Research Consortium TRC-SFD-1-07, Texas A&M University, College Station, TX, May.

[42] Seshaghiri, S., 2011, "Identification of Force Coefficients in Two Squeeze Film Dampers with a Central Groove," M.S. Thesis, Texas A&M University, College Station, TX, May.

[43] Mahecha, P., 2011, "Experimental Dynamic Forced Performance of a Centrally Grooved, End Sealed Squeeze Film Damper," M.S. Thesis, Texas A&M University, College Station, TX, August.

[44] San Andrés, L., 2010, "XL_SFD," SFD Predictive Code Developed for Pratt & Whitney Engines, Texas A&M University, College Station, TX.

[45] San Andrés, L., 2012, *Modern Lubrication Theory*, "Thermal Analysis of Finite Length Journal Bearings Including Fluid Inertia Effects," Notes 7, Texas A&M University Digital Libraries, College Station, TX, http://repository.tamu.edu/handle/1969.1/93197 [4/30/2013]

[46] San Andrés, L., 2012, *Modern Lubrication Theory*, "Fluid Inertia and Turbulence in Fluid Film Bearings," Notes 9, Texas A&M University Digital Libraries, College Station, TX, http://repository.tamu.edu/handle/1969.1/93197 [4/30/2013]

[47] San Andrés, L., 2012, *Modern Lubrication Theory*, "A Note on Power Dissipation From Whirl Motions in a Fluid Film Bearing," Appendix to Notes 5, Texas A&M University Digital Libraries, College Station, TX, http://repository.tamu.edu/handle/1969.1/93197 [4/30/2013]

[48] "NI cDAQ – 917x User Manual," User manual for NI Compact DAQ 9171/9174/9178 USB Chassis, National Instruments, July 2011, Appendix A. Specifications.

[49] Beckwith, T., Marangoni, R., and Lienhard, J. 1993, "Mechanical Measurements", Prentice Hall, 5th edition, pp. 82

[50] "Uncertainty Analysis", Physical Chemistry Laboratory, University of Delaware, Accessed Jan. 2013, pp. 9, http://www.udel.edu/pchem/C446/error.pdf

APPENDIX A

TEST RIG AND LUBRICANT PROPERTIES

Static Load Test

Static load tests aid to determine the test rig structure static stiffness (K_S) by measuring the amount of force (F) required to displace the BC a certain amount δ ($K_S = F/\delta$). Figure A.1 shows a schematic view of the test rig with the static hydraulic loader pulling the BC. This loader is 45° away from the (X, Y) axes. The procedure records the applied load and the ensuing BC displacements (with respect to the stationary journal) along the (X, Y) axes and along the 45° direction. Figure A.2 shows the load versus displacement data and notes the stiffnesses derived from the respective slopes for the linear fits. It is important to note that the displacements shown are recorded with the eddy current sensors facing the center of the film land.
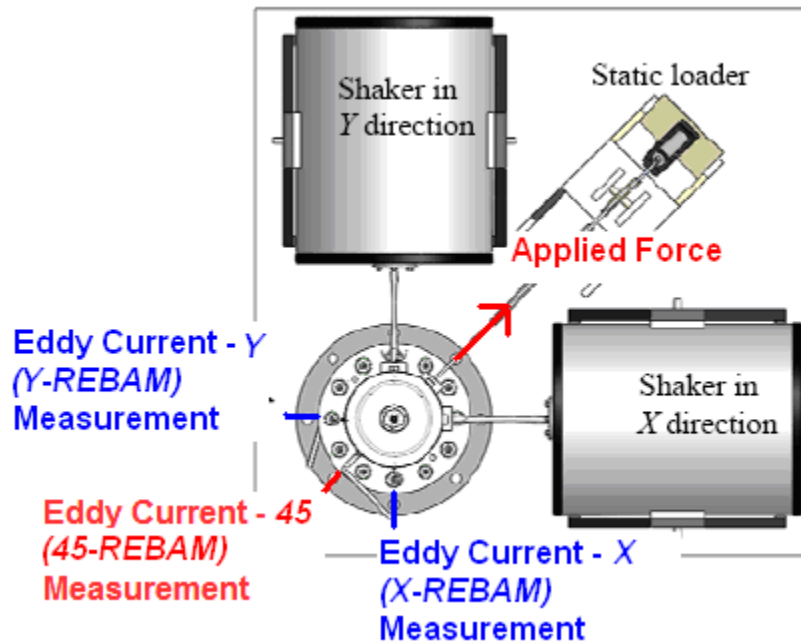

Figure A 1. SFD test rig top view schematic showing the set up for a static load test
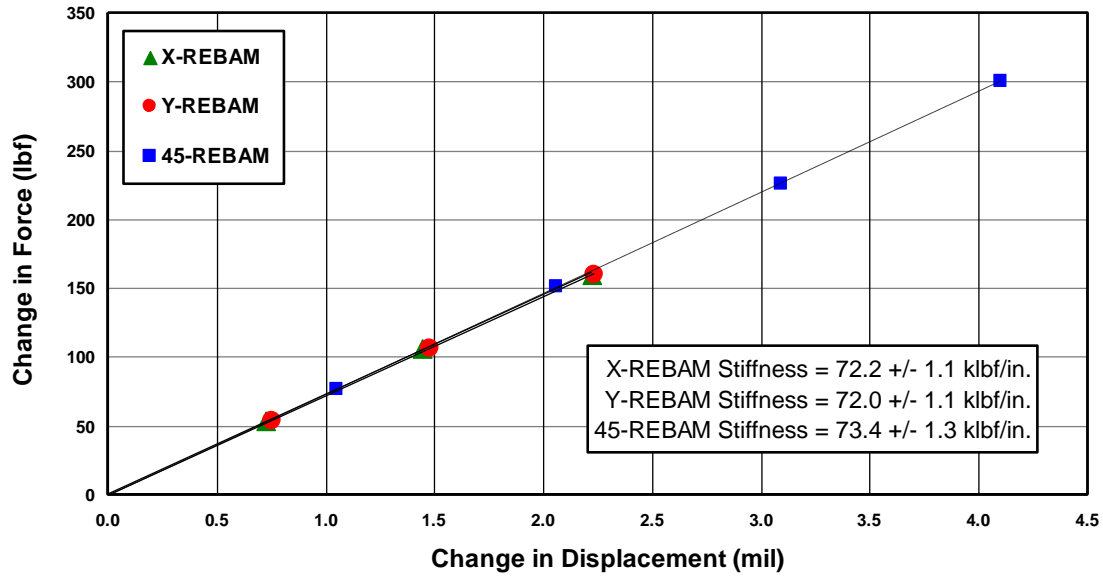
Figure A 2. Test results for static load vs. measured BC displacement to identify the structural static stiffness of the test rig

The structural static stiffness in the direction of the applied load is K_S= 12.85 MN/m (73.4 klbf/in.), while the structural static stiffness along the X and Y directions is K_{SX}=12.64 MN/m (72.2 klbf/in.) and K_{SY}=12.60 (72.0 klbf/in.)

The mass of the BC (14.65 kg) plus the effective mass contributed by the support rods (0.5 kg) is hereby referred to as the BC mass M_{BC} =15.15 kg (33.4 lb)[16]. Therefore the predicted system natural frequency, $\omega_n = (K_s/M_{BC})^{1/2}$, is ~ 146 Hz in all directions (*X, Y,* 45º).

Lubricant Viscosity Measurements

The oil viscosity is of particular interest, as it largely determines the damping capability and the flow characteristics. As per the manufacturer, the ISO VG 2 oil has a rated density (ρ) of 0.80 g/cm3 and kinematic viscosity (*v*) of 2.2 cSt at 40ºC. This lubricant has similar viscosity as the ones in aircraft engines at actual (elevated) operating temperatures.

---

[16] The BC mass was measured on a scale prior to installation. Based on a structural beam calculation, M_{rods} is equivalent to the 25% the total mass of all four rods.

Measurement of a known volume of oil and its weight gives a density of $\rho = 0.78$ g/cm³. A Brookfield DV-E rotary viscometer equipped with a hot water bath delivers the oil absolute viscosity (μ) at increasing temperatures, 23 °C to 50 °C, as shown in Figure A.3. For predictive purposes, the ASTM standard viscosity-temperature relation is

$$\mu = \mu_R e^{-\alpha_v (T - T_R)} \tag{A.1}$$

where $\mu_R = 2.47$ cPoise is the measured viscosity at room temperature ($T_R = 23$ºC). The oil viscosity coefficient (α_v,) is

$$\alpha_v = \frac{-\ln(\mu_2 / \mu_R)}{(T_2 - T_R)} = 0.021 \frac{1}{^\circ C} \tag{A.2}$$

where T_2 and μ_2 are the highest temperature recorded and oil viscosity, respectively. The ISO VG2 kinematic viscosity (v) at 40ºC is 2.20 cSt. Since dynamic viscosity ($\mu = v / \rho$), then Eq. (A.1) predicts 2.21 cSt at 40ºC, thus demonstrating the lubricant satisfies the rated specifications. Note that the kinematic viscosity actually measured at 38.8ºC is 2.18 cSt. The measured viscosity at testing supply temperature ($T_S = 22.2$ºC) is $\mu = 2.5 \pm 0.025$ cP.
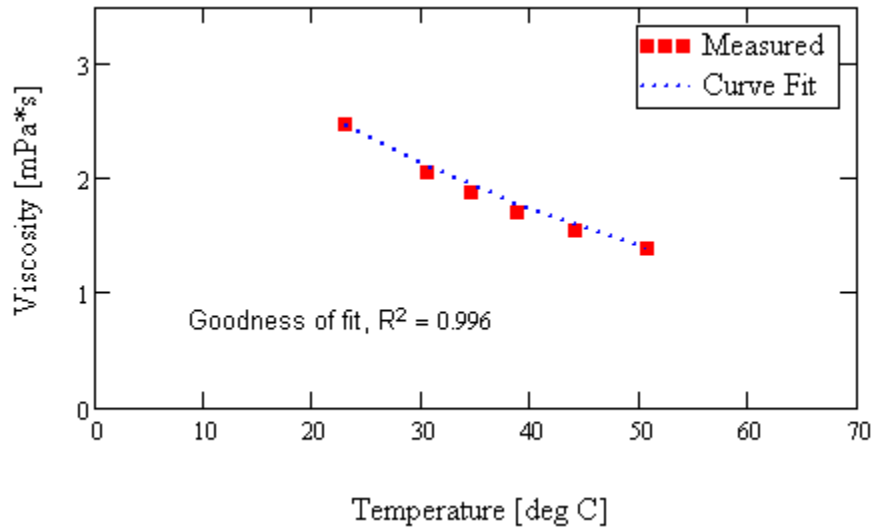

Figure A 3. Measured dynamic viscosity vs. temperature for ISO VG 2 oil

Flow Rate Measurements

The SFD test rig supplies lubricant to the damper film land via 3 radial feed holes (spaced 120° apart) with orifice inserts (hole diameter is 2.57 mm). Lubricant flows through the top and bottom sections of the film land and exits to ambient. The inlet flow rate (Q_{in}) is user controlled and measured by a turbine flow meter. The bottom outlet flow rate (Q_b) is measured by timing how long it takes to fill a known volume with lubricant. For a damper with a uniform clearance (BC and journal perfectly centered and aligned), the ratio of bottom land flow to inlet flow must equal 50%, Q_b/Q_{in}=0.50. A dial pressure gauge measures the inlet pressure (P_{in}) of the lubricant before entering the SFD test rig. Figure 11 (see chapter V) shows the disposition of static (strain gauge) pressure sensors in the SFD test rig. E_2, located at Θ=45°, measures the film land pressure directly in front of a lubricant feed hole. E_1, located at Θ=135°, measures the film land pressure 30° away from a lubricant feed hole.

Table A.1 lists the recorded static pressures, supply and bottom flow rates, and the ratio Q_b/Q_{in}. The table also list the total film lands flow conductance, $C_{total} \sim Q_{in}/(E_2-P_a)$, and the bottom half film land flow conductance, $C_b \sim Q_b/(E_2-P_a)$. Note ambient pressure P_a= 0 psig. The flow conductances (C) are derived from curve fits of the flow rates vs. feed hole pressure (E_2).

Table A 1. Measured lubricant flow rates for open end damper without a central groove and film clearance c=129.5 μm. 25.4 mm film land length

E_2 bar	Q_{in} LPM	Q_b LPM	Ratio Q_b/Q_{in}
0.29	2.50	1.33	0.54
0.50	3.67	2.04	0.55
0.72	5.04	2.92	0.58
0.81	5.64	3.10	0.55
Flow Conductance			
LPM/bar	5.88	3.29	0.56

EXCLUSION OF DATA AT FREQUENCIES 110-250 HZ

The test data for the system impedances (and flexibilities) in the frequency domain shows large shifts/jumps for excitation frequencies ranging from 120-200 Hz. Figure B.1 shows this shift in the real and imaginary parts of the direct impedance function,

$$H_{XX_{(\omega)}} = \frac{F_{X_{(\omega)}} - M_{BC} a_{X_{(\omega)}}}{x_{(\omega)}}$$

, as well as in the amplitude of the flexibility function

. Here, $F_{X(\omega)}$ is the DFT of the applied shaker load in the X

$$G_{XX_{(\omega)}} = \frac{x_{(\omega)}}{F_{X_{(\omega)}} - M_{BC} a_{X}}$$

direction, a_X is the DFT of the measured BC acceleration, and x is the DFT of the measured BC displacement. Recall that $M_{BC} = 15.15$ kg.
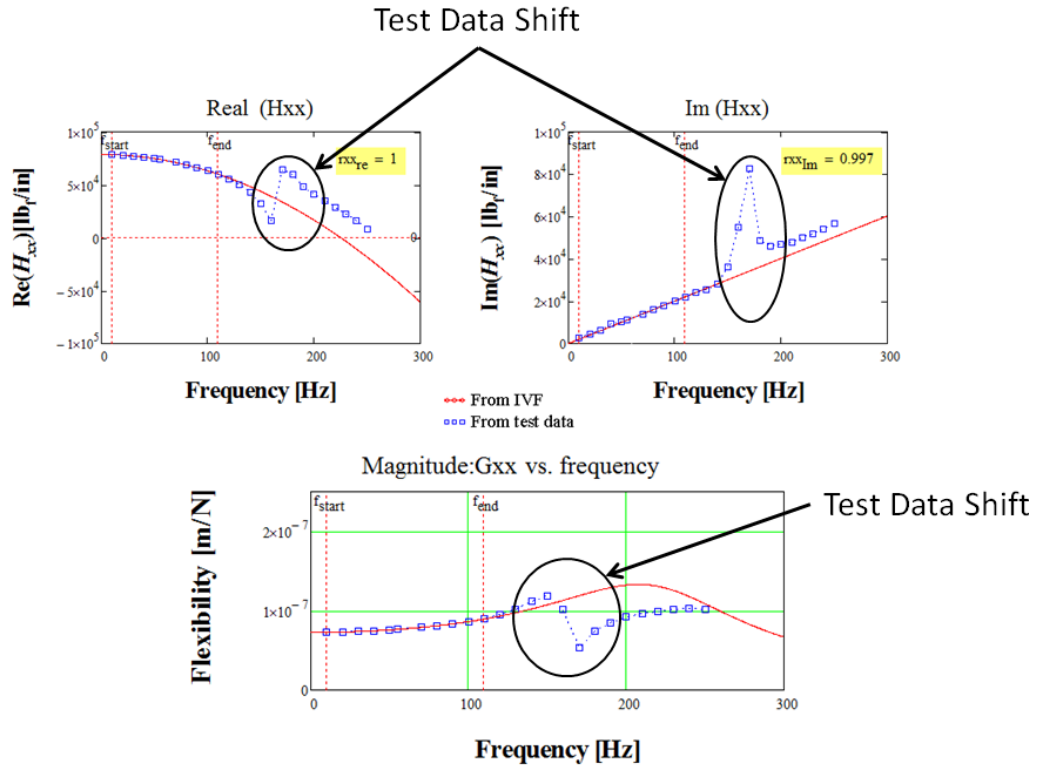

Figure B 1. Real and imaginary parts of HXX and amplitude of flexibility GXX versus frequency. Data shows drastic shift in experimental data. CCO test with orbit radius _r_=0.2_c_

Because of the noted shift in experimental data, former students limited the parameter identification range to below 100 Hz. The shift is caused by a resonance at ~157 Hz to 162 Hz of the pedestal supporting the entire test rig. This resonance is due to the way the pedestal is mounted to the table (i.e., with a rubber isolation mat). The same type of mat is used underneath the e-shakers. Figure B.2 shows the location of the rubber mat that causes a non-rigid mounting of the test rig and shakers.

Figure B 2. Side view of SFD test rig and *X*-Shaker showing the location of the vibration isolation mat

If journal motion is present and slightly out of phase with the BC motion, the relative acceleration ($\ddot{x}$ or $\ddot{y}$) and absolute BC acceleration (a_X or a_Y) will be different. The current identification model already corrects for this difference. Thus, the shift in experimental data is NOT due to journal motion, but rather to an artificial "stiffening" effect.

Figure B.3 shows the amplitude of the applied load from the shakers along the *X,Y* directions to produce an orbit with radius $r=0.20c$. Just around 130-140 Hz, the applied load reaches a minimum, which denotes the excitation of the system natural frequency (bearing cartridge and support rods). As the excitation frequency increases, the amplitude of the applied load should increase steadily, $F \sim M\omega^2$. However, the data evidences a sudden "hump" at around 160 Hz, the pedestal natural frequency. This

94

artificial "stiffening" of the test system involves a more complicated physical modeling. Hence, a modified identification model must be developed that accounts for the difference in load at this frequency.
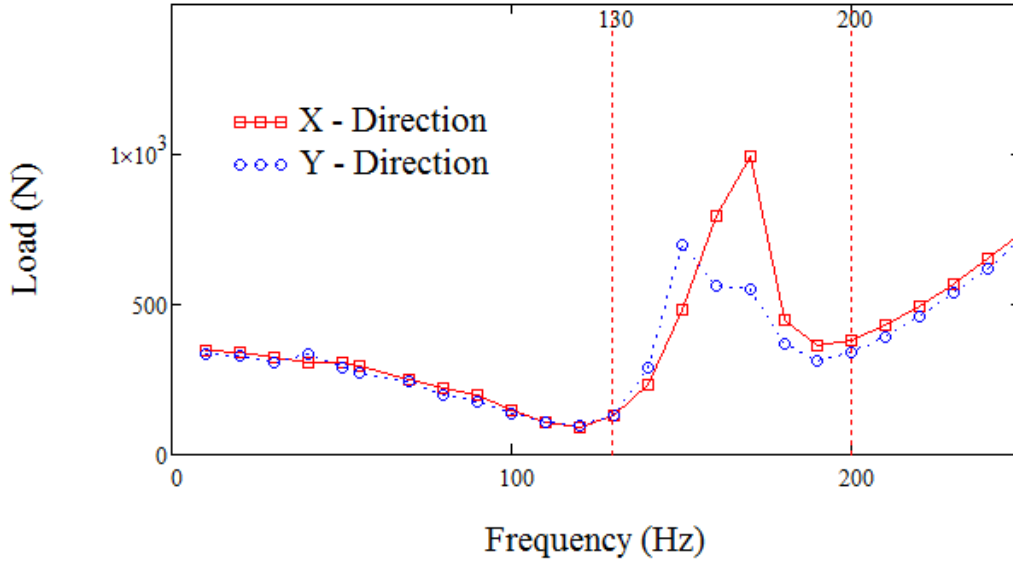

Figure B 3. Amplitude of shaker loads, *X* and *Y* axes, versus excitation frequency

Presently, maintaining a parameter identification range of 10-250 Hz but excluding data in the range from 110-200 Hz, i.e. away from the pedestal ω_n, gives an excellent correlation between the assumed physical model and the experimental data. Figure B.4 shows the fit of the physical model to the experimental data for the real and imaginary parts of the impedance ($H_{XX_{(\omega)}} = \dfrac{F_{X_{(\omega)}} - M_{BC} a_{X_{(\omega)}}}{x_{(\omega)}}$) as well as the flexibility function

($G_{XX_{(\omega)}} = \dfrac{x_{(\omega)}}{F_{X_{(\omega)}} - M_{BC} a_{X_{(\omega)}}}$) with data excluded in the range from 130-200 Hz. Only data

for tests along the *X* direction is shown. Note that the data for the *Y* direction impedance and flexibility functions exhibit the same trend.
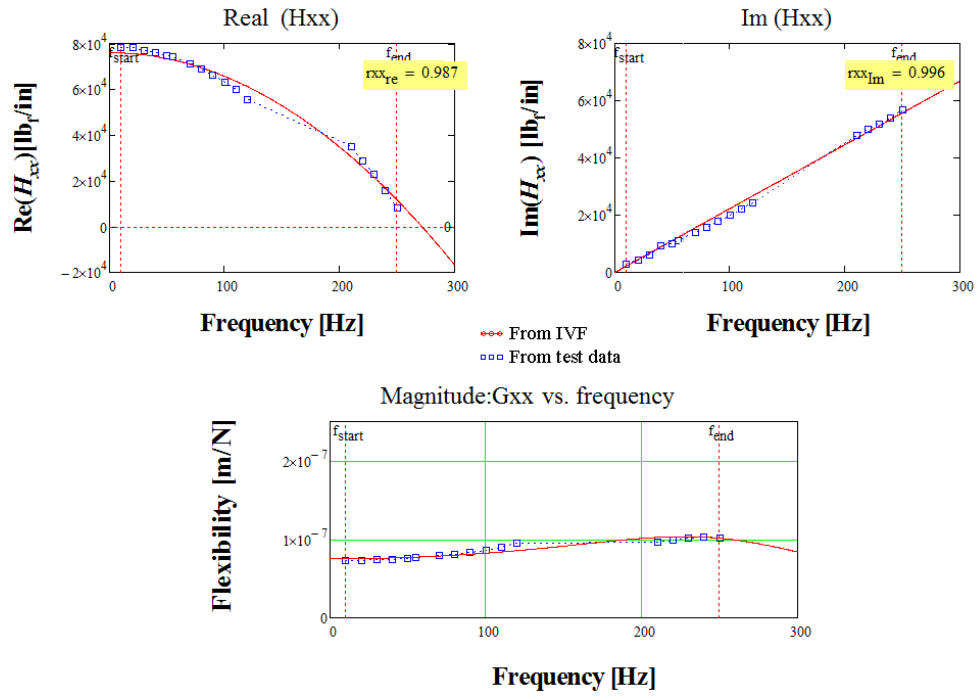
Figure B 4. Real and imaginary parts of H_{XX} and amplitude of flexibility G_{XX} versus frequency. Data at 110-200 Hz excluded from identification. CCO test with orbit radius *r*=0.2*c*

APPENDIX C

UNCERTAINTY ANALYSIS

This section outlines the calculation of uncertainty in identified SFD force coefficients. The total uncertainty consists of a bias (instrument) uncertainty and a precision (measurement variability) uncertainty. Both types of uncertainty are outlined, along with the combination of bias and precision into total uncertainty for each force coefficient $(K, C, M)_{\text{SFD}}$. For brevity the calculated values are based on largest possible cases; the actual uncertainty values may be less than these calculated values. Bias, precision, and total uncertainties are denoted as B, P, and U, respectively.

Bias (Instrument) Uncertainty

The data acquisition (DAQ) board has a rated uncertainty of $B_{DAQ} = 0.1\%$ in the measurement of voltage [48]. The DAQ board sampling rate is 16,384 samples/second, storing 4096 samples and giving an uncertainty in the output frequency of $B_{\omega} = 2\,\text{Hz}$ for the entire frequency range [48]. This is equivalent to $B_{\omega} = 20\%$ at the lowest test frequency of 10 Hz, $B_{\omega} = 0.8\%$ at the largest test frequency of 250 Hz, and an average of $B_{\omega} = 3.1\%$ across the entire range. Note, the following analysis considers the average $B_{\omega} = 3.1\%$, because the force coefficients are best fit over the entire range. From calibrations, the uncertainty of X and $Y -$ REBAM® (displacement) sensors are $B_X = 4.3\%$ and $B_Y = 4.4\%$, respectively. The load cell uncertainty is $B_{LOAD} = 1.0\%$. With these individual uncertainties, the propagation of uncertainty into the measurements of displacement and force, respectively, are

$$B_{DISP} = \sqrt{(B_{REBAM})^2 + (B_{DAQ})^2} = 4.4\% \tag{C.1}$$

$$B_{FORCE} = \sqrt{(B_{LOAD})^2 + (B_{DAQ})^2} = 1.0\% \tag{C.2}$$

Knowledge of frequency domain relations $K \sim F/D$, $C \sim (F/D)\omega$, and $M \sim (F/D)\omega^2$ aids to determine the total bias uncertainty in force coefficients as

97

$$B_K = \sqrt{(B_{DISP})^2 + (B_{FORCE})^2} = 4.5\% \qquad \text{(C.3)}$$

$$B_C = \sqrt{(B_{DISP})^2 + (B_{FORCE})^2 + (B_{\omega})^2} = 5.5\% \qquad \text{(C.4)}$$

$$B_M = \sqrt{(B_{DISP})^2 + (B_{FORCE})^2 + (2 \cdot B_{\omega})^2} = 7.7\% \qquad \text{(C.5)}$$

Recall, determination of the SFD force coefficient requires subtraction of dry system coefficients from lubricated system coefficients, i.e.

$$(\mathbf{K}, \mathbf{C}, \mathbf{M})_{SFD} = (\mathbf{K}, \mathbf{C}, \mathbf{M}) - (\mathbf{K}, \mathbf{C}, \mathbf{M})_{S} \qquad \text{(C.6)}$$

Therefore, propagation of the bias uncertainty from two measurements into the SFD coefficient's bias is

$$B_{K_{SFD}} = \sqrt{(B_{K_S})^2 + (B_K)^2} = 6.4\% \qquad \text{(C.7)}$$

$$B_{C_{SFD}} = \sqrt{(B_{C_S})^2 + (B_C)^2} = 7.7\% \qquad \text{(C.8)}$$

$$B_{M_{SFD}} = \sqrt{(B_{M_S})^2 + (B_M)^2} = 10.8\% \qquad \text{(C.9)}$$

Precision Uncertainty

Precision uncertainty deals with the repeatability of measurements. However, only one set of tests were conducted at each test condition (r, e_S). This set of tests consisted of individual tests at several pre-selected frequencies (ω). Plotting the real and imaginary part of the measured impedance versus frequency and using an IVFM curve fit (variation of least squares) gives plots as those shown in Figure G.1. The stiffness coefficient (K) is estimated as the Y-intercept and the mass coefficient (M) is estimated as the slope of the real part of the measured mechanical impedance. The slope of the imaginary part of the measured mechanical impedance is the estimated damping coefficient (C).
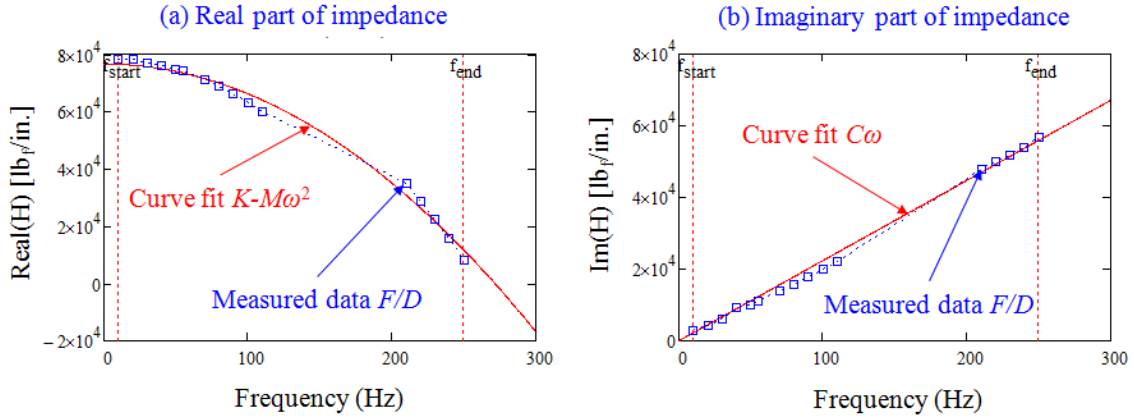
Figure C 1. Plots real (a) and imaginary (b) parts of mechanical impedance versus frequency (ω). Curve fit and measured data shown

For the estimation of precision uncertainty in a single measurement, Ref. [49] gives

$$P = 1.96 \cdot (S) \tag{C.10}$$

where S is the estimated standard deviation based upon engineering knowledge. Ref. [50] gives relations for estimated standard deviation of the intercept and slope of a least squares fit line as

$$S_{Intercept} = \sqrt{\frac{1}{N(N-2)}\frac{1-r^2}{r^2}} \tag{C.11}$$

$$S_{Slope} = \sqrt{\frac{1}{(N-2)}\frac{1-r^2}{r^2}} \tag{C.12}$$

where N is the number of points used for the curve fit and r^2 is the curve fit correlation. Using the relations given in C.11 and C.12 with $N=16$ and $r^2=0.95$, the largest standard deviation in the estimated stiffness, damping, and mass coefficients, respectively, are

$$S_K = \sqrt{\frac{1}{N(N-2)}\frac{1-r^2}{r^2}} = 0.015 \text{ MN/m} \tag{C.13}$$

$$S_C = \sqrt{\frac{1}{(N-2)}\frac{1-r^2}{r^2}} = 0.061 \text{ kN}\cdot\text{s/m}^2 \tag{C.14}$$

99

$$S_M = \sqrt{\frac{1}{(N-2)} \frac{1-r^2}{r^2}} = 0.061 \text{ kg} \tag{C.15}$$

The corresponding precision uncertainty in the force coefficients are

$$P_K = 1.96 \cdot (S_K) = 0.03 \text{ MN/m} \tag{C.16}$$

$$P_C = 1.96 \cdot (S_C) = 0.12 \text{ kN} \cdot \text{s/m}^2 \tag{C.17}$$

$$P_M = 1.96 \cdot (S_M) = 0.12 \text{ kg} \tag{C.18}$$

and propagation into the uncertainty of SFD coefficients gives

$$P_{K_{SFD}} = \sqrt{P_{K_S}^2 + P_K^2} = 0.3\% \tag{C.19}$$

$$P_{C_{SFD}} = \sqrt{P_{C_S}^2 + P_C^2} = 3.0\% \tag{C.20}$$

$$P_{M_{SFD}} = \sqrt{P_{M_S}^2 + P_M^2} = 2.1\% \tag{C.21}$$

Total Uncertainty

The total uncertainty in each SFD force coefficients are

$$U_{K_{SFD}} = \sqrt{B_{K_{SFD}}^2 + P_{K_{SFD}}^2} = 6.4\% \tag{C.22}$$

$$U_{C_{SFD}} = \sqrt{B_{C_{SFD}}^2 + P_{C_{SFD}}^2} = 8.4\% \tag{C.23}$$

$$U_{M_{SFD}} = \sqrt{B_{M_{SFD}}^2 + P_{M_{SFD}}^2} = 11.0\% \tag{C.24}$$

Note these uncertainty values are for SFD coefficients estimated from a minimum $N=16$ test frequencies and an IVFM curve fit correlation with a minimum of $r^2=95\%$. This uncertainty analysis also takes the average DAQ frequency uncertainty as $B_\omega = 3.1\%$ over the tested frequency range.